A COUPLED THERMAL/ELECTRIC CIRCUIT MODEL FOR DESIGN OF MVDC CABLES

by

Xiang Zhang

A Dissertation

Submitted to the Faculty of Purdue University

In Partial Fulfillment of the Requirements for the degree of

Doctor of Philosophy

School of Electrical & Computer Engineering

West Lafayette, Indiana

December 2019

THE PURDUE UNIVERSITY GRADUATE SCHOOL
STATEMENT OF COMMITTEE APPROVAL

Dr. Steven Pekarek, Chair
School of Electrical and Computer Engineering

Dr. Scott Sudhoff
School of Electrical and Computer Engineering

Dr. Oleg Wasynczuk
School of Electrical and Computer Engineering

Dr. Jiao Dan
School of Electrical and Computer Engineering

Approved by:

Dr. Dimitrios Peroulis
Head of the Graduate Program

I dedicate this work to my parents, Xianjun Zhang and Xiaoyan Zhang for inspiring me into the world of electric engineering. Thanks my grandparents, Yingtian Zhang and Jiajin Ye for their unconditional and endless support and love. Thanks my cat Zuanfeng the Maine who supports me through the most difficult time.

ACKNOWLEDGMENTS

Firstly, I would like to thank my major advisor Dr. Steven Pekarek for accepting me to join the group and for his guidance and support in my research and daily life during my PhD. I could not accomplish such an achievement without his patience and help. I would also like to thank my committee member Dr. Oleg Wasynczuk, Dr. Scott Sudhoff, and Dr. Dan Jiao. It is Dr. Wasynczuk who taught me the very first lesson in power engineering and led me into the world of electric machines. Dr. Scott Sudhoff taught me invaluable knowledge on the equivalent circuit method. Without this, this work could not be done. Dr. Dan Jiao provided me with important knowledge on electromagnetic analysis and theories. I would also like to thank my friends and fellow students for their amazing advices and support through my research and life.

I would like to thank Office of Naval Research (ONR) for funding this work under grant #N00014-16-1-2956.

Finally, I would like to thank my families for supporting me study abroad and my US family Mr. Ed Niles and Mrs. Paulette Niles for providing me with a lovely sweet home and unique experiences of a traditional US family far away home.

TABLE OF CONTENTS

LIST OF TABLES

LIST OF FIGURES

ABSTRACT

Author: Zhang, Xiang. PhD
Institution: Purdue University
Degree Received: December 2019
Title: A Coupled Thermal/Electric Equivalent Circuit Model for Design of MVDC Cable
Major Professor: Steven D. Pekarek

Cables play an important role in the design of a power system. DC cable design presents unique challenges due to the fact that space charge can accumulate within the dielectric over time. Space charge accumulation is a function of temperature, electric field, and dielectric properties. Of particular concern is that the space charge leads to electric fields that are sufficient to break down the cable, particularly during transient conditions such as voltage reversal.

In this research, a focus is on the development of a coupled thermal- and electrical-equivalent-circuit model that is general and provides the ability to predict the electric fields and space charge accumulation within single and multi-conductor DC cables. In contrast to traditional analytical models, the approach is more general, allowing for exploration of a wide spectrum of geometries. In contrast to traditional numerical methods, including finite element or finite difference, apriori knowledge of the electric field behavior is used to discretize the dielectric into a small number of electric flux tubes. The electric field dynamics within each tube are then modeled using a first order nonlinear differential equation. The relatively coarse discretization enables the solution to be computed rapidly. This is useful in population-based design where a large number of candidate evaluations is necessary to explore a design space. The modeling approach has been validated using several examples presented in the literature. In addition, its usefulness has been highlighted in the optimization of a 20 kV cable wherein objectives include minimization of mass and loss.

1. INTRODUCTION

1.1 Motivation

Over the past century, the majority of utility power systems have utilized AC transmission and distribution. Niche applications, such as grid-to-grid interconnections, utilize DC subsystems. Advantages of DC include eliminating the need for synchronization and reactive power matching [1][2][3][4]. Advances in power electronics have led to further interest in DC power systems. For example, they are utilized to provide power in large data centers, at the interconnection of wind farms, and ship power systems [5][6][7].

Cables play an important role in the design of a DC power system [8][9][10]. Their mass/volume/cost is often an appreciable percent of the total system mass/volume/cost. Cable junctions/connections are often a location of wear/fatigue/failure. Finally, they often must endure surge current resulting from faults or large power variations. Although their geometry is relatively straightforward, their design is complicated by the fact that under DC excitation, the electric field within a cable is dependent upon the conductivity of the dielectric. Since the conductivity is a function of temperature and electric field as shown in Fig.1.1 [8], its value is dependent on the location within the dielectric. This positional dependence leads to charge migration which results in so-called space charge accumulation. The space charge accumulation results in electric fields that are challenging to predict. In addition, during transients, such as voltage reversal, the pre-transient space charge can lead to electric fields that far exceed the nominal cable ratings. This has been shown as a key source of cable failures [1][2][11].

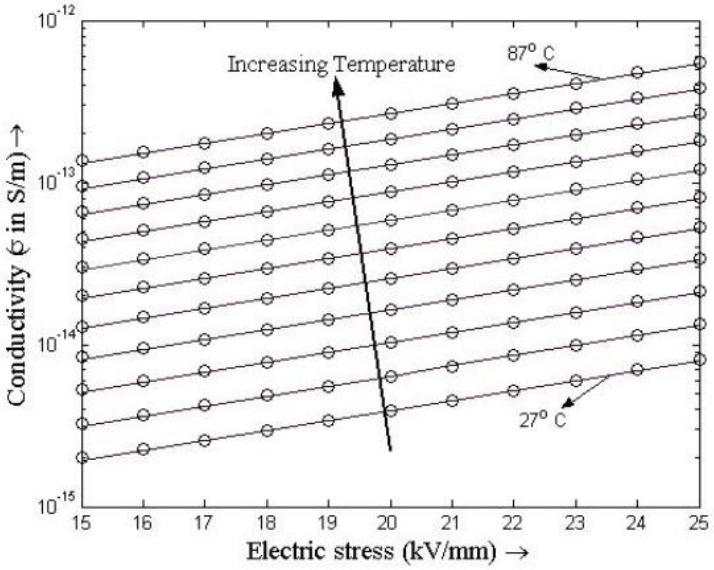

Fig.1.1 Conductivity performance of XLPE under various temperature and electric field[8]

In an effort to optimize DC systems, several alternative cable architectures have been proposed. Three are shown in Fig.1.2. In Fig.1.2(a), a DC bus is created using two coaxial style cables. Such a design provides potential installation advantage, since an installer only has to work with a single conductor when making terminations. In ship applications, it has a potential disadvantage in that the net magnetic field surrounding the DC bus can be significant which results in potential magnetization of surrounding steel. The middle topology shown in Fig.1.2(b) greatly reduces the magnetic field surrounding the DC bus. The third geometry shown in Fig.1.2(c) has an advantage that the temperature within the DC bus can be regulated using forced air or thermal fluid within the center of the interior conductor [12].

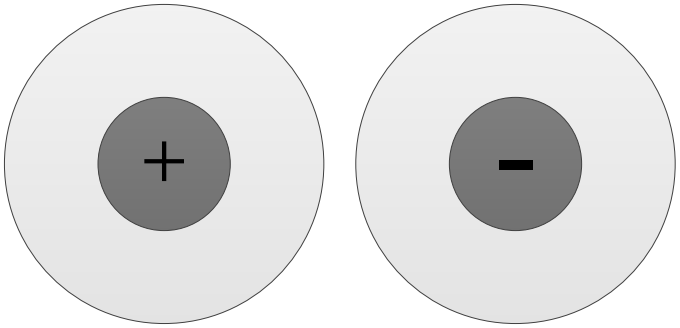

Fig.1.2(a) Single conductor layout

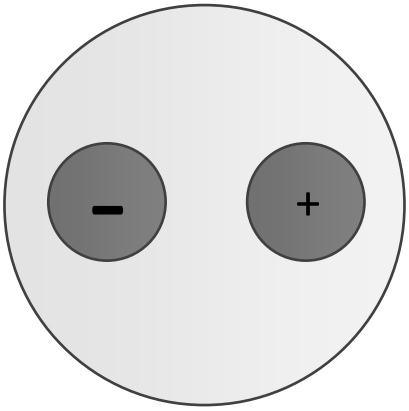

Fig.1.2(b) Multi-conductor layout

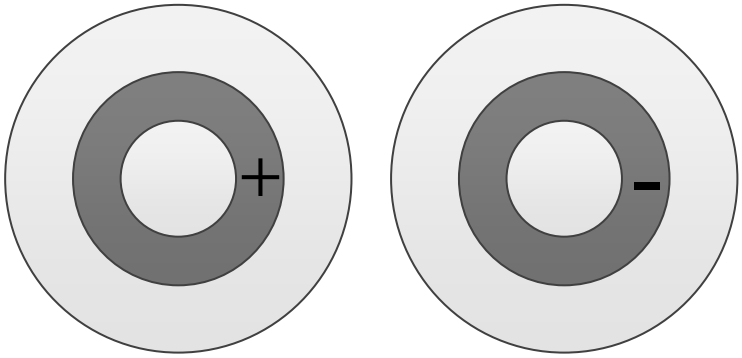

Fig.1.2(c) Bus pipe (Self-contained Fluid-filled(SCFF)) cable layout

Fig.1.2 Cable architectures

Several researchers have considered the designs shown in Fig.1.2(a). To establish the designs, they have traditionally relied upon analytical approaches, experiments, or numerical-

based analysis to predict the electromagnetic fields within the dielectric [2][8][9][10][11] [13][14][15][16].

In this thesis, the modelling and design of DC cable will be set forth using a coupled electric/thermal equivalent circuit method. The proposed method is capable of predicting coupled electric/thermal dynamic performance of the dielectric. It is relatively computationally efficient so that it enables a multi-objective optimization of cables so that one can rigorously compare alternative architectures.

1.2 Literature Reviews of Existing Approaches

In [11], the nonlinear electrical and thermal dynamics that relate the electric field, current density, and charge density are discretized in time and space using a finite element method (FEM). This method is capable of describing the dielectric performance both under the transient and steady state operations. It is a general approach that can be applied to the multiple geometric alternatives as shown in Fig.1.2. In practice, the electric and thermal distribution may be simulated using commercial FEM software tools such as Ansys Maxwell or COMSOL[17][18][19]. However, there is a significant computational burden imposed by the nonlinear conductivity and relatively small discretization level.

Alternatively, to ease the computational burden, the steady state electric field distribution has been derived using analytical techniques for a coaxial structure in Fig.1.2(a) [11]. Since the steady-state value of the electric field relies only on the conductivity, the dielectric layer is modeled as a nonlinear resistor. The local potential is found using Kirchhoff's Voltage Law. The gradient of the resulting potential is used to establish a nonlinear equation that relates the electric field to the conductivity, the applied voltage and temperature. The resulting electric field is solved using

any one of a number of nonlinear solvers. Although valuable for single conductor cables, such an approach is not easily extended to multi-conductor cable architectures.

An alternative analytical approach can be derived by utilizing a truncated Taylor series to establish a closed form expression that relates the electric field to the temperature and the current in the dielectric [8]. The challenge of this approach is obtaining the analytical expression for the dielectric current. In addition, it is difficult to generalize the method to alternative geometries.

In practice, the direct measurement of the electric field within the dielectric is difficult to perform. As an alternative, the charge within the dielectric has been estimated using nondestructive methods such as the Pressure-Wave-Propagation Method (PWP), Pulsed Electro-Acoustic Method (PEA) and Laser Induced Pressure Pulse Method (LIPP) [9][10][11][16] [20][21][22][23][24][25]. In the PEA method, a pulsed electric field is applied to the dielectric sample. The pulsed external field induces a perturbation force which moves the space charge within the dielectric. This movement launches an acoustic wave which propagates through the dielectric and is received by a transducer. The space charge can be then estimated using the propagated acoustic signals. The space charge can be used to predict the electric field through numerical integration. It is an accurate method to determine the electric field distribution. However, it requires special equipment, an existing cable, and a means to place the cable under the thermal gradient of interest. Thus, it is not directly applicable to cable design.

1.3 Objectives

The objective of this research is to develop a modeling approach that can be used to predict the dynamic electric field response within the dielectric of alternative DC cables, while keeping the computational requirement low. In addition, a goal is to structure the respective cable models

for use in multi-objective optimization so that alternative designs can be compared with sufficient rigor.

The cable model proposed utilizes coupled thermal/electric equivalent circuits to predict the electric field, temperature, and space charge based upon the voltage applied to the conductor, current in the conductor, material properties, and the cable geometry. To derive the model, the dielectric is discretized into resistive tubes that relate the potential to the dielectric current. The tubes are arranged to predict the steady state electric field using Kirchhoff's Voltage Law. In addition, they are used to calculate the space charge. Subsequently, the tube surface charge is used to relate the potential to the electric flux within each tube. The ratio of electric flux over the tube potential is used to calculate the equivalent capacitance that is used for transient analysis.

The electric equivalent circuit model is introduced in Chapter 2 and validated with the existing methods presented in the literature. The results from the model are compared and discussed with other models. Special transient cases including voltage reversal are examined and evaluated. Error analysis and solver algorithms that minimize computational burden are also considered.

As shown in Fig.1.1, temperature plays an important role in shaping the electric field. Hence, to incorporate the electric and thermal behavior together using the equivalent tube, a thermal equivalent circuit model is proposed in Chapter 3. The thermal equivalent circuit model enables the prediction of both transient and steady-state thermal performance, which can be incorporated with the electric circuit to better describe the transient electric field performance including overload conditions.

In Chapter 4, the approach is extended and developed for a multi-conductor cable with the topology shown in Fig.1.2(b). The formulation of the model is achieved using judicious application of the Method of Images (MOI). In addition, the validation of the model is performed through comparison of results obtained using finite element analysis acquired from COMSOL.

In Chapter 5, a population based multi-objective design optimization of MVDC cable is performed using a Genetic Algorithm [26]. A 3D Pareto-Optimal Front is set forth by comparing conduction loss, cable size and cable mass. Subsequently, a case study with the objective of a 20 kV 30 MW application is performed. Several design candidates are studied and discussed based on the performance of the temperature behavior, electric field distribution, and space charge profile. In addition, the use of the cable model is demonstrated in a system level simulation. Therein, a 20 kV 30 MW MVDC ship auxiliary power system is simulated using parameters obtained by applying per-unit transformation to the system depicted in [7]. The cable system is implemented between the active bridge rectifier and the load system. A line-to-line fault is initiated that results in large current surge. From this simulation a voltage reversal is observed and studied during the fault and subsequent recovery.

In Chapter 6, defect charge is a result of impurities in the dielectric material [44]. The defects may have the potential to create field distortions that lead to premature failure of the dielectric, electric discharge and dielectric breakdown for example. Herein, an attempt is made to explore methods to approximate the result of the defect charge within the equivalent electric circuit model. The validation of the defect charge is performed through comparison of results obtained from COMSOL. Finally, in Chapter 7 future research paths are proposed.

2. ELECTRIC EQUIVALENT CIRCUIT

2.1 Introduction

The behavior of electric fields within DC cables has been of increasing interest, due to their use in coupling renewable energy sources into the utility power system [1][2][3][4]. Solving for the dynamic response of the electric field in cables requires knowledge of the conductivity of the dielectric material, which has been shown to be a function of temperature and electric field [2] [8][9][11][14][24][27][28]. This leads to challenges in deriving analytical and numerical solutions. Herein, an electrical equivalent circuit approach is proposed to address these issues and at the same time enable efficient computation to support DC cable design.

2.2 Quasi-Steady State Model of Electric Field in DC Cables

2.2.1 General equations for model constructions

To support the analytical derivations presented in this chapter, it is convenient to consider the cross section of the cable provided in Fig.1.2(a). In practice, to create a DC bus, a voltage is placed between the center conductor and a center conductor of a second cable. As a result, a voltage is present from each center conductor to the outside shield that is taken to be ground. Herein it is assumed that current flows within the center conductors. Loss created by the current is dissipated to air through the dielectric. In order to derive a simplified cable model, it is convenient to first consider the electromagnetic behavior within the dielectric under steady-state and quasi-steady state operation.

From the law of charge conservation and the divergence theorem [1][2][8][9][13][16][28], it can be shown that the divergence of free current density, $\vec{J}_f$, is equal to the rate of change of the volumetric free charge density, ρ_v.

$$\nabla \cdot \vec{J}_f = -\frac{\partial \rho_v}{\partial t} \tag{2.1}$$

From Maxwell's equations, it is known that the curl of the electric field is the negative rate of change of magnetic flux density:

$$\nabla \times \vec{E} = -\frac{d\vec{B}}{dt} \tag{2.2}$$

One can express $\vec{B}$ as the curl of a vector magnetic potential.

$$\vec{B} = \nabla \times \vec{A} \tag{2.3}$$

Equation (2.2) and (2.3) can be combined as,

$$\nabla \times (\vec{E} + \frac{d\vec{A}}{dt}) = 0 \tag{2.4}$$

From vector calculus, it is known that the curl of the gradient of a potential is zero:

$$\nabla \times \nabla V = 0 \tag{2.5}$$

Therefore, one can use (2.4) and (2.5), to express

$$\vec{E} = -\nabla V - \frac{d\vec{A}}{dt} \tag{2.6}$$

Assuming the influence of the time-rate of change of flux density is negligible[9][11], the electric field is expressed

$$\vec{E} = -\nabla V \tag{2.7}$$

From Maxwell's equations,

$$\nabla \cdot \vec{D} = \rho_v \tag{2.8}$$

, where electric flux density $\vec{D}$, can expressed as,

$$\vec{D} = \varepsilon \vec{E} \tag{2.9}$$

with ε representing the permittivity. Substituting equation (2.9) into (2.8) and taking the derivative of both sides with respect to time, it can be shown that,

$$\nabla \cdot \frac{d(\varepsilon \vec{E})}{dt} = \frac{d\rho_v}{dt} \tag{2.10}$$

Within the dielectric, any free current density is proportional to the electric field

$$\vec{J}_f = \sigma \vec{E} \tag{2.11}$$

The rate of change of volumetric space charge present in the dielectric in equation (2.10) can be expressed in terms of conductivity and electric potential by combining equation (2.1), (2.7) and (2.11). This yields,

$$\nabla \cdot [\sigma(-\nabla V)] = -\frac{d\rho_v}{dt} \tag{2.12}$$

Equating the terms in (2.10) and (2.12), one can show

$$\nabla \cdot (\sigma \nabla V) - \nabla \cdot \frac{d(\varepsilon \vec{E})}{dt} = 0 \tag{2.13}$$

Substituting (2.7) into (2.13), one can establish a quasi-steady state model of the electric potential within the dielectric of a DC cable:

$$\nabla \cdot (\sigma \nabla V) + \nabla \cdot \frac{d(\varepsilon \nabla V)}{dt} = 0 \tag{2.14}$$

From (2.14), one can observe that under steady-state DC conditions,

$$\nabla \cdot (\sigma \nabla V) = 0 \tag{2.15}$$

which, perhaps contrary to intuition, shows that the electric field within the dielectric is solely dependent on its conductivity (and boundary conditions).

2.2.2 Empirical expressions for conductivity

It has been shown in the literature that the conductivity of a dielectric is a function of temperature and electric field. Several researchers have proposed models to describe the relationship [1][2][3][8][11][14][27]. These include:

$$\sigma(r,T,\vec{E}) = \sigma_0 e^{-\frac{b}{T(r)}} e^{a|\vec{E}(r)|} \tag{2.16}$$

$$\sigma(r,T,\vec{E}) = \sigma_0^{'} e^{-\frac{b'}{T(r)}} \frac{\sinh(a'|\vec{E}(r)|)}{|\vec{E}(r)|} \tag{2.17}$$

$$\sigma(r,T,\vec{E}) = \sigma_0 e^{\alpha T(r)} e^{\beta|\vec{E}(r)|} \tag{2.18}$$

where σ_0, $\sigma_0^{'}$ are referred to as the nominal conductivity, b, b' and α are temperature coefficients, and a, a' and β are electric field coefficients, respectively. Herein, to support correlation with existing literature, the models of (2.16) and (2.18) have been selected for the model development.

2.3 Electric Equivalent Circuit

2.3.1 Flux tube in magnetic equivalent circuit

In the field of quasi-steady state magnetic analysis, besides Finite Element Analysis (FEA), researchers often use Magnetic Equivalent Circuit (MEC) analysis. In MECs, [29] a volume that contains magnetic material, conductors, and air, is partitioned into flux tubes. An example flux tube is shown in Fig.2.1. The flux tube approach assumes that the volume is surrounded by two equipotential surfaces. It is further assumed that the total number of flux lines are the same at the two equipotential surfaces. In other words, no flux lines penetrate the side surface. Although typically applied to magnetic systems, similar analogies can be used to form electric equivalent circuits. In an electric equivalent circuit, one possible model uses voltages at the tube ends, and models the current through the respective tube using Ohm's law. The resistance is calculated using

$$R = \int_0^l \frac{dx}{c(x)A(x)} \tag{2.19}$$

, where $c(x)$, $A(x)$ and l are a function of material property, cross-sectional area and the total flux tube length respectively. By applying different material properties such as conductivity σ, permittivity ε and permeability μ, the R shown in (2.19) can be interpreted as the resistance, the inverse of capacitance and reluctance respectively.

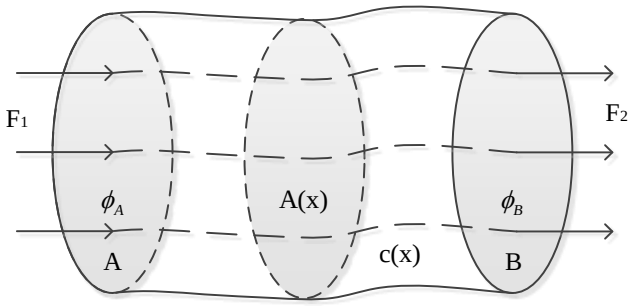

Fig.2.1 Flux tube model

An equivalent circuit model based on cable characteristics is proposed in this thesis. The analogy of basic circuit elements can be a comprehensive way to simulate the performance of medium material and corresponding field distribution.

2.3.2 Electric flux tube model for steady state models

If one substitutes any of the expressions for conductivity in (2.16) - (2.18) into (2.15), it is difficult, if not intractable, to establish an analytical expression for the electric potential or electric field within the dielectric. To solve for the electric potential, researchers have adopted FEA and finite difference methods [17][18][19].

Herein, an alternative path is proposed. As a starting point, the dielectric is partitioned into electric tubes in which it is assumed that conductivity remains a constant within the tube. This simplifies (2.15) to yield an expression within the tube

$$\sigma\nabla\cdot(\nabla V)=0 \tag{2.20}$$

For some geometries, one can solve (2.20) analytically. However, this is not a generally applicable approach. Instead, it convenient to consider that (2.20) indicates that the divergence of the electric field within a tube is zero. Since (2.20) is established through the relationship between current density and electric field, one can formulate an equivalent circuit that is representative of (2.20). The electric circuit is that of a resistive tube shown in Fig.2.2. As shown, the two ends of the tube are equipotential surfaces (labeled A and B).

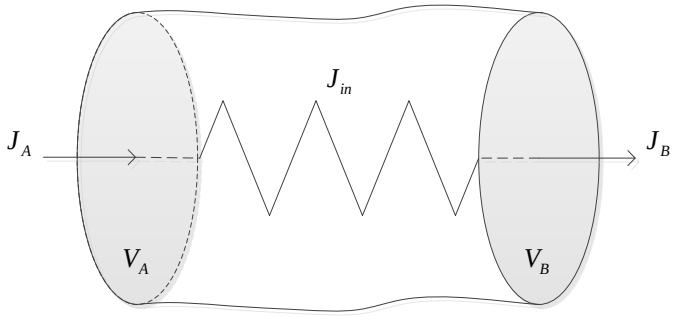

Fig.2.2 An equivalent resistor tube

The electric current density is assumed to enter and leave the resistive tube (orthogonally), only at the two equipotential surfaces. This suggests that no internal charge exists within the enclosed volume. This would suggest that the approximation is being made that the space charge is located at the boundary of the flux tube. Electric resistance can be used to model the relationship between the surface potentials, where

$$R = \frac{V}{I} \tag{2.21}$$

and I is taken as the integral of the current density over the tube cross sectional area. A general expression for the tube resistance is

$$dR = \frac{dr}{\sigma S(r)} \tag{2.22}$$

Applying the flux tube concept to the DC cable shown in Fig.2.3, one can break the dielectric material into N concentric tubes shown in Fig.2.4 and Fig.2.5. For each tube, one can express the differential resistance in a form

$$dR = \frac{dr}{\sigma(2\pi r l_d)} \tag{2.23}$$

$$R = \int_{r_{sp,n}}^{r_{ep,n}} \frac{dr}{\sigma(2\pi r l_d)} \tag{2.24}$$

where $r_{sp,n}$ and $r_{ep,n}$ stand for the start point and end point of the current ring tube respectively and can be expressed as,

$$r_{sp,n} = r_{in} + \frac{D_i}{N}(n-1) \tag{2.25}$$

$$r_{ep,n} = r_{in} + \frac{D_i}{N} n \tag{2.26}$$

where n denotes the segment, l_d is the unit depth along the cable direction, D_i is the thickness of the dielectric layer, and r_{in} is the radius of the inner conductor.

Solving (2.23) yields

$$R_n(T,E) = \frac{\ln(\frac{r_{ep,n}}{r_{sp,n}})}{\sigma(T,E)2\pi l_d} \tag{2.27}$$

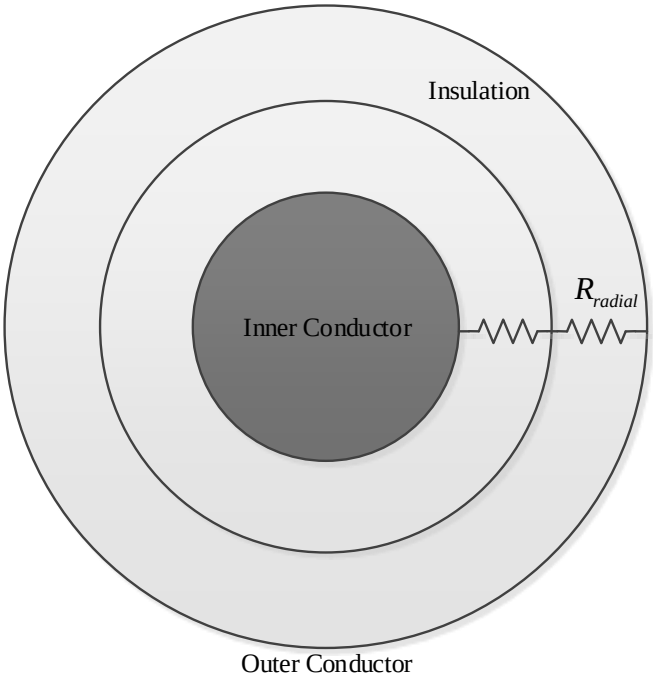

Fig.2.3 Single serial resistor circuit model

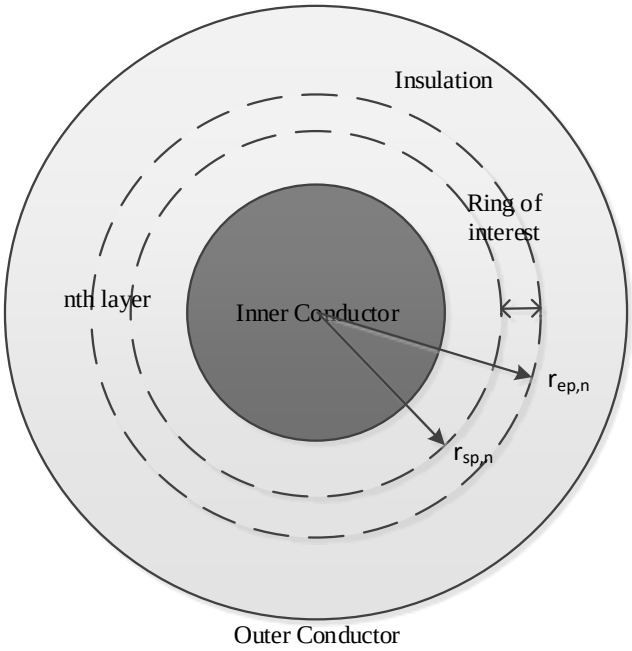

Fig.2.4 Ring shape of interest

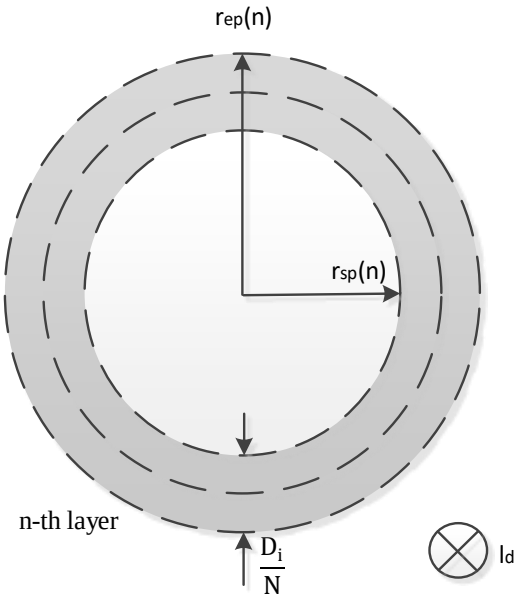

Fig.2.5 The dimension of the ring shape

To solve the steady-state behavior within the dielectric, one can utilize Kirchhoff's laws applied to the circuit shown in Fig.2.6. To do so, the total resistor in series as displayed in Fig.2.6 can be obtained by taking a summation of segment resistors expressed in (2.28).

$$R_{total}(T,E)=\sum_{n=1}^{N}R_n(T,E)=\sum_{n=1}^{N}\frac{\ln(\frac{r_{ep,n}}{r_{sp,n}})}{\sigma(T,E)\cdot(2\pi l_d)} \tag{2.28}$$

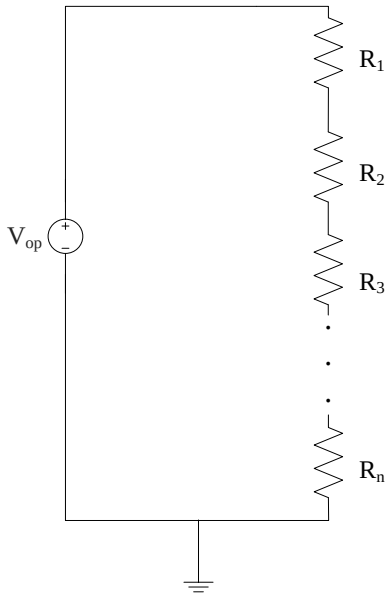

Fig.2.6 Steady-state equivalent circuit model of co-axial cable

In (2.28), the conductivity is a function of the electric field in the tube as well as the temperature. The temperature is obtained by the thermal equivalent circuit outlined in Chapter 4. The electric field used in the conductivity is assumed to be that at the midpoint of each electric tube. The electric field at the center of each tube must be solved using numerical techniques. To do so, the current through the dielectric is first obtained using

$$I(T,E)=\frac{V_{op}}{R_{total}(T,E)}=\frac{V_{op}}{\sum_{n=1}^{N}\frac{\ln(\frac{r_{ep,n}}{r_{sp,n}})}{\sigma(T,E)2\pi l_d}} \tag{2.29}$$

Subsequently, the current density at the mid-point of each tube is expressed through geometry as,

$$J_n(T,E)=\frac{I(T,E)}{2\pi\frac{r_{sp,n}+r_{ep,n}}{2}l_d} \tag{2.30}$$

Finally, the electric field is related to current density. Doing so for all tubes, one can establish an equation of the form

$$\begin{pmatrix} E_1 \\ \vdots \\ E_N \end{pmatrix} - \begin{pmatrix} \frac{1}{\sigma(E_1,T)} & \cdots & \frac{1}{\sigma(E_N,T)} \end{pmatrix} \begin{pmatrix} J_1(E,T) \\ \vdots \\ J_N(E,T) \end{pmatrix} = \begin{pmatrix} 0 \\ \vdots \\ 0 \end{pmatrix} \tag{2.31}$$

During steady state operation, temperature is a constant during solution calculation. Hence, the solution of (2.31) can be found by solving

$$f(\mathbf{E}) = \mathbf{E} - (\boldsymbol{\sigma}^{-1}(\mathbf{E}))^T \mathbf{J}(\mathbf{E}) = 0 \tag{2.32}$$

Herein, a Newton Raphson method is applied to find solutions to (2.32).

2.3.3 Steady-state electrical equivalent circuit validation

An algorithm to implement the solution of the steady state equivalent circuit model is shown in Fig.2.7. As shown in the figure, the algorithm is initialized with geometric, thermal and electrical parameters, where the thermal solution is acquired from the thermal equivalent circuit. An initial electric field distribution is constructed by assuming a uniform conductivity across the dielectric. In subsequent iterations, the respective electrical components and conductivity are updated using (2.28) - (2.32). A convergence test is based on the absolute change in electric field between two steps.

$$\left| E^{k+1} - E^k \right| < e_{\max,step} \tag{2.33}$$

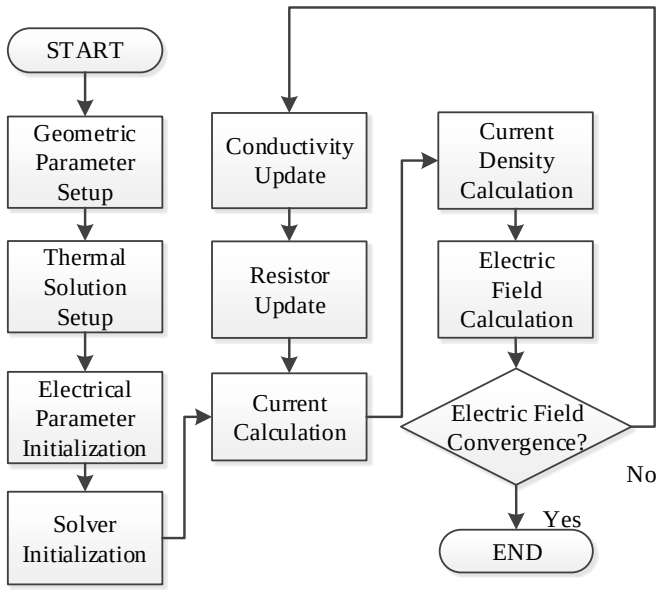

Fig.2.7 Block diagram for steady-state electric circuit model

To validate the approach, the behavior predicted by the electric equivalent circuit has been compared with those presented in [8]. In [8], an Aluminum-XLPE single cable system has been examined for model construction. The cable geometry and material properties are shown in Table 2.1. The cable has rated voltage of 600kV and a current range of 1600-1800A. Under these conditions, the field predicted assuming an equivalent circuit is shown in Fig.2.8. Also shown are Reddy's [8] results as well as the electric field predicted if conductivity is assumed to be uniform. From the results, one can observe the field inversion that occurs when a conductivity is a function of space and field. This inversion is more pronounced as the thermal gradient across the dielectric increases, which occurs with higher power loss. One also notes that the predicted results closely match those presented in [8]. A second example is also listed herein to validate the electric field distribution of a 450 kV, 1600 mm^2 cable system shown in Fig.2.9 [11], whose parameters are presented in Table 2.2.

Table 2.1 Reddy's Cable Parameters [8]

Geometric Parameters	
r_1	22.5mm
r_2	44.2mm
Conductor Parameters	
Material	Aluminum
conductivity	36.9×10^{6} S/m
Dielectric Parameters	
Material	XLPE
k_i	0.34 W/mK
A/σ_0	2.2896×10^{-6} $(\Omega m)^{-1}$
a	0.142×10^{-6} $(V/m)^{-1}$
b	7600 K
ε_r	4.2
C_p[50]	2300 $J(kgK)^{-1}$
ρ[51][52]	950 kg/m^{-3}

Table 2.2 Jeorense's Cable Parameters [11]

Geometric Parameters	
r_1	23.2mm
r_2	42.4mm
Conductor Parameters	
Material	Aluminum
conductivity	36.9×10^{6} S/m
Dielectric Parameters	
Material	Oil-Paper
k_i	N.A.
A	2.2896×10^{-6} $(\Omega m)^{-1}$
β	0.1 $(V/m)^{-1}$
α	0.03×10^{-6} $^oC^{-1}$
ε_r	3.5
C_p[50]	2300 $J(kgK)^{-1}$
ρ[51][52]	950 kg/m^{-3}

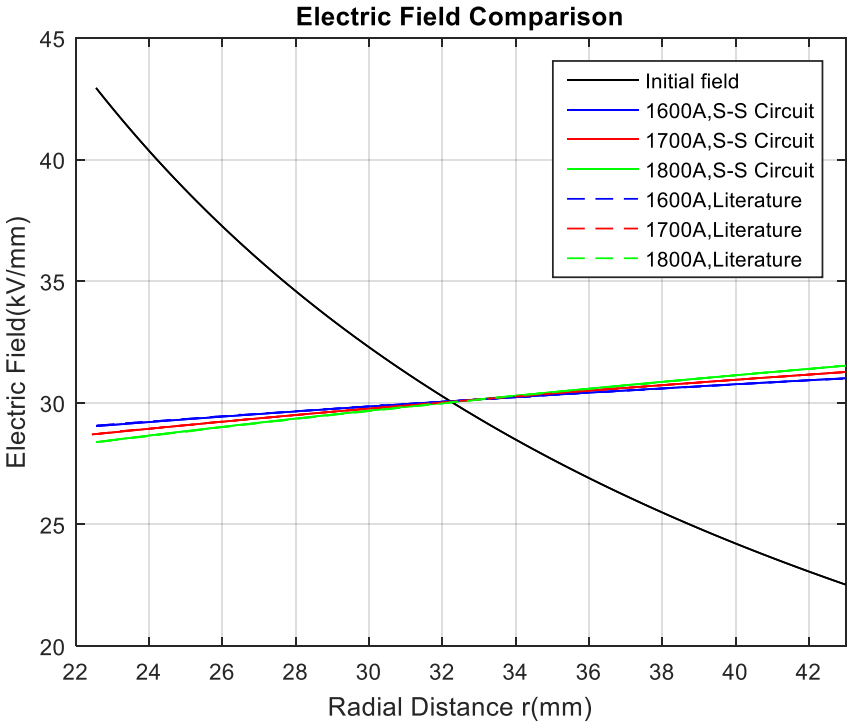

Fig.2.8 Steady-state electric field comparison with [8]

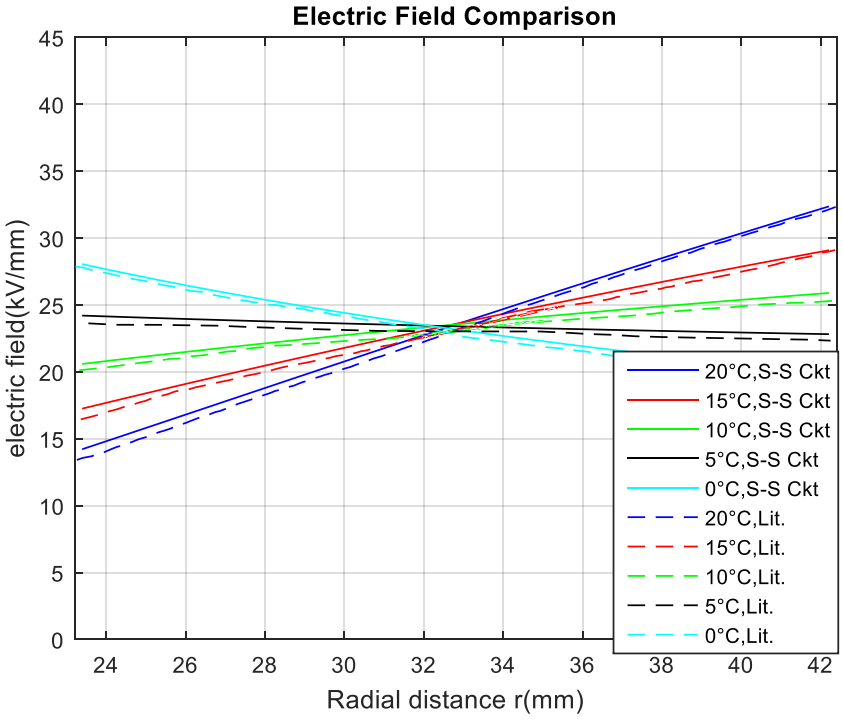

Fig.2.9 Steady-state electric field comparison with [11]

2.3.4 Transient equivalent circuit model

The steady-state equivalent circuit model derived in the previous session is constructed based upon (2.14) wherein time is not involved. A question arises as to the rate at which space charge accumulates within the dielectric. To address this question, the concept of an equivalent electric circuit is again used. However, in contrast to the relationship between electric current density and electric field, the focus of the analysis is on the electric flux density. This is highlighted using the flux tube geometry shown in Fig.2.10, wherein lines of electric flux density are shown. As with the electric flux tube used for steady state analysis, the two ends of the tube are equipotential surfaces. It is assumed that lines of electric flux density penetrate the end surfaces orthogonally and that there is no divergence of the electric flux density within the tube. The relationship between the electric flux density and the electric field at any point within the tube is expressed in (2.9).

It is noted that in general, the quantities *D* and *E* are vector fields. Within electrostatics, the total number of electric flux lines are often quantified to enable one to work with scalar quantities, rather than vectors. This is accomplished using the defined relation:

$$Q = \int \vec{D} \cdot d\vec{S} = \int \varepsilon \vec{E} \cdot d\vec{S} \tag{2.34}$$

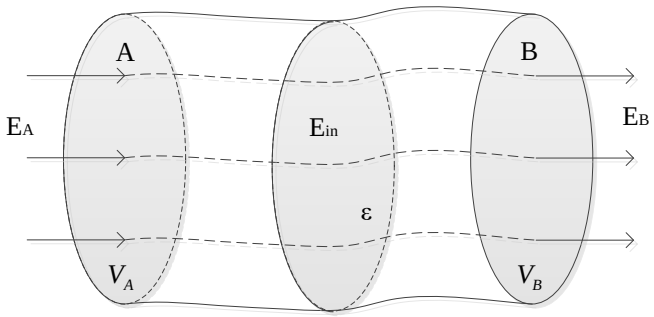

Fig.2.10 Electric flux tube

where Q has a unit of charge. The total electric flux Q can be used to calculate an equivalent capacitance of the tube, using the relationship

$$C = \frac{Q}{V} \tag{2.35}$$

where the voltage V is the electric potential drop across the electric tube which is calculated using the integral form of (2.7).

$$V = \int_B^A E \cdot dl = V_A - V_B \tag{2.36}$$

The equivalent capacitor model based on the equation (2.35) can then be shown in Fig.2.11.

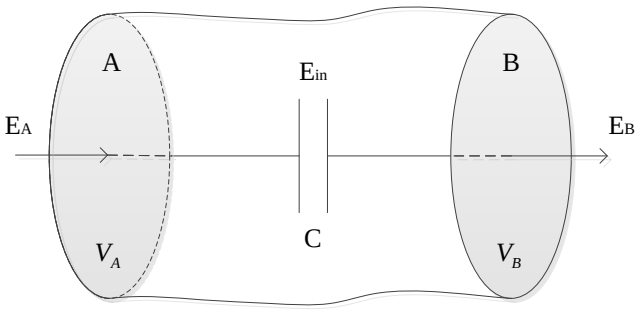

Fig.2.11 Equivalent capacitor tube

Considering the quantities in (2.35) and (2.36), an approach to calculate the capacitance is to solve the steady-state circuit model, establish the voltage at the ends of the flux tubes, integrate the electric field obtained over the surface of the flux tube at its midpoint, and divide the respective results. Although possible, if permittivity is constant, capacitance does not change with the electric field. Therefore, one can establish the values of capacitance apriori through a straightforward evaluation of each flux tube. For the coaxial cable with a discretization of ring tubes shown in Fig.2.12, one can establish that a ring element will have differential capacitance.

$$\frac{1}{dC} = \frac{Edr}{2\pi\varepsilon r l_d E} \tag{2.37}$$

It is noted that the electric field shown in the differential equation (2.37) of inverse capacitance can be canceled in the numerator and denominator. Therefore, the inverse capacitance can be found by integrating the equation (2.37) from the beginning to the end radius of each tube.

$$\frac{1}{C} = \int_{r_{sp,n}}^{r_{ep,n}} \frac{dr}{2\pi\varepsilon l_d r} = \frac{\ln(\frac{r_{ep,n}}{r_{sp,n}})}{2\pi\varepsilon l_d} \tag{2.38}$$

With a discretized ring shape layer of the dielectric layer in Fig.2.12 and (2.38), the capacitance of each layer can be expressed as,

$$C = \frac{2\pi\varepsilon l_d}{\ln(\frac{r_{ep,n}}{r_{sp,n}})} \tag{2.39}$$

Where n stands for the n^{th} electric tube.

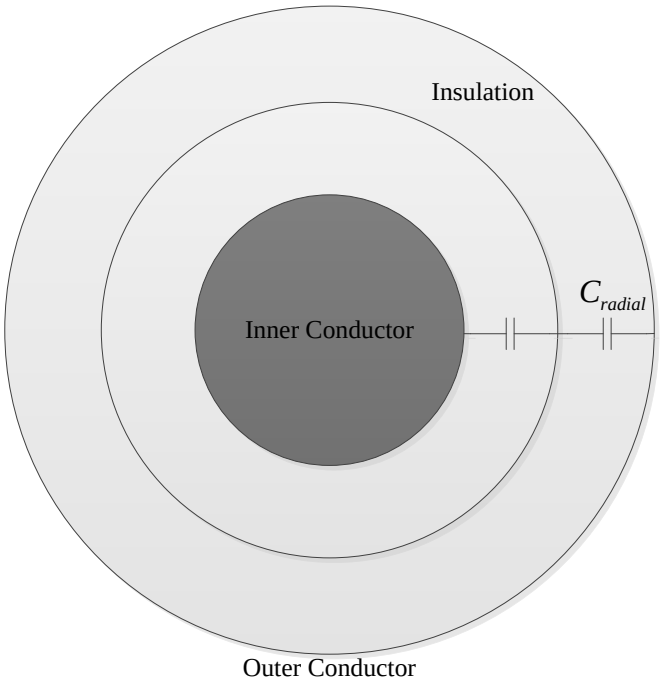

Fig.2.12 Equivalent capacitor configuration

Based upon the flux tube derivations, an RC parallel circuit illustrated in Fig.2.13 is proposed to construct an equivalent circuit model to represent the dynamics of the electric field within the dielectric. Prior to continuing the derivation to consider space charge calculation, it is convenient to consider the proposed model in the context of the field equations. Specifically, from Fig.2.13, one can express

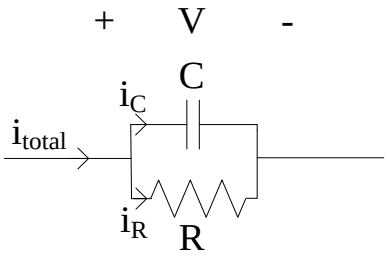

Fig.2.13 A RC circuit

$$i_R + i_C = i_{total} \tag{2.40}$$

The currents in the resistor and capacitor can be expressed as,

$$i_R = \frac{V}{R} \tag{2.41}$$

$$i_C = C\frac{dV}{dt} \tag{2.42}$$

Equation (2.40) to (2.42) can be combined as follows,

$$\frac{V}{R} + C\frac{dV}{dt} = i_{total} \tag{2.43}$$

If one considers the homogeneous solution to (2.43) and substitutes (2.27) and (2.39) for the resistor and capacitor values, one obtains

$$\frac{(2\pi l_d)\sigma}{\ln(\frac{r_{ep,n}}{r_{sp,n}})}V + \frac{(2\pi l_d)\varepsilon}{\ln(\frac{r_{ep,n}}{r_{sp,n}})}\frac{dV}{dt} = 0 \tag{2.44}$$

Collecting like terms and taking the Laplacian of both sides yields

$$\nabla \cdot \nabla \frac{2\pi l_d}{\ln(\frac{r_{ep,n}}{r_{sp,n}})}(\sigma V + \varepsilon \frac{dV}{dt}) = 0 \tag{2.45}$$

Since geometric term is constant for each layer, it is convenient to move the geometric term out of the Laplacian operator.

$$\frac{2\pi l_d}{\ln(\frac{r_{ep,n}}{r_{sp,n}})}(\nabla \cdot \nabla(\sigma V) + \varepsilon \frac{d(\nabla \cdot \nabla V)}{dt}) = 0 \tag{2.46}$$

which shows consistency with (2.14).

Herein, the RC circuit model shown in Fig.2.13 is applied to the coaxial cable design shown in Fig.2.14, where each layer of the dielectric tube contains a parallel RC pair. The electrical performance of the coaxial cable under an operating condition is readily analyzed using basic circuit analysis.

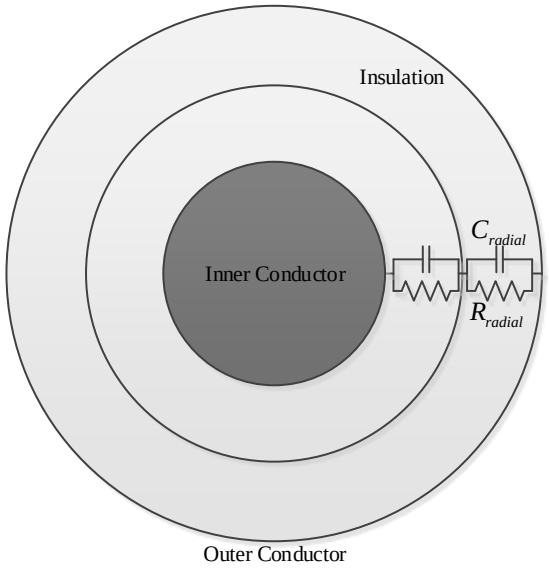

Fig.2.14 RC circuit based coaxial cable

Several researchers have expressed a desire to compute the space charge distribution within regions of the dielectric [1][2][8][9][10][11][16][20][23][24][28]. A common method to establish the space charge is to relate volumetric charge to the predicted conductivity using:

$$\rho = \nabla \cdot \left(\varepsilon \frac{j}{\sigma} \right) = -\frac{\varepsilon}{\sigma} \frac{\partial \rho}{\partial t} + j \nabla \cdot \left(\frac{\varepsilon}{\sigma} \right) \tag{2.47}$$

This requires numerical differentiation. An alternative approach using the electric flux tube is proposed here to predict the space charge distribution.

Considering the derivations above, the electric tubes that relate J and E and D and E both assume that the divergence of the electric field is zero within the tube. An implication of the model is that the space charge that does accumulate is represented at the tube boundaries. Therefore, the volumetric space charge distribution is taken as a surface charge between two adjacent electric tubes as shown in Fig.2.15. A volumetric space charge and the surface charge can be constructed based upon the geometry of the electric tubes.

$$Q_{sp} = \iiint \rho_V \cdot dV_\Omega = \iint \rho_s \cdot dS \tag{2.48}$$

where ρ_V and ρ_S are the volumetric and surface charge density respectively. The total space charge Q_{sp} enclosed in a volume can be expressed using the integral form of Gauss's Law:

$$Q_{sp} = \iiint \rho_V \cdot dV_\Omega = \oiint \varepsilon \vec{E} \cdot d\vec{S}_\Omega \tag{2.49}$$

where Ω is the enclosed shaded volume highlighted in Fig.2.15 specifically.

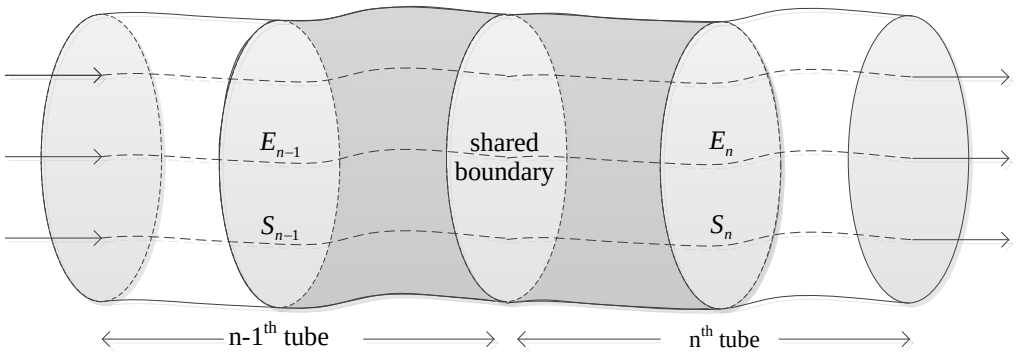

Fig.2.15 Two adjacent electric tubes

To consider the space charge Q_{sp}, one can analyze the volume bounded by midpoints of two adjacent electric tubes as shown in Fig.2.15. The space charge is calculated by integrating the electric flux over the surface area shown. Specifically, for the n-1th and nth tube:

$$Q_{sp,n} = \varepsilon(\iint_{\bar{S}_{n-1}} \vec{E}_{n-1} \cdot d\vec{S}_{n-1} + \iint_{\bar{S}_n} \vec{E}_n \cdot d\vec{S}_n + \iint_{\bar{S}_{side,n-1}} \vec{E}_{side,n-1} \cdot d\vec{S}_{side,n-1} + \iint_{\bar{S}_{side,n}} \vec{E}_{side,n} \cdot d\vec{S}_{side,n})$$

(2.50)

where $\vec{S}_{n-1}$, $\vec{S}_n$, $\vec{S}_{side,n-1}$ and $\vec{S}_{side,n}$ are the midpoint and side surface of n-1th and nth electric tube respectively and all pointing outwards from the respective tube surface. The side surface integral leads to zero due to the assumption that the divergence of electric flux within the tubes is zero. Hence, the total charge can be expressed.

$$Q_{sp,n} = \varepsilon(\iint_{\bar{S}_{n-1}} \vec{E}_{n-1} \cdot d\vec{S}_{n-1} + \iint_{\bar{S}_n} \vec{E}_n \cdot d\vec{S}_n) \tag{2.51}$$

Under the assumption that all electric flux penetrates the end surface (two equipotential surfaces) orthogonally, the dot operation of the two terms can be simplified:

$$Q_{sp,n} = \varepsilon(E_n \cdot S_n - E_{n-1} \cdot S_{n-1}) \tag{2.52}$$

Hence, the space charge enclosed by the midpoints of two adjacent tubes is calculated by the electric field and the surface area of the respective locations. The product of the electric field and

the surface area can be acquired from the total flux equation of the equivalent capacitor stated in (2.34).

$$Q_n = \varepsilon E_n \cdot S_n \tag{2.53}$$

$$S_n = 2\pi r_n l_d \tag{2.54}$$

where S_n is the cross-sectional area at each midpoint of each electric flux tube. Hence, the total space charge enclosed can be accomplished by substituting equation (2.53) into (2.52).

$$Q_{sp,n} = Q_n - Q_{n-1} \tag{2.55}$$

With the transient equivalent circuit model shown in this chapter, the space charge can be further expressed using (2.35).

$$Q_{sp,n} = C_n V_n - C_{n-1} V_{n-1} \tag{2.56}$$

where C_n and V_n are the capacitance and the capacitor voltage of the nth tube. The volumetric space charge can be calculated by combining the total space charge in equation (2.56) and equation (2.48), yielding:

$$\rho_{V,n} = \frac{Q_{sp,n}}{V_{sp,n}} \tag{2.57}$$

For the case of a coaxial conductor using the ring tubes, the volume $Vol_{sp,n}$ of the nth tube can be expressed.

$$Vol_{sp,n} = \int_0^{l_d} \int_0^{2\pi} \int_{r_{md,n-1}}^{r_{md,n}} r dr d\theta dz \tag{2.58}$$

$$Vol_{sp,n} = \pi l_d \left(r_{md,n}^2 - r_{md,n-1}^2 \right) \tag{2.59}$$

where $r_{md,n}$ is the midpoint of the radius of the respective tube.

$$r_{md,n} = \frac{r_{sp,n} + r_{ep,n}}{2} \tag{2.60}$$

The volumetric space charge distribution can be calculated based on the equation (2.57) and (2.59).

2.3.5 Transient-state electrical equivalent circuit validation

The transient analysis based on the coaxial cable has been established using the RC model shown in Fig.2.16. As shown, each layer of electric tube is represented with an RC branch. A small resistor is placed in series with a voltage source for the purpose of representing the source. The state model of the system is expressed by first starting with each tube capacitor current,

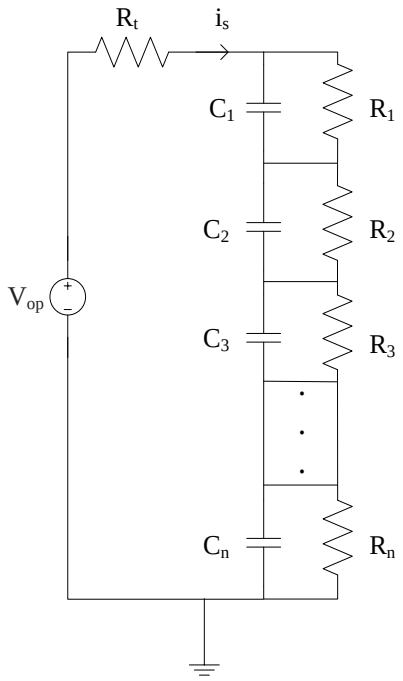

Fig.2.16 RC equivalent circuit model of co-axial cable

$$\frac{dv_{c,n}}{dt} = \frac{i_{c,n}}{C_n} \tag{2.61}$$

where $i_{c,n}$ represents the capacitor current that can be expressed as,

$$i_{c,n} = \frac{V_{op} - \sum_{n=1}^{N} v_{c,n}}{R_t} - \frac{v_{c,n}}{R_n} \tag{2.62}$$

Substituting (2.62) into (2.61) the state model for each capacitor voltage is expressed as:

$$\left(\frac{dv}{dt}\right)_{c,n} = \frac{V_{op} - \sum_{n=1}^{N} v_{c,n}}{C_n R_t} - \frac{v_{c,n}}{C_n R_n} \tag{2.63}$$

In this research, the state model is initially solved using a forward Euler integration algorithm,

$$v_{c,n}^{k+1} = v_{c,n}^{k} + dt\left(\frac{dv}{dt}\right)_{c,n}^{k} \tag{2.64}$$

where here, the superscript k is used to denote the index of time. The selection of a Forward Euler algorithm is considered in the next section. Once the capacitor voltage of each tube is solved, the electric field is updated by solving the nonlinear equation:

$$E_n = \frac{v_{c,n}}{\sigma_n(E,T) R_n(E,T) S_n} \tag{2.65}$$

where the conductivity is expressed in (2.16) to (2.18). Subsequently, the equivalent resistance R_n is updated using (2.27)

$$R_n = \frac{\ln(\frac{r_{ep,n}}{r_{sp.n}})}{\sigma_n 2\pi l_d} \tag{2.66}$$

Three approaches have been considered to solve the nonlinear equation and are described in the next section.

A block diagram to realize the circuit development is provided in Fig.2.17. Similar to the steady-state equivalent circuit, both geometric/electrical parameters and thermal condition are initialized. A proper time step is selected and tested for the initial stability test which will be discussed in next section. After the initialization, the state model of the capacitor voltage is updated

using (2.62)-(2.65). Subsequently, the conductivity and resistance is updated using (2.16) - (2.18) and (2.66). In design studies where there is a desire to calculate a response until a steady state is reached, the difference of the voltage between successive time steps is used to determine a stopping time.

$$\left| v_{c,n}^{k+1} - v_{c,n}^{k} \right| < e_{\max,step} \tag{2.67}$$

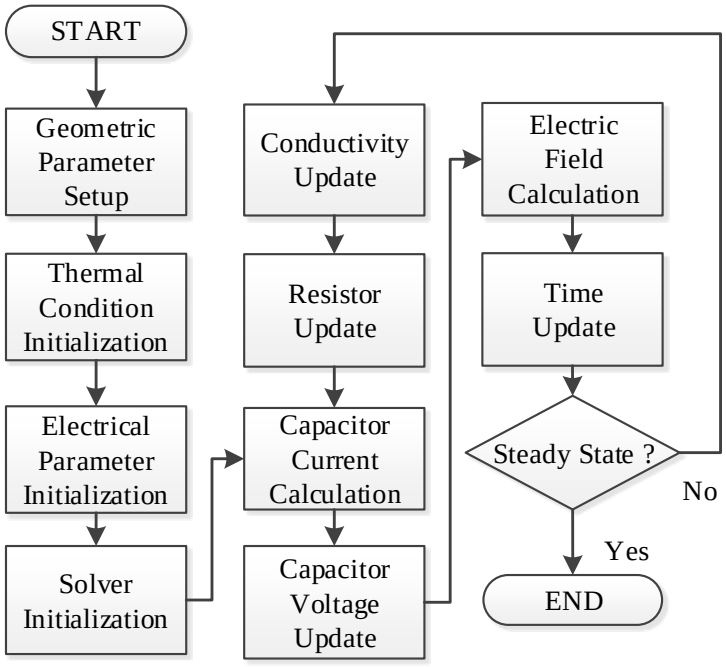

Fig.2.17 Block diagram for RC circuit model

To validate the approach, the cable studied under steady-state operation is used to evaluate the transient circuit model. The cable parameters are identical to those provided in [8]. For the study, the cable is initially de-energized and assumed to operate at an ambient condition of 19 ^{o}C. At t = 0 s, a 600 kV is applied between the center and outer conductors. It is assumed the center conductor is carrying a current of 1600 A. The temperature within the dielectric for time greater than zero is assumed to be a steady state value (34 ^{o}C at the inner boundary) obtained from the thermal equivalent circuit.

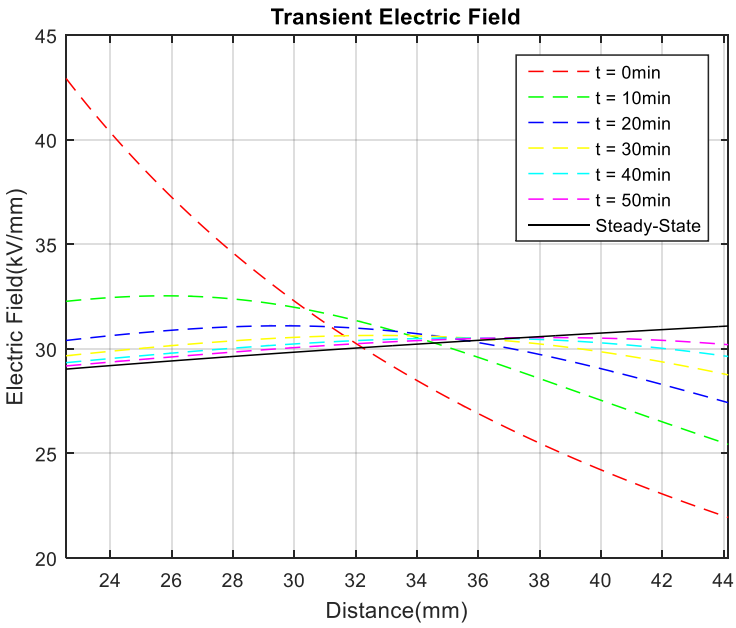

Fig.2.18 Transient electric field distribution

It is noted from the results that at t = 0, the electric field has the expected logarithmic shape that is predicted under conditions of zero temperature gradient and hence uniform conductivity. As time continues, one can see that the electric field undergoes an inversion. Shown in Fig.2.18 is the expected steady-state value (black) obtained with the steady-state resistive model. One can observe that the dynamic circuit approaches the steady state within roughly 60 min. A similar study was repeated for different current levels. The final steady-state electric field obtained by the equivalent circuit is compared with those provided in [8] in Fig.2.19.

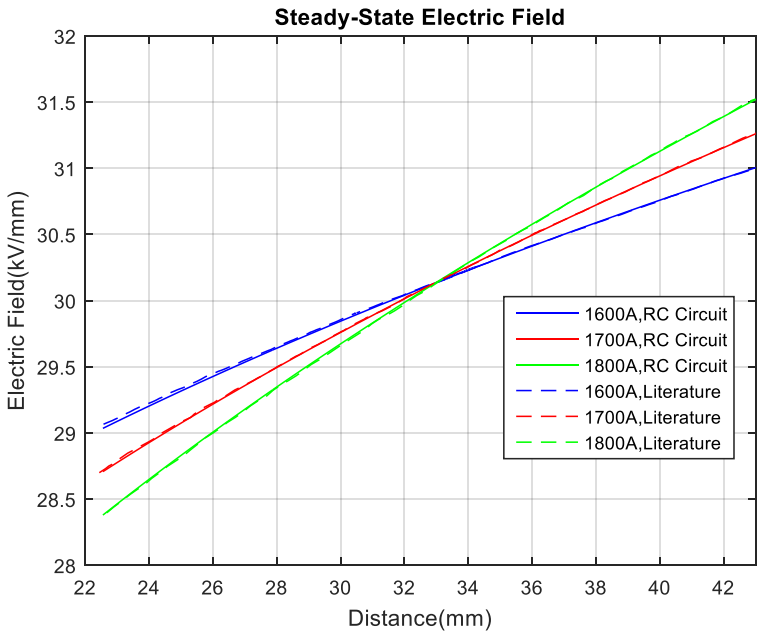

Fig.2.19 Steady state comparison for RC circuit model

The RC circuit model can further be validated using a second study that is described in [11]. Under this case, the cable parameters and operating conditions are shown in Table 2.2. At t = 0, conditions are similar to that above. Fig.2.20 shows that the electric field derived from the proposed RC circuit model has the similar results with the solutions in the literature [11] and steady state equivalent circuit model described in Fig.2.21. A space charge distribution is also compared and shown in Fig.2.22. It is noted that the higher temperature creates more space charge, as expected. The charge-induced field further distorts the original electric field and enhances the field inversion effect as shown in Fig.2.21.

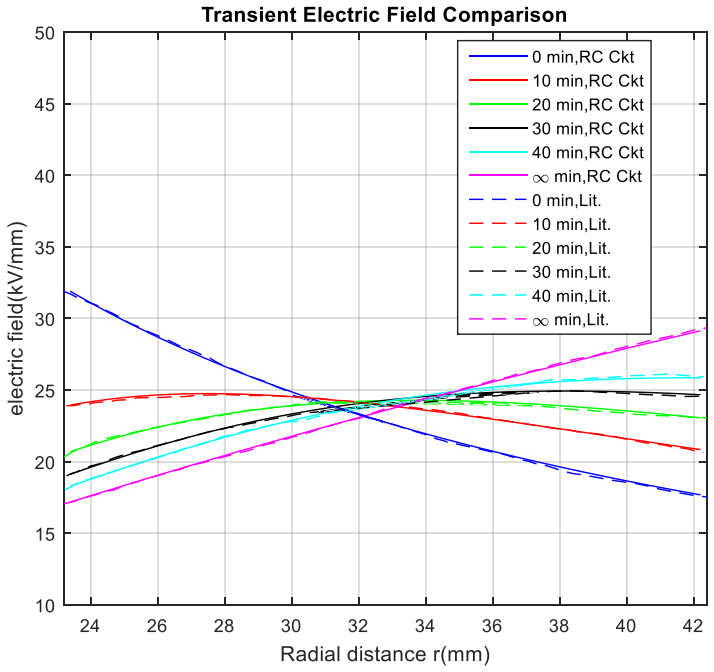

Fig.2.20 Transient electric field distribution

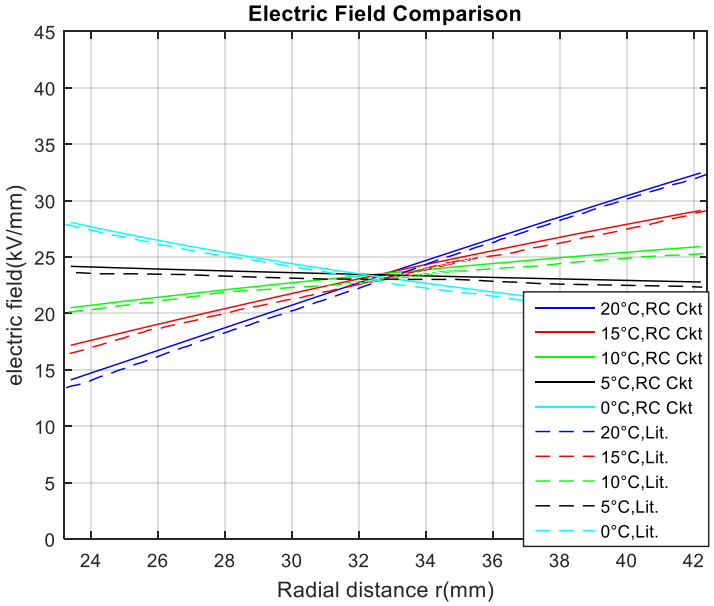

Fig.2.21 Steady state comparison for RC circuit model

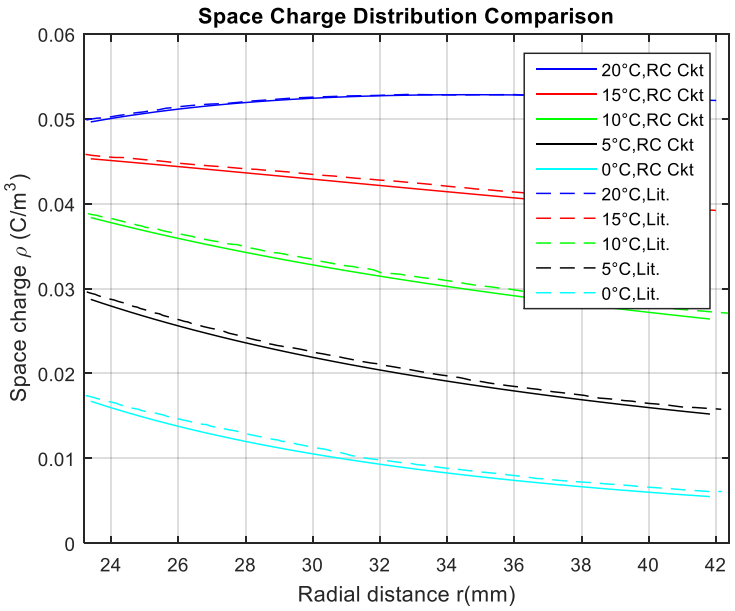

Fig.2.22 Space charge comparison for RC circuit model

Since the voltage reversal is a concern in cable design [1][3][11][15], a voltage reversal effect can also be examined and compared with the literature. Shown in Fig.2.23 are a simple result using the cable parameters in Table 2.2. The cable experiences a voltage reversal after operating in a steady state condition while current stays, or temperature stays unchanged.

From the capacitor model expressed in (2.39), the capacitance of each layer increases from the inner radius to the outer radius since it is only a function of geometric term $1/\ln\left(r_{ep,n}/r_{sp,n}\right)$. However, the resistance (2.27) of each layer is a combined effect of geometric term $\ln\left(r_{ep,n}/r_{sp,n}\right)$ and conductivity $\sigma\left(r,T,E\right)$, which increases with temperature and electric field. In the actual circuit simulation as in Reddy and Jeroense's case study [8][11], resistance increases with the radius. This is because a temperature gradient is present and it plays the dominant role in the conductivity. In the steady state, there is no current flow in the capacitor branches of the model. According to Kirchhoff's Voltage Law, the larger resistance near the outer radius shares more

applied voltage, which subsequently can be used to find the steady-state electric field as shown in Fig.2.23. The field inversion effect can be clearly seen in Fig.2.23 (a) by the resistance distribution.

With the reversed applied voltage, the branch voltage near the inner boundary drops much faster than the branch voltage near the outer boundary as shown in Fig.2.23 (a) and in detail Fig.2.23 (b). An explanation can be shown here based on the RC circuit analysis. It can be shown that the time constant of each RC branch are different. These are listed in Table 2.3, for a discretization of ten flux tubes. One can notice that the time constant of branch 10 is roughly 3 times of that of branch 1. Although time constants vary by a small amount at each time step, the range of the time constants and the ratio of branch 1 to branch 10 remains relatively constant, which can be seen in Fig.2.23 (a). Furthermore, with the lower steady-state voltage in branch 1, it experiences a larger voltage drop due to a smaller time constant compared to branch 10. This may lead to an appreciable drop into the negative range with a corresponding large magnitude of electric field. The transient captures of the electric field distribution within the dielectric are shown in Fig.2.23 (c) and are recorded at every 0.1s.

Interestingly, the space charge does not encounter the sudden change due to the voltage reversal shown in Fig.2.23 (d). Researchers suggest that the steady state of the electric field consists of two parts, the space charge induced field and the voltage induced field [1][11][28][30]. The space charge is a long-term effect caused by the variation in the conductivity. Hence, the space charge induced field does not change at the initial stage of the voltage reversal. Instead, the time constant of the RC circuit describes the behavior of the space charge development. The initial electric field change during the voltage reversal effect is dependent primarily on the external voltage.

An attempt to solve for the initial electric field change is as follows. The voltage induced field does not include effects of space charge. Hence, the voltage induced electric field can be derived by combining (2.7) - (2.9).

$$\nabla \cdot (\nabla V) = \nabla^2 V = -\frac{\rho}{\varepsilon} = 0 \tag{2.68}$$

Using cylindrical coordinates, the Laplacian of V and divergence of E can be shown to be only dependent on radial components in coaxial cable for example.

$$\nabla^2 V = \frac{1}{\rho}\frac{\partial}{\partial \rho}\left(\rho \frac{\partial V}{\partial \rho}\right) + \frac{1}{\rho^2}\frac{\partial^2 V}{\partial \varphi^2} + \frac{\partial^2 V}{\partial z^2} = \frac{1}{\rho}\frac{\partial}{\partial \rho}\left(\rho \frac{\partial V}{\partial \rho}\right) = 0 \tag{2.69}$$

$$\nabla \cdot E = \frac{1}{r}\frac{\partial}{\partial r}(rE_r) + \frac{1}{r}\frac{\partial E_\theta}{\partial \theta} + \frac{\partial E_Z}{\partial Z} = \frac{1}{r}\frac{\partial}{\partial r}(rE_r) \tag{2.70}$$

By integrating (2.69) twice from r_{in} to r_{out} and substituting boundaries conditions in (2.71), the voltage distribution can be derived in (2.72).

$$\begin{cases} V(r_{in}) = V_{in} \\ V(r_{out}) = 0 \end{cases} \tag{2.71}$$

$$V(r) = \frac{-V_{in}\ln(r)}{\ln\left(\frac{r_{out}}{r_{in}}\right)} + \frac{V_{in}\ln(r_{out})}{\ln\left(\frac{r_{out}}{r_{in}}\right)} \tag{2.72}$$

The electric field can be then derived by taking divergent of V using (2.7),

$$E(r) = \frac{V_{in}}{r\ln\left(\frac{r_{out}}{r_{in}}\right)} \tag{2.73}$$

In the case of voltage reversal, the voltage induced electric field changes from positive V_{in} to negative V_{in}. The total voltage induced field change $\Delta E_{voltage}$ due to the voltage reversal is expressed.

$$\Delta E_{voltage}(r) = \frac{2V_{in}}{r \ln\left(\frac{r_{out}}{r_{in}}\right)} \tag{2.74}$$

This expression indicates that the maximum electric field change occurs at the inner boundary where it is the lowest value in a steady state operation. Thus, it would appear that both conditions (the steady-state electric field and the voltage reversal) must be used to assess the electric field related stresses within a dielectric.

Table 2.3 Details on Steady State RC Branches

Branch No.	R_n(GΩ)	C_n(nF)	τ_n(min)
1	548.34	2.45	22.39
2	590.54	2.65	26.03
3	631.55	2.84	29.89
4	671.39	3.03	33.95
5	710.10	3.23	38.22
6	747.73	3.42	42.67
7	784.32	3.62	47.30
8	819.92	3.81	52.11
9	854.59	4.01	57.08
10	888.40	4.20	62.23

Fig.2.23 Continued

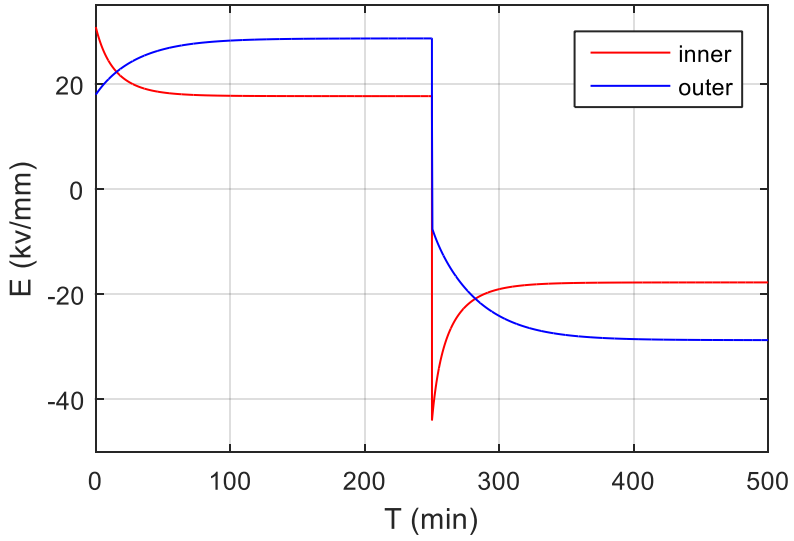

Fig.2.23 (a) Transient performance of electric field at two boundaries

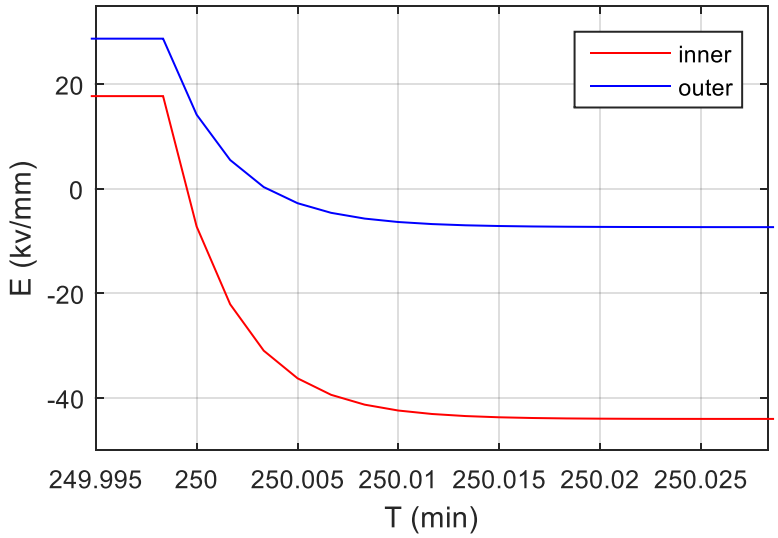

Fig.2.23 (b) Details on voltage reversal point

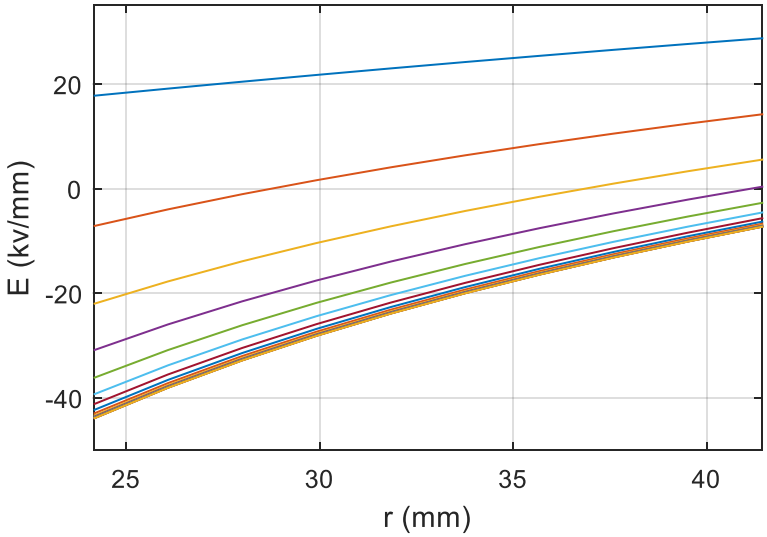

Fig.2.23 (c) Captures of transient electric field distribution

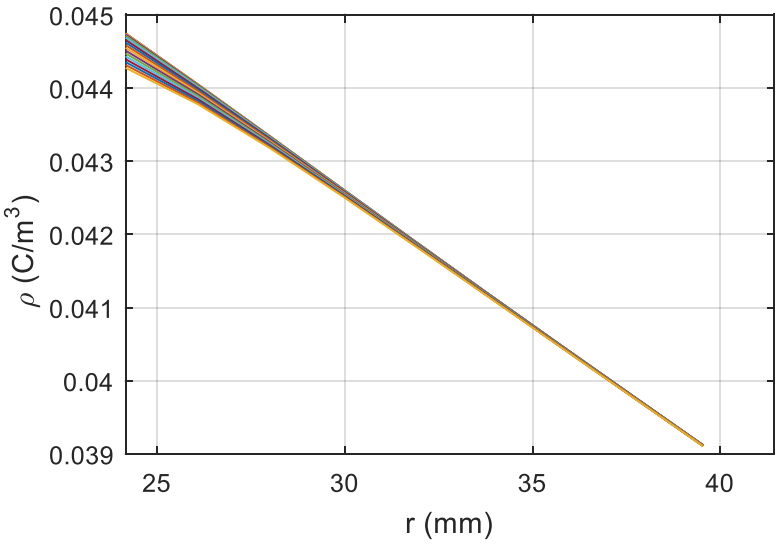

Fig.2.23(d) Captures of transient space charge distribution

Fig.2.23 Voltage reversal effect

2.3.6 Selection of solvers

2.3.6.1 Nonlinear solver approaches for electric field calculation

As shown in (2.63), the electric field is a nonlinear function of conductivity:

$$f(\mathbf{E}) = \mathbf{E} - \frac{\mathbf{v}_c^k}{\boldsymbol{\sigma}(\mathbf{E},\mathbf{T})\mathbf{R}(\mathbf{E},\mathbf{T})\mathbf{S}} = 0? \tag{2.75}$$

Attempting to solve (2.75) iteratively requires considerable computational effort due to electric field dependent conductivity and resistance. In this research, two approaches to approximate the solution without iteration have been attempted. In the first, (2.65) is solved directly using the value of conductivity and current density from the previous time step shown in (2.76). Specifically, the electric field is calculated using the conductivity from the previous time step, i.e.

$$E_n^k = \frac{J_n^{k-1}}{\sigma_n^{k-1}} = \frac{v_{c,n}^{k-1}}{\sigma_n^{k-1} R_{c,n}^{k-1} S_n} \tag{2.76}$$

A second approach is to assume the electric field is constant over the length of the flux tube, and therefore solved using (2.36), wherein:

$$E_n^k = \frac{v_{c,n}^k}{r_{ep,n} - r_{sp,n}} \tag{2.77}$$

The first and second approximate methods are called resistor and capacitor based approximate method respectively for further reference.

2.3.6.2 Integration approaches for state update with ordinary differential equations

Two approaches to solve the state model of (2.63) are provided for comparison and evaluation for error and efficiency. The first approach utilizes a Forward Euler algorithm:

$$v_{c,n}^{k+1} = v_{c,n}^{k} + h\left(\frac{dv}{dt}\right)_{c,n}^{k} = v_{c,n}^{k} + h\left(\frac{V_{op} - \sum_{n=1}^{N} v_{c,n}^{k}}{C_n R_t} - \frac{v_{c,n}^{k}}{C_n R_n^{k}}\right) \tag{2.78}$$

where h stands for the time step. The second approach utilizes a Fourth-Order Runge-Kutta algorithm, which has the form as below.

$$\frac{dx^k}{dt} = f(x^k, t^k) \tag{2.79}$$

$$x^{k+1} = x^k + \frac{1}{6}\left(F_1^k + 2F_2^k + 2F_3^k + F_4^k\right) \tag{2.80}$$

where

$$\begin{cases} F_1^k = hf(x^k, t^k) \\ F_2^k = hf(x^k + \frac{1}{2}F_1^k, t^k + \frac{1}{2}h) \\ F_3^k = hf(x^k + \frac{1}{2}F_2^k, t^k + \frac{1}{2}h) \\ F_4^k = hf(x^k + F_3^k, t^k + h) \end{cases} \tag{2.81}$$

The variable *x* stands for capacitor voltage of the each tube in the equivalent circuit model. Hence, the function *f* and the updated voltage can be shown by substituting (2.63) into (2.79) and (2.80),

$$f(v_{c,n}^k, t^k) = \left(\frac{dv}{dt}\right)_{c,n}^{k} = \frac{V_{op} - \sum_{n=1}^{N} v_{c,n}^{k}}{C_n R_t} - \frac{v_{c,n}^{k}}{C_n R_n^{k}} \tag{2.82}$$

$$v_{c,n}^{k+1} = v_{c,n}^{k} + \frac{1}{6}\left(F_{1,n}^k + 2F_{2,n}^k + 2F_{3,n}^k + F_{4,n}^k\right) \tag{2.83}$$

where the four higher order terms are shown as:

$$\begin{cases} F_{1,n}^{k} = hf\left(v_{c,n}^{k}, t^{k}\right) \\ F_{2,n}^{k} = hf\left(v_{c,n}^{k} + \frac{1}{2}F_{1,n}^{k}, t^{k} + \frac{1}{2}h\right) \\ F_{3,n}^{k} = hf\left(v_{c,n}^{k} + \frac{1}{2}F_{2,n}^{k}, t^{k} + \frac{1}{2}h\right) \\ F_{4,n}^{k} = hf\left(v_{c,n}^{k} + F_{3,n}^{k}, t^{k} + h\right) \end{cases} \tag{2.84}$$

It is noted that since the resistance in (2.82) is dependent on the electric field, higher order term calculation in (2.84) requires a nonlinear solve using (2.75). However, to reduce computational effort, two simplified approaches have been proposed to approximate the resistance. The first approach is based on the approximate electric field calculation method stated in (2.76) or (2.77) where the approximate electric field is calculated using resistor or capacitor model and then applied to the intermediate resistance calculation. The approximate electric field is updated during the construction of the four higher order terms in (2.84). Subsequently, the resistance is calculated based on the updated electric field dependent conductivity via (2.66). The second approximate method is aimed to further reduce the computational stress by assuming a constant resistance during the construction of the four higher order terms. No calculation is required for the resistance update due to the assumption that no appreciable variation in electric field dependent resistance will occur over a small increment in the state variable. Hence, the four higher order term are constructed directly.

2.3.6.3 Solver implementation and comparisons

Two different types of solver implementation are shown in Fig.2.24 based on the integration algorithm with the Forward Euler's Method and the Fourth-Order Runge-Kutta Method on the left and right respectively.

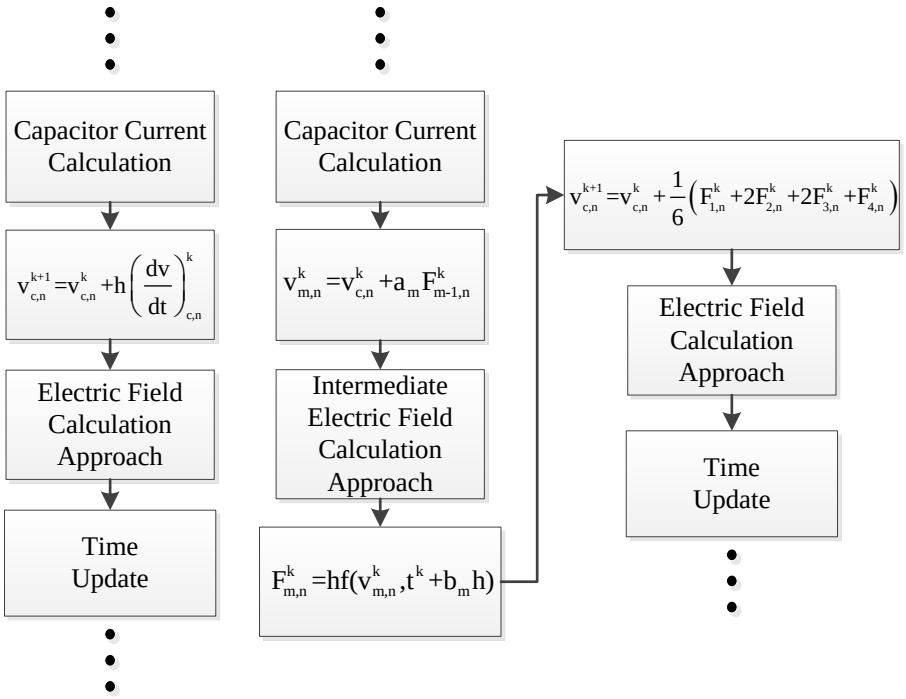

Fig.2.24 Solver implementation flow chart

The error analysis has been examined based upon the results from the approximated approaches compared to the most accurate model with the iterative method of a nonlinear solver and Fourth-Order Runge-Katta Method. The maximum absolute relative error equation is provided.

$$\epsilon_{abs,\max}^{k}=\max\left(\left|\frac{E_{mtd}^{k}-E_{nlr}^{k}}{E_{nlr}^{k}}\right|\right)\times 100\% \tag{2.85}$$

where $\epsilon_{abs,\max}^{k}$, E_{mtd}^{k} and E_{nlr}^{k} represents the maximum absolute relative error, the electric field from the approximation method and the electric field from the nonlinear solver respectively. The maximum error table are provided for comparison shown in Table 2.4.

To compare the computational stress, the ratio of the run time compared to the length of time simulated is provided.

$$\eta = \frac{t_{real}}{t_{simulated}} \times 100\% \tag{2.86}$$

The run time is calculated using the Matlab commands '*tic*' and '*toc*' at the simulation time initiation and termination respectively. It is noted that these values are meant to provide a relative comparison between approaches, since the run time may vary from computer to computer due to the capabilities of the machine utilized. For all computational studies, the cable in Jeorense's case study [11] with parameters shown in Table 2.2 is used. The approximate approaches illustrated in Chapt.2.3.6.1 and Chapt.2.3.6.2 have been implemented. Each model is simulated with a time step of 0.1s and the total simulation time of 200 minutes.

Among the iterative approaches 1-4, the electric field is calculated based on the iterative algorithm while different ODE solvers and intermediate electric field approaches are selected for comparisons. It is noted that the iterative method significantly increases the calculation time. It is also noted that the non-iterative solutions in the iterative approach 1 to 4 yield results similar to the solutions acquired using an iterative approach. Furthermore, the calculation time required for the non-iterative methods is much less than the iterative solution among the iterative approach 1-4. The electric field calculated in the iterative approach 1 using the resistor approach in (2.76) is established based on the electrical properties from the previous step which hence accumulates a relatively larger error compared to the capacitor approach calculated in the iterative approach 2 using (2.77). The iterative approach 3 with the constant intermediate electric field further reduces the calculation time compared to the iterative approach 1 and 2 due to no intermediate electric field evaluation and update but also accumulates a large error due to no electric field update in the ODE solver. The Euler's method in the iterative approach 4 further reduce the ODE calculation procedure but, on the other hand, deviates the solutions compared to the Runge-Kutta method.

To further analyze the potentials of the non-iterative method, 6 non-iterative approaches are given based on the non-iterative method implementation. One can notice that it significantly reduces the computational effort using the non-iterative approach 1 to 6 while the maximum error increases accordingly due to the double non-iterative method. Among the non-iterative approach, Runge-Kutta 4th Order does not gain advantage over Forward Euler's Method. Hence, based upon the tradeoff between the error and computational effort, the non-iterative approach 6 has been adopted for the further circuit construction and optimization.

Table 2.4 The Comparison of Different Approaches

	ODE solver	Electric field solver in ODE solver	Electric field solver	Error Comparison	η
accurate approach	RK4	iterative	iterative	N.A	88.46%
iterative approach 1	RK4	resistor	iterative	7.37×10^{-4}%	28%
iterative approach 2	RK4	capacitor	iterative	4.79×10^{-4}%	28.03%
iterative approach 3	RK4	N.A	iterative	7.37×10^{-4}%	27.59%
iterative approach 4	Euler	N.A	iterative	16.6×10^{-4}%	27.46%
non-iterative approach 1	RK4	resistor	resistor	114×10^{-4}%	8.892×10^{-4}%
non-iterative approach 2	RK4	capacitor	capacitor	22.5×10^{-4}%	8.917×10^{-4}%
non-iterative approach 3	RK4	N.A	resistor	114×10^{-4}%	5.967×10^{-4}%
non-iterative approach 4	RK4	N.A	capacitor	22.4×10^{-4}%	6.417×10^{-4}%
non-iterative approach 5	Euler	N.A	resistor	114×10^{-4}%	2.583×10^{-4}%
non-iterative approach 6	Euler	N.A	capacitor	22.2×10^{-4}%	3.250×10^{-4}%

2.3.6.4 Time step selection and the stability analysis of ODEs

The selection of time step is crucial to the model accuracy and efficiency. The time step is examined with the integral algorithm demonstrated in (2.78) to (2.84). It is noted the source has a relatively small source resistor, which can influence the time step selection. The selection criteria is constructed using a Forward Euler's Method based on the previous conclusion. By rearranging the update evaluation of the Forward Euler's Method in (2.78), it is shown that

$$v_{c,n}^{k+1} = v_{c,n}^{k} + h\left(\frac{dv}{dt}\right)_{c,n}^{k} = v_{c,n}^{k} + \frac{h}{R_t}\frac{V_{op}}{C_n} - \frac{h}{R_t}\frac{\sum_{n=1}^{N} v_{c,n}^{k}}{C_n} - \frac{h}{R_n^k}\frac{v_{c,n}^{k}}{C_n} \tag{2.87}$$

It is noted that the second term and third term are dependent on the ratio of the time step and the source resistor. Based on the discrete-time system characteristic equation, the forward Euler's method in (2.87) can be summarized in a matrix form, which yields,

$$\mathbf{v}_c^{k+1} = \mathbf{A}^k \mathbf{v}_c^k + \mathbf{B}\mathbf{V}_{op} \tag{2.88}$$

where **A** and **B** represent the coefficient matrix for general solution and the coefficient matrix for particular solution corresponding to the voltage source respectively which are expressed as:

$$\mathbf{A}^k = \begin{bmatrix} 1-\frac{h}{C_1R_t}-\frac{h}{C_1R_1^k} & -\frac{h}{C_1R_t} & \cdots & -\frac{h}{C_1R_t} & -\frac{h}{C_1R_t} \\ -\frac{h}{C_2R_2^k} & 1-\frac{h}{C_2R_t}-\frac{h}{C_2R_2^k} & -\frac{h}{C_2R_2^k} & -\frac{h}{C_2R_2^k} & -\frac{h}{C_2R_2^k} \\ \vdots & & \ddots & & \vdots \\ -\frac{h}{C_{N-1}R_t} & -\frac{h}{C_{N-1}R_t} & -\frac{h}{C_{N-1}R_t} & 1-\frac{h}{C_{N-1}R_t}-\frac{h}{C_{N-1}R_{N-1}^k} & -\frac{h}{C_{N-1}R_t} \\ -\frac{h}{C_NR_N^k} & -\frac{h}{C_NR_N^k} & \cdots & -\frac{h}{C_NR_N^k} & 1-\frac{h}{C_NR_t}-\frac{h}{C_NR_N^k} \end{bmatrix} \tag{2.89}$$

$$B=\begin{bmatrix} \frac{h}{C_1R_t} & 0 & \dots & 0 & 0 \\ 0 & \frac{h}{C_2R_t} & 0 & 0 & 0 \\ \vdots & & \ddots & & \vdots \\ 0 & 0 & 0 & \frac{h}{C_{N-1}R_t} & 0 \\ 0 & 0 & \dots & 0 & \frac{h}{C_NR_t} \end{bmatrix} \tag{2.90}$$

Since the Euler's method is expressed in discrete-time autonomous linear systems, it can be shown that the solution of capacitor voltage $\mathbf{v}_c^{k+1}$ at (k+1)$^{\text{th}}$ step can be expressed as a lumped system in terms of initial condition $\mathbf{v}_c^0$.

$$\mathbf{v}_c^{k+1}=\mathbf{A}^k\mathbf{A}^{k-1}\cdots\mathbf{A}^1\mathbf{A}^0\mathbf{v}_c^0+\left(\mathbf{A}^k\cdots\mathbf{A}^1\mathbf{A}^0+\mathbf{A}^{k-1}\cdots\mathbf{A}^1\mathbf{A}^0+\cdots+\mathbf{A}^1\mathbf{A}^0+\mathbf{A}^0\right)\mathbf{B}\mathbf{V}_{op} \tag{2.91}$$

It is difficult to analyze the stability of the lumped system in (2.91) which requires heavy computational effort to calculate the eigenvalues of the matrix $\mathbf{A}^k$ at each k$^{\text{th}}$ step [31][32][33]. However, the branch resistor R_n^k does not vary significantly and is similar to the neighborhood of multiple time steps. Therefore, it is essential to make sure that the initial matrix $\mathbf{A}^0$ is stable by keeping the eigenvalues of the matrix $\mathbf{A}^k$ to be inside the open unit disk of the complex plan $\mathbb{C}$, which yields,

$$|\lambda_n^0|<1, n=1,\dots,N \tag{2.92}$$

Hence, the stability of the function is mainly dependent on the ratio of the time step and the source resistance according to (2.87), (2.89) and (2.90). Therefore, the time step and the source resistor must be changed simultaneously to maintain a stable response. Fortunately, the source resistor does not have large impact on the overall performance. By Kirchhoff's Voltage Law, the source

resistor shares a small portion of the applying voltage which lowers the average electric field in the main body by a small portion equivalently speaking.

3. THERMAL EQUIVALENT CIRCUIT

3.1 Introduction

Since conductivity is not constant under DC operation, the electric field within a DC cable is more challenging to predict than within an AC cable [8][11][20][21][22][23]. Several empirical expressions for conductivity have been developed based upon measurements of temperature versus electric field [14][27]. In this chapter, a focus is to develop a thermal model of cable architectures so that the electric field within the cable can be predicted accurately.

3.2 Fundamentals of Analytical Thermal Expressions

3.2.1 General equations for model construction

Due to the electrical resistance, heat loss is generated by the current-carrying conductor. A thermal gradient is then established across the dielectric layer. A standard heat equation and Fourier's Law of heat conduction;

$$\rho C_p \frac{dT}{dt} = -\nabla \cdot \vec{\varphi} + p_H \tag{3.1}$$

$$\vec{\varphi} = -k\nabla T \tag{3.2}$$

$$\dot{Q} = \int_S \vec{\varphi} \cdot ds \tag{3.3}$$

can be applied to predict the thermal behavior within the dielectric of a co-axial cable [8][11][33]. In (3.1) - (3.3), ρ is the mass density of the dielectric in kg·m^{-3}; C_p is the specific heat of the dielectric in J·kg^{-1}·K^{-1}; T is the temperature in K; $\vec{\varphi}$ is the local heat flux density in W·m^{-2}; p_H is the heat generation per unit volume in W·m^{-3}; k is the thermal conductivity of the dielectric in W·m^{-1}·k^{-1}; and $\dot{Q}$ is the heat transfer through a given surface in W.

Combining equation (3.1) and (3.2), a general heat equation can be expressed as

$$\rho C_p \frac{dT}{dt} = \nabla \cdot (k \nabla T) + p_H \tag{3.4}$$

Although mass density, specific heat and thermal conductivity vary with temperature and electric conductivity (in the case of thermal conductivity), herein it is assumed that their respective changes are negligible. To further analyze the time differential term, both sides of equation (3.4) are divided by mass density and specific heat, which yields,

$$\frac{dT}{dt} = \alpha_T \nabla^2 T + \frac{1}{\rho C_p} p_H \tag{3.5}$$

$$\alpha_T = \frac{k}{\rho C_p} \tag{3.6}$$

, where $\nabla^2 T$ is the Laplacian of temperature and α_T is the thermal diffusivity, $m^2 \cdot s^{-1}$.

3.2.2 The analysis on the cable geometry

For the coaxial geometry shown in Fig.3.1, it is assumed that the thermal flux radiates outward from the inner conductor toward the outer ground cover. Therefore, it is convenient to express (3.5) in cylindrical coordinates:

$$\frac{dT}{dt} = \alpha_T \left(\frac{1}{r}\frac{\partial}{\partial r}\left(r\frac{\partial T}{\partial r}\right) + \frac{1}{r^2}\frac{\partial^2 T}{\partial \phi^2} + \frac{\partial^2 T}{\partial z^2}\right) + \frac{p_H}{\rho C_p} \tag{3.7}$$

It is assumed that the conductor is long, and therefore the heat is uniform in the axial direction. In addition, due to symmetry, it is assumed that the heat is independent of angular position. Therefore, (3.7) can be simplified to:

$$\frac{dT}{dt} = \alpha_T \left(\frac{1}{r}\frac{\partial}{\partial r}\left(r\frac{\partial T}{\partial r}\right)\right) + \frac{p_H}{\rho C_p} \tag{3.8}$$

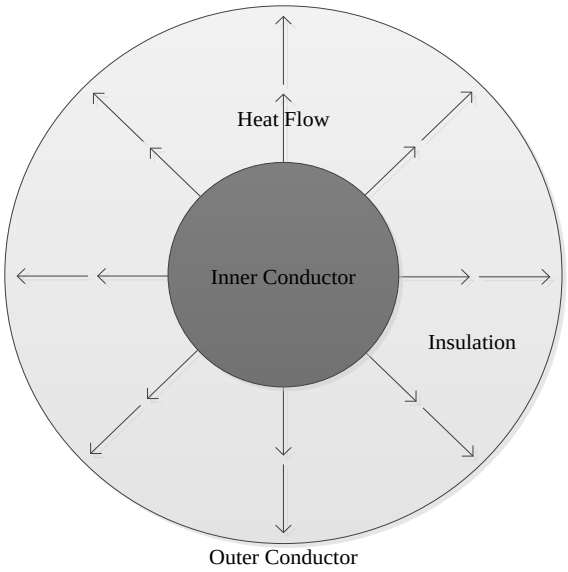

Fig.3.1 Heat flow illustration

3.2.3 Analytical steady-state thermal expressions

For DC excitation, the steady-state temperature within the dielectric can be acquired using Fourier's Law (3.2), yielding:

$$\vec{\varphi} = -k(\frac{\partial T}{\partial r}\hat{r} + \frac{1}{r}\frac{\partial T}{\partial \phi}\hat{\phi} + \frac{\partial T}{\partial r}\hat{z}) \tag{3.9}$$

Due to the symmetry of the cable layout, (3.9) in cylindrical coordinates can be further simplified:

$$\vec{\varphi} = -k(\frac{\partial T}{\partial r}\hat{r}) \tag{3.10}$$

The heat produced by the inner conductor crosses the boundary between the inner conductor and the dielectric and flows radially. Under the assumption of the negligible internal heat generation, p_H , due to leakage current within the dielectric layer compared to the conductor loss[8], the heat flux density can be expressed as,

$$\vec{\varphi} = -\frac{I_{op}^2 \cdot R_{cd}}{2\pi r} \tag{3.11}$$

and therefore, the heat conduction equation can be expressed,

$$k\frac{dT(r)}{dr} = -\frac{I_{op}^2 \cdot R_{cd}}{2\pi r}, r_{in} \le r \le r_{out} \tag{3.12}$$

, where, I_{op} and R_{cd} are, operating voltage, operating current and conductor resistance respectively. The temperature in (3.12) can be integrated from the outer radius r_{out} to an arbitrary radial position r, yielding

$$T(r) = \frac{I_{op}^2 R_{cd}}{2\pi k}\ln(\frac{r_{out}}{r}) + c_0 \tag{3.13}$$

where c_0 is constant coefficient, that can be evaluated at the outer boundary due to the accessibility of the outer surface temperature.

$$T(r_{out}) = T_{out} \tag{3.14}$$

Hence, the temperature within the dielectric of a co-axial cable can be expressed analytically as,

$$T(r) = \frac{I_{op}^2 R_{cd}}{2\pi k}\ln(\frac{r_{out}}{r}) + T_{out} \tag{3.15}$$

The steady-state temperature drop across the dielectric can be acquired by subtracting the temperatures between the inner r_{in} and the outer boundary r_{out}, which yields:

$$T_{in} - T_{out} = \frac{I_{op}^2 R_{cd}}{2\pi k}\ln(\frac{r_{out}}{r_{in}}) \tag{3.16}$$

This equation illustrates the impact that resistive loss in the conductor has on the temperature within range within the dielectric.

3.3 Thermal Equivalent Circuit

3.3.1 Thermal equivalent circuit model

To understand the transient behavior of the temperature, a thermal equivalent circuit model based on (3.8) with time differential term is derived [34].In Fig.3.2, a cross-sectional area of a coaxial cable is shown with the area of interest, Ω, covered from inner to outer radius, $r_{\Omega i}$ to $r_{\Omega o}$, and an angular region of θ_{Ω}. The coaxial cable extends both into and out of the page, in the direction of z axis.

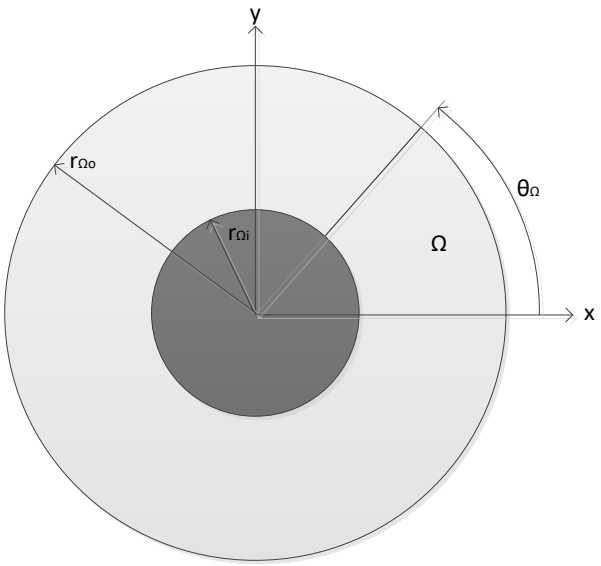

Fig.3.2 Cylindrical region of interest

As shown previously, the steady state solution within the dielectric can be expressed in a form:

$$T(r) = c_{lr} \ln(r) + c_0 \tag{3.17}$$

, where c_{lr} and c_0 are the constant coefficients.

$$c_{lr} = -\frac{I_{op}^2 R_{cd}}{2\pi k} \tag{3.18}$$

$$c_0 = \frac{I_{op}^2 R_{cd}}{2\pi k} \ln(r_{out}) + T_{out} \tag{3.19}$$

For the region of interest, the spatial average of temperature can be found as,

$$\langle T_\Omega \rangle = \frac{\iiint_{V_\Omega} T_\Omega dV}{\iiint_{V_\Omega} dV} \tag{3.20}$$

$$\langle T_\Omega \rangle = \frac{1}{V_\Omega} \int_0^{l_d} \int_0^{\theta_\Omega} \int_{r_{\Omega i}}^{r_{\Omega 0}} (T(r)) r dr d\theta dz \tag{3.21}$$

$$V_\Omega = \frac{\theta_\Omega l_d (r_{\Omega o}^2 - r_{\Omega i}^2)}{2} \tag{3.22}$$

The spatial average of temperature can be readily obtained using (3.21):

$$\langle T_\Omega \rangle = c_{lr} \left(\frac{r_{\Omega o}^2 \ln(r_{\Omega o}) - r_{\Omega i}^2 \ln(r_{\Omega i})}{r_{\Omega o}^2 - r_{\Omega i}^2} - \frac{1}{2} \right) + c_0 \tag{3.23}$$

From (3.17), the temperatures at the inner and outer boundaries can be expressed:

$$T_{\Omega ir} = T_\Omega(r_{\Omega i}) = c_{lr} \ln(r_{\Omega i}) + c_0 \tag{3.24}$$

$$T_{\Omega or} = T_\Omega(r_{\Omega o}) = c_{lr} \ln(r_{\Omega o}) + c_0 \tag{3.25}$$

Plugging the overall spatial average of temperature shown in (3.23) into the boundary temperature shown of (3.24) and (3.25):

$$T_{\Omega ir} = \langle T_\Omega \rangle - c_{lr} \left(\frac{r_{\Omega o}^2}{r_{\Omega o}^2 - r_{\Omega i}^2} \ln\left(\frac{r_{\Omega o}}{r_{\Omega i}}\right) - \frac{1}{2} \right) \tag{3.26}$$

$$T_{\Omega or} = \langle T_\Omega \rangle - c_{lr} \left(\frac{r_{\Omega i}^2}{r_{\Omega o}^2 - r_{\Omega i}^2} \ln\left(\frac{r_{\Omega o}}{r_{\Omega i}}\right) - \frac{1}{2} \right) \tag{3.27}$$

Applying boundary condition via Fourier's Law stated in equation (3.2) to the heat transfer over the boundary surface using equation (3.3), the heat transfer rate can be obtained.

$$\dot{Q}_\Omega = -k\theta_\Omega l_d c_{lr} \tag{3.28}$$

Since the radial component is cancelled during integration in (3.28), the heat transfer rate at the boundaries can be obtained.

$$\dot{Q}_{\Omega ir} = -k\theta_{\Omega} l_d c_{lr} \tag{3.29}$$

$$\dot{Q}_{\Omega or} = -k\theta_{\Omega} l_d c_{lr} \tag{3.30}$$

Substituting the coefficient c_{lr} back into the boundary spatial average of temperature in equation (3.26) and (3.27) respectively, boundary temperature expressions can be updated with the equivalent thermal resistances.

$$T_{\Omega ir} = \langle T_{\Omega} \rangle + R_{\Omega ir} \dot{Q}_{\Omega ir} \tag{3.31}$$

$$T_{\Omega or} = \langle T_{\Omega} \rangle - R_{\Omega or} \dot{Q}_{\Omega or} \tag{3.32}$$

The thermal resistances $R_{\Omega ir}$ and $R_{\Omega or}$ in the updated temperature equation (3.31) and (3.32) are given by,

$$R_{\Omega ir} = \frac{1}{k\theta_{\Omega} l_d} \left(\frac{r_{\Omega o}^2}{r_{\Omega o}^2 - r_{\Omega i}^2} \ln\left(\frac{r_{\Omega o}}{r_{\Omega i}} \right) - \frac{1}{2} \right) \tag{3.33}$$

$$R_{\Omega or} = \frac{1}{k\theta_{\Omega} l_d} \left(\frac{1}{2} - \frac{r_{\Omega i}^2}{r_{\Omega o}^2 - r_{\Omega i}^2} \ln\left(\frac{r_{\Omega o}}{r_{\Omega i}} \right) \right) \tag{3.34}$$

The transient performance of the equivalent circuit can be derived by integrating the heat equation (3.1) over the volume of interest.

$$\int_0^{l_d} \int_0^{\theta_{\Omega}} \int_{r_{\Omega i}}^{r_{\Omega o}} \left(\frac{dT}{dt} \right) r dr d\theta dz = -\frac{1}{\rho C_p} \int_{r_{\Omega i}}^{r_{\Omega o}} \int_0^{l_d} \int_0^{\theta_{\Omega}} \left(\nabla \cdot \vec{\varphi} \right) r d\theta dz dr + \frac{1}{\rho C_p} \int_0^{l_d} \int_0^{\theta_{\Omega}} \int_{r_{\Omega i}}^{r_{\Omega o}} \left(p_H \right) r dr d\theta dz \tag{3.35}$$

The time derivative term can be expressed by applying the definition equation in (3.20) to (3.22).

$$\int_0^{l_d}\int_0^{\theta_\Omega}\int_{r_{\Omega i}}^{r_{\Omega o}}\left(\frac{dT}{dt}\right)rdrd\theta dz = V_\Omega \frac{d\left\langle T_\Omega \right\rangle}{dt} = V_\Omega \left\langle \frac{dT}{dt} \right\rangle \tag{3.36}$$

The heat transfer rate can be expressed in the cylindrical coordinates, yielding:

$$\int_{r_{\Omega i}}^{r_{\Omega o}}\int_0^{l_d}\int_0^{\theta_\Omega}\left(\nabla\cdot\vec{\varphi}\right)rd\theta dzdr = \int_{r_{\Omega i}}^{r_{\Omega o}}\int_0^{l_d}\int_0^{\theta_\Omega}\left(\frac{1}{r}\frac{\partial\left(r\varphi_r\right)}{\partial r}+\frac{1}{r}\frac{\partial\varphi_\phi}{\partial\phi}+\frac{\partial\varphi_z}{\partial z}\right)rd\theta dzdr \tag{3.37}$$

It is noted that heat transfer rate only contains radial component as discussed above. The (3.37) can be rearranged, yielding:

$$\int_{r_{\Omega i}}^{r_{\Omega o}}\int_0^{l_d}\int_0^{\theta_\Omega}\left(\nabla\cdot\vec{\varphi}\right)rd\theta dzdr = \int_{r_{\Omega i}}^{r_{\Omega o}}\int_0^{l_d}\int_0^{\theta_\Omega}\left(\frac{\partial\left(r\varphi_r\right)}{\partial r}\right)d\theta dzdr = 2\pi l_d\int_{r_{\Omega i}}^{r_{\Omega o}}\left(\frac{\partial\left(r\varphi_r\right)}{\partial r}\right)dr \tag{3.38}$$

Hence, the integral can be expressed as,

$$\int_{r_{\Omega i}}^{r_{\Omega o}}\int_0^{l_d}\int_0^{\theta_\Omega}\left(\nabla\cdot\vec{\varphi}\right)rd\theta dzdr = 2\pi l_d\left(r_{\Omega o}\varphi_{r_{\Omega o}} - r_{\Omega i}\varphi_{r_{\Omega i}}\right) \tag{3.39}$$

The heat transfer through the inner and the outer boundaries can be expressed with (3.3) in the cylindrical coordinates.

$$\dot{Q} = \int_0^{l_d}\int_0^{2\pi}\left(\varphi_r\hat{r}+\varphi_\phi\hat{\phi}+\varphi_z\hat{z}\right)\cdot r\hat{r}d\theta dz \tag{3.40}$$

Similar to the previous discussion, only radial component is taken into consideration, yielding:

$$\dot{Q} = \int_0^{l_d}\int_0^{2\pi}\left(\varphi_r\right)rd\theta dz = 2\pi l_d\varphi_r r \tag{3.41}$$

Combining (3.39) and (3.41), the final form of the integral can be expressed in terms of the heat transfer over the surface area of two boundaries.

$$\int_{r_{\Omega i}}^{r_{\Omega o}}\int_0^{l_d}\int_0^{\theta_\Omega}\left(\nabla\cdot\vec{\varphi}\right)rd\theta dzdr = -\dot{Q}_{\Omega ir}+\dot{Q}_{\Omega or} \tag{3.42}$$

The internal heat generation is negligible due to low leakage as discussed earlier. Hence, the (3.35) yields,

$$\frac{d\langle T_\Omega \rangle}{dt} = \left\langle \frac{dT}{dt} \right\rangle = \frac{1}{\rho C_p V_\Omega}\left(\dot{Q}_{\Omega ir} - \dot{Q}_{\Omega or} \right) \tag{3.43}$$

Hence, the difference in heat flux rates at two boundaries can be treated as the equivalent current into the thermal equivalent capacitor. Thus the equivalent thermal capacitor can be expressed as,

$$C_\Omega = \rho C_p V_\Omega = \frac{1}{2}\rho C_p l_d \theta_\Omega (r_{\Omega o}^2 - r_{\Omega i}^2) \tag{3.44}$$

Herein, an equivalent thermal circuit can be constructed in Fig.3.3 with the equivalent thermal components labeled. Within the circuit, temperature, heat transfer, and internal heat generation are represented using voltage, current and current source respectively.

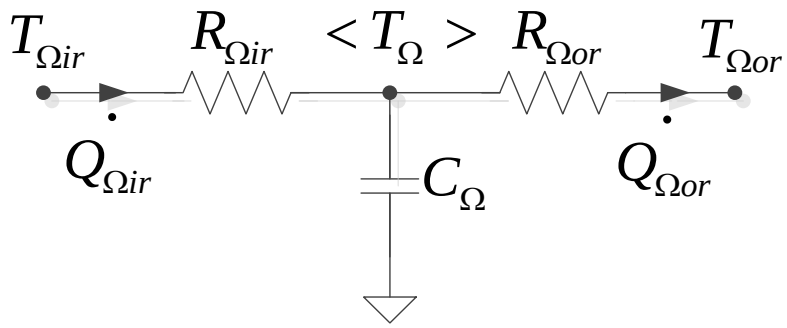

Fig.3.3 Thermal equivalent circuit of cylindrical region

3.3.2 Thermal equivalent circuit analysis with layer discretization

The thermal equivalent circuit can be utilized to analyze the transient thermal performance of a dielectric layer. A detailed temperature profile is required to study the electrical performance described in Chapter 2.

To do so, the dielectric layer is discretized into N concentric ring tubes as illustrated in Fig.3.4. Herein, each concentric ring tube can be considered as a volume of interest with unit depth of l_d. The equivalent thermal circuit derived in chapter 3.3.1 depicted in Fig.3.3 can be applied to

each concentric ring tube to describe the temperature as shown in Fig.3.5. Thus, the spatial average of temperature, $<T_\Omega>$, is used to represent the average temperature of each concentric ring tube. The angle of interest, $\theta_\Omega=2\pi$ and starting and ending radius, $r_{\Omega i}$ and $r_{\Omega o}$, $r_{sp,n}$ and $r_{ep,n}$ are substituted into the thermal resistance and capacitance derived in (3.33), (3.34) and (3.44).

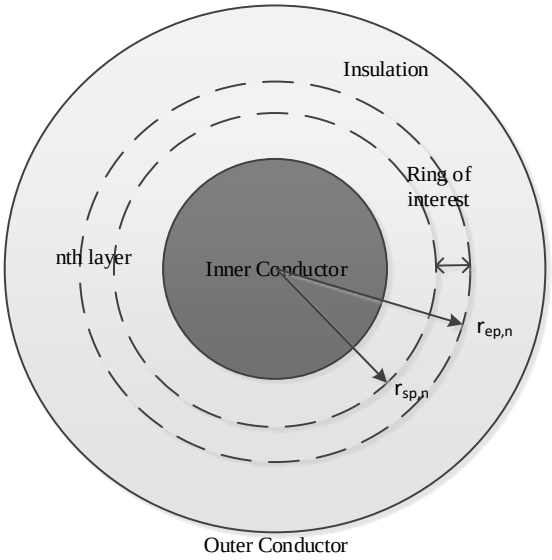

Fig.3.4 Concentric ring tube of interest

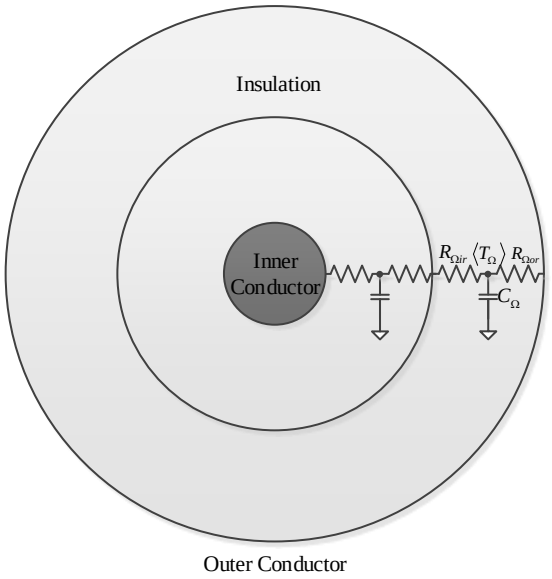

Fig.3.5 The equivalent thermal circuit of ring tube

A distributed system of the thermal profile can be extracted and constructed using the thermal equivalent circuit as shown in Fig.3.6. Hence, the conductor heat loss is the equivalent current source shown to the left of the distributed system. The voltage of the equivalent capacitor represents the average temperature of each ring tube segment. A constant voltage source, T_{amb}, is added to the right end of the circuit to represent the ambient temperature. The thermal equivalent circuit is implemented in software to simulate the development of thermal distribution.

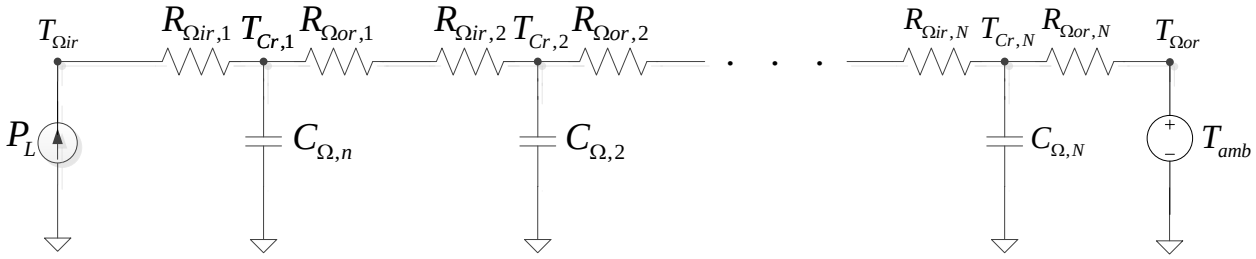

Fig.3.6 Distributed equivalent thermal circuit

3.3.3 Software implementation

The state model of the system in Fig.3.6 is expressed by first starting with each tube capacitor current

$$C_{\Omega,n}\left(\frac{dT}{dt}\right)_{Cr,n} = I_{C,n} \tag{3.45}$$

where $I_{C,n}$ stands for the current flowing into the capacitor. To establish the thermal transient model, a nodal analysis is constructed with Kirchhoff's Current Law with the state variable $T_{Cr,n}$. In Fig.3.6, the current at each center node $T_{cr,n}$ can be expressed. It is noted that n ≠ 1, N.

$$\frac{T_{cr,n} - T_{cr,n-1}}{R_{\Omega or,n-1} + R_{\Omega ir,n}} + \frac{T_{cr,n} - T_{cr,n+1}}{R_{\Omega ir,n+1} + R_{\Omega or,n}} + I_{C,n} = 0 \tag{3.46}$$

At inner and outer boundary where n = 1, N, the current can be expressed.

$$\frac{T_{cr,1}-T_{\Omega ir}}{R_{\Omega ir,1}}+\frac{T_{cr,1}-T_{cr,2}}{R_{\Omega ir,2}+R_{\Omega or,1}}+I_{C,1}=0 \tag{3.47}$$

$$\frac{T_{cr,N}-T_{cr,N-1}}{R_{\Omega or,N-1}+R_{\Omega ir,N}}+\frac{T_{cr,N}-T_{\Omega or}}{R_{\Omega or,N}}+I_{C,N}=0 \tag{3.48}$$

In most cases, the inner boundary, $T_{\Omega ir}$, is an unknown. The heat loss P_L is introduced. The outer boundary, $T_{\Omega or}$, is the same as ambient temperature T_{amb}.

$$-P_L+\frac{T_{cr,1}-T_{cr,2}}{R_{\Omega ir,2}+R_{\Omega or,1}}+I_{C,1}=0 \tag{3.49}$$

$$\frac{T_{cr,N}-T_{cr,N-1}}{R_{\Omega or,N-1}+R_{\Omega ir,N}}+\frac{T_{cr,N}-T_{amb}}{R_{\Omega or,N}}+I_{C,N}=0 \tag{3.50}$$

In this research, the state model is solved using a forward Euler integration algorithm,

$$T_{Cr,n}^{k+1}=T_{Cr,n}^{k}+h\left(\frac{dT}{dt}\right)_{Cr,n}^{k} \tag{3.51}$$

where here, the superscript k is used to denote the index of time and h stands for time step. The selection of a Forward Euler algorithm is considered in the next Section. A block diagram to realize the circuit development has been provided in Fig.3.7. After thermal equivalent circuit initialization, a matrix of the thermal resistor network is constructed to solve the capacitor currents via (3.46) to (3.50). Subsequently, the capacitor voltages are updated using forward Euler integration algorithm using (3.51). Similar to the electric equivalent circuit, the difference of the thermal capacitor voltage between successive time steps is used to determine a stopping time.

$$\left|T_{Cr,n}^{k+1}-T_{Cr,n}^{k}\right|<e_{\max,step} \tag{3.52}$$

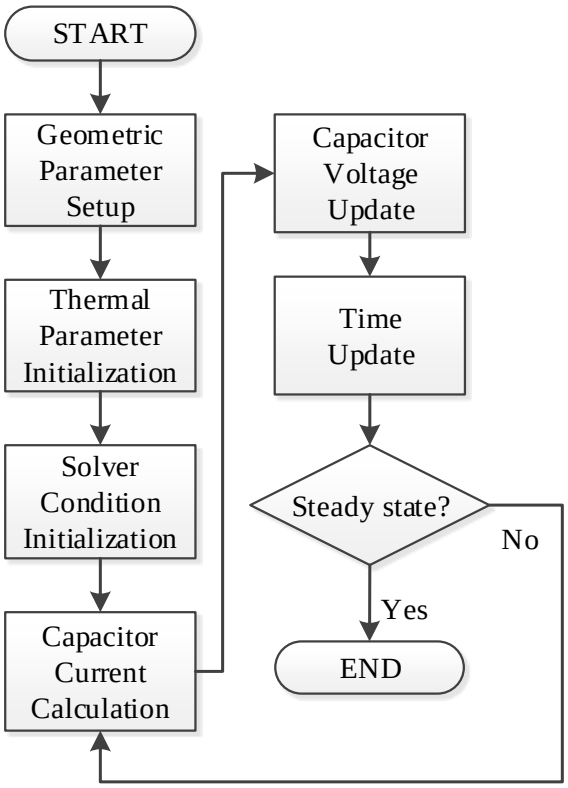

Fig.3.7 Block diagram for thermal circuit model

To validate the approach, the circuit is tested with the similar test stated in Chapter 2 with the parameters given in Table 2.1 [8].

The circuit is tested with an operating current of 1600 A with environment (soil) temperature of 292.15 K, 19 ^{o}C equivalently. The outer sheath temperature is 314.27 K, 41.12 ^{o}C equivalently. The conductor heat loss per unit depth is 44.4928 W with Aluminum. The transient results of the overall geometry and the inner boundary are shown in Fig.3.8 & Fig.3.9 respectively. It is noted that temperature rises much faster near the inner boundary and during the initial transient. With a thin layer of the dielectric in presence, it takes around 100 minutes to reach steady state. The steady-state results are compared with analytical steady-state expression using power loss derived from equation (3.15) shown in Fig.3.10. Similar steady-state results are compared with

operating currents of 1600 A to 2000 A shown in Fig.3.11 where the different sheath temperatures are due to the surrounding soil layer.

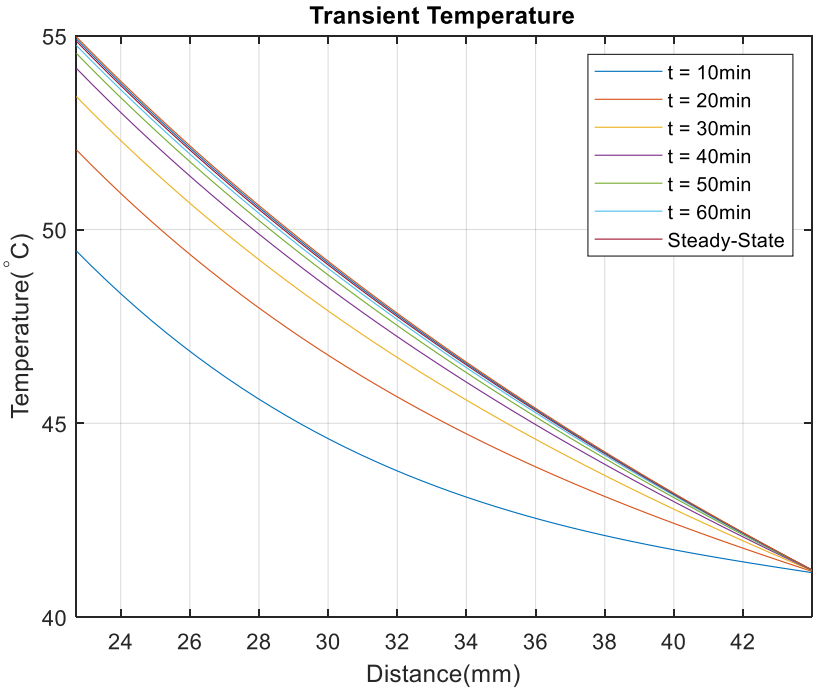

Fig.3.8 Real-time temperature development

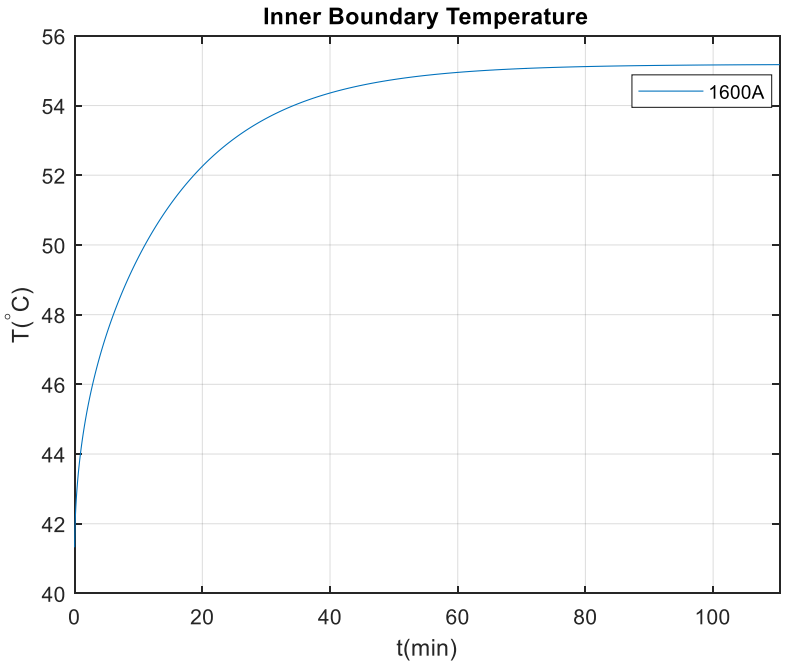

Fig.3.9 Real-time temperature at inner boundary

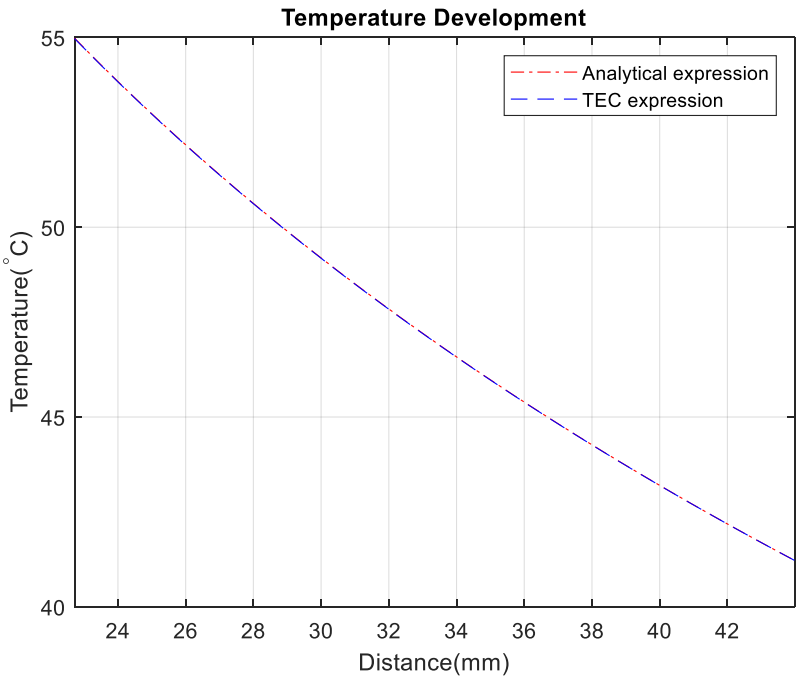

Fig.3.10 Steady-state comparison

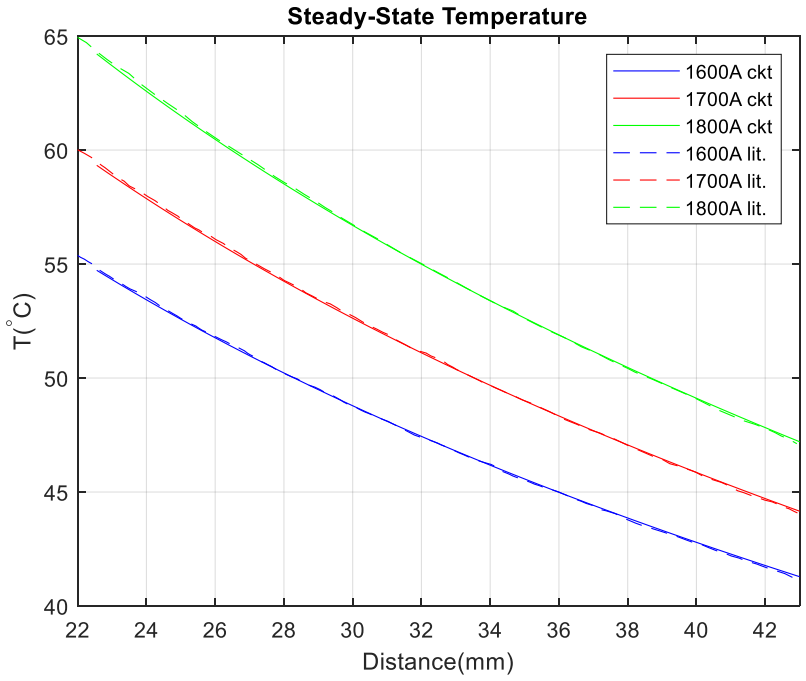

Fig.3.11 Steady-state comparison with different operating currents

3.3.4 Integration solver selections

3.3.4.1 Integration approaches for state update

Two approaches to solve the state model of (3.45) are provided for comparison and evaluation for error and efficiency. The first approach utilizes a Forward Euler algorithm:

$$T_{Cr,n}^{k+1} = T_{Cr,n}^{k} + h\left(\frac{dT}{dt}\right)_{Cr,n}^{k} \tag{3.53}$$

The second approach utilizes a Fourth-Order Runge Kutta algorithm, which has the form as below.

$$f(T_{Cr,n}^{k}, t^{k}) = \left(\frac{dT}{dt}\right)_{Cr,n}^{k} = \left(-\frac{1}{C_{\Omega,n}\left(R_{\Omega or,n-1} + R_{\Omega ir,n}\right)} - \frac{1}{C_{\Omega,n}\left(R_{\Omega ir,n+1} + R_{\Omega or,n}\right)}\right) T_{Cr,n}^{k} + \frac{1}{C_{\Omega,n}\left(R_{\Omega or,n-1} + R_{\Omega ir,n}\right)} T_{Cr,n-1}^{k} + \frac{1}{C_{\Omega,n}\left(R_{\Omega ir,n+1} + R_{\Omega or,n}\right)} T_{Cr,n+1}^{k} \tag{3.54}$$

$$f(T_{Cr,1}^{k}, t^{k}) = \left(\frac{dT}{dt}\right)_{Cr,1}^{k} = \left(-\frac{1}{C_{\Omega,1}\left(R_{\Omega ir,2} + R_{\Omega or,1}\right)}\right) T_{Cr,1}^{k} + \frac{1}{C_{\Omega,1}\left(R_{\Omega ir,2} + R_{\Omega or,1}\right)} T_{Cr,2}^{k} + \frac{1}{C_{\Omega,1}} P_{L} \tag{3.55}$$

$$f(T_{Cr,N}^{k}, t^{k}) = \left(\frac{dT}{dt}\right)_{Cr,N}^{k} = \left(-\frac{1}{C_{\Omega,N}\left(R_{\Omega or,N-1} + R_{\Omega ir,N}\right)} - \frac{1}{C_{\Omega,N} R_{\Omega or,N}}\right) T_{Cr,N}^{k} + \frac{1}{C_{\Omega,N}\left(R_{\Omega or,N-1} + R_{\Omega ir,N}\right)} T_{Cr,N-1}^{k} + \frac{1}{C_{\Omega,N} R_{\Omega or,N}} T_{amb} \tag{3.56}$$

The state update equation can be shown as,

$$T_{Cr,n}^{k+1} = T_{Cr,n}^{k} + \frac{1}{6}\left(F_{1,n}^{k} + 2F_{2,n}^{k} + 2F_{3,n}^{k} + F_{4,n}^{k}\right) \tag{3.57}$$

where the four higher order terms are shown as,

$$\begin{cases} F_{1,n}^{k} = hf\left(T_{Cr,n}^{k}, t^{k}\right) \\ F_{2,n}^{k} = hf\left(T_{Cr,n}^{k} + \frac{1}{2}F_{1,n}^{k}, t^{k} + \frac{1}{2}h\right) \\ F_{3,n}^{k} = hf\left(T_{Cr,n}^{k} + \frac{1}{2}F_{2,n}^{k}, t^{k} + \frac{1}{2}h\right) \\ F_{4,n}^{k} = hf\left(T_{Cr,n}^{k} + F_{3,n}^{k}, t^{k} + h\right) \end{cases} \tag{3.58}$$

3.3.4.2 Solver implementation and comparisons

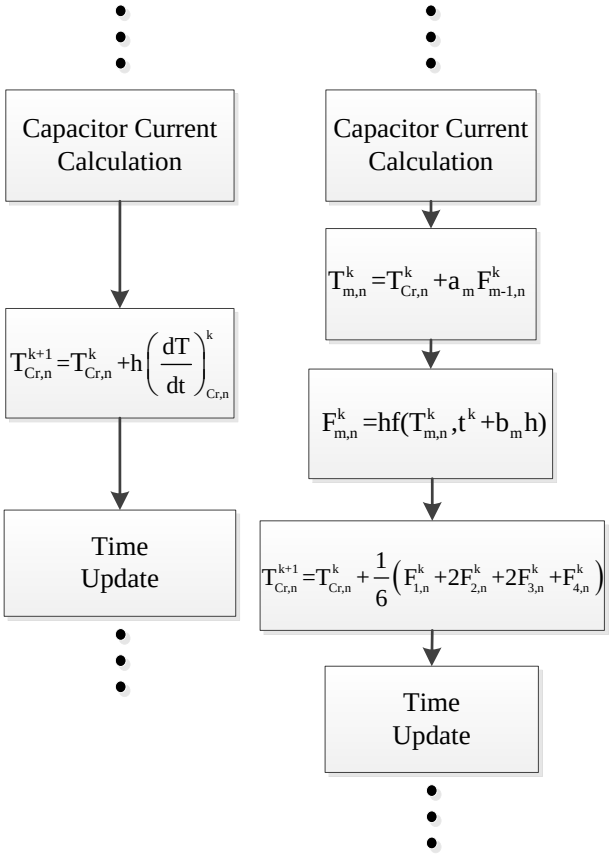

Fig.3.12 Detailed solver block diagram for thermal circuit model

Two approaches to the integration are shown in Fig.3.12 with the Forward Euler's Method and the Fourth-Order Runge-Kutta Method on the left and right respectively. The error analysis

has been examined between two approaches with Runge-Kutta method as the basis. The maximum absolute relative error equation is provided.

$$\epsilon_{abs,\max}^{k} = \max\left(\left|\frac{T_{Euler}^{k} - T_{RK4}^{k}}{T_{RK4}^{k}}\right|\right)\times 100\% \tag{3.59}$$

where $\epsilon_{abs,\max}^{k}$, T_{Euler}^{k} and T_{RK4}^{k} represents the maximum absolute relative error, the temperature from the Forward Euler's Method and the Fourth-Order Runge-Kutta Method respectively. The system is simulated with time step of 0.002s and total time of 2.72s and the parameters from Reddy's experiment[8]. Hence, the maximum error and relative computation time are provided in Table 3.1.

Table 3.1 The Comparison of Different Approaches

	Error Comparison	η
Runge-Kutta	N.A	2.13%
Forward Euler	$6.5\text{x}10^{-4}$%	1.03%

It is noted that it reduces the computational effort using Forward Euler's Method while no significant deviation from the solution from the Fourth-Order Runge-Kutta Method. To implement within an optimization algorithm, the Forward Euler's Method is chosen for temperature simulation for time efficiency while Fourth-Order Runge-Kutta Method for detailed solutions in the case study.

3.3.4.3 Stability analysis of state update

By substituting (3.45), (3.46), (3.49) and (3.50) into (3.51), the update function at each segment can be rearranged and expressed.

$$T_{Cr,n}^{k+1}=\left(1-\frac{h}{C_{\Omega,n}\left(R_{\Omega or,n-1}+R_{\Omega ir,n}\right)}-\frac{h}{C_{\Omega,n}\left(R_{\Omega ir,n+1}+R_{\Omega or,n}\right)}\right)T_{Cr,n}^{k}+\frac{h}{C_{\Omega,n}\left(R_{\Omega or,n-1}+R_{\Omega ir,n}\right)}T_{Cr,n-1}^{k}+\frac{h}{C_{\Omega,n}\left(R_{\Omega ir,n+1}+R_{\Omega or,n}\right)}T_{Cr,n+1}^{k} \tag{3.60}$$

$$T_{Cr,1}^{k+1}=\left(1-\frac{h}{C_{\Omega,1}\left(R_{\Omega ir,2}+R_{\Omega or,1}\right)}\right)T_{Cr,1}^{k}+\frac{h}{C_{\Omega,1}\left(R_{\Omega ir,2}+R_{\Omega or,1}\right)}T_{Cr,2}^{k}+\frac{h}{C_{\Omega,1}}P_{L} \tag{3.61}$$

$$T_{Cr,N}^{k+1}=\left(1-\frac{h}{C_{\Omega,N}\left(R_{\Omega or,N-1}+R_{\Omega ir,N}\right)}-\frac{h}{C_{\Omega,N}R_{\Omega or,N}}\right)T_{Cr,N}^{k}+\frac{h}{C_{\Omega,N}\left(R_{\Omega or,N-1}+R_{\Omega ir,N}\right)}T_{Cr,N-1}^{k}+\frac{h}{C_{\Omega,N}R_{\Omega or,N}}T_{amb} \tag{3.62}$$

The update equation set can be summarized into a matrix form based upon (3.60) to (3.62).

$$\mathbf{T}_{Cr}^{k+1}=\mathbf{A}\mathbf{T}_{Cr}^{k}+\mathbf{B}\dot{\mathbf{Q}}_{ext} \tag{3.63}$$

where capacitor voltages $\mathbf{T}_{Cr}^{k}$ and external sources $\dot{\mathbf{Q}}_{ext}$ are in the column vector form while $\mathbf{A}$ and $\mathbf{B}$ are the coefficient matrix for the general solution and the particular solution corresponding to the external heat input and internal heat generation respectively, which yields,

$$\dot{\mathbf{Q}}_{ext}=\begin{bmatrix}P_{L} & 0 & \cdots & 0 & \dfrac{T_{amb}}{R_{\Omega or,N}}\end{bmatrix}^{T} \tag{3.64}$$

$$\mathbf{A}=\begin{bmatrix} 1-\dfrac{h}{C_{\Omega,1}\left(R_{\Omega ir,2}+R_{\Omega or,1}\right)} & \dfrac{h}{C_{\Omega,1}\left(R_{\Omega ir,2}+R_{\Omega or,1}\right)} & 0 & \cdots \\ \dfrac{h}{C_{\Omega,2}\left(R_{\Omega or,1}+R_{\Omega ir,2}\right)} & A_{2,2} & \dfrac{h}{C_{\Omega,2}\left(R_{\Omega ir,3}+R_{\Omega or,2}\right)} & 0 \\ \vdots & & & \ddots \\ 0 & 0 & 0 & 0 \\ 0 & 0 & 0 & \cdots \end{bmatrix}$$

$$\begin{bmatrix} \cdots & 0 & 0 & 0 \\ 0 & 0 & 0 & 0 \\ \ddots & & & \vdots \\ 0 & \dfrac{h}{C_{\Omega,N-1}\left(R_{\Omega or,N-2}+R_{\Omega ir,N-1}\right)} & A_{N-1,N-1} & \dfrac{h}{C_{\Omega,N-1}\left(R_{\Omega ir,N}+R_{\Omega or,N-1}\right)} \\ \cdots & 0 & \dfrac{h}{C_{\Omega,N}\left(R_{\Omega or,N-1}+R_{\Omega ir,N}\right)} & 1-\dfrac{h}{C_{\Omega,N}\left(R_{\Omega or,N-1}+R_{\Omega ir,N}\right)}-\dfrac{h}{C_{\Omega,N}R_{\Omega or,N}} \end{bmatrix} \tag{3.65}$$

$$A_{2,2}=1-\frac{h}{C_{\Omega,2}\left(R_{\Omega or,1}+R_{\Omega ir,2}\right)}-\frac{h}{C_{\Omega,2}\left(R_{\Omega ir,3}+R_{\Omega or,2}\right)} \tag{3.66}$$

$$A_{N-1,N-1}=1-\frac{h}{C_{\Omega,N-1}\left(R_{\Omega or,N-2}+R_{\Omega ir,N-1}\right)}-\frac{h}{C_{\Omega,N-1}\left(R_{\Omega ir,N}+R_{\Omega or,N-1}\right)} \tag{3.67}$$

$$\mathbf{B}=\begin{bmatrix} \dfrac{h}{C_{\Omega,1}} & 0 & \cdots & 0 & 0 \\ 0 & 0 & 0 & 0 & 0 \\ \vdots & & \ddots & & \vdots \\ 0 & 0 & 0 & 0 & 0 \\ 0 & 0 & \cdots & 0 & \dfrac{h}{C_{\Omega,N}} \end{bmatrix} \tag{3.68}$$

Based upon the discrete-time system characteristic equation, it is essential to ensure the eigenvalues of the matrix $\mathbf{A}$ in (3.63) to be inside the open unit disk of the complex plan $\mathbb{C}$, which yields,

$$|\lambda_n|<1, n=1,\ldots,N \tag{3.69}$$

Within an optimization, all of the geometric details are established, and therefore one can compute the eigenvalues analytically, after which the time step is selected to ensure the simulation remains stable.

4. MULTICONDUCTOR CABLE DESIGN

4.1 Introduction

The analysis techniques developed in Chapters 2 and 3 have been applied to the single conductor coaxial cable. In this chapter, the approach is extended to a multi-conductor cable shown in Fig.4.1. The formulation of the model is achieved using judicious application of the Method of Images (MOI). Validation of the model is performed through comparison of results obtained using finite element analysis.

The dimensions used for analysis of the multi-conductor cable are R_c, R_I, R_O, Di_{in}, and Di_{out} which are the location of the center of the inner +/- conductor to the center O of the cable, the radius of the inner +/- conductor and the outer (shield) conductor, and the thickness of the inner dielectric and outer dielectric, respectively.

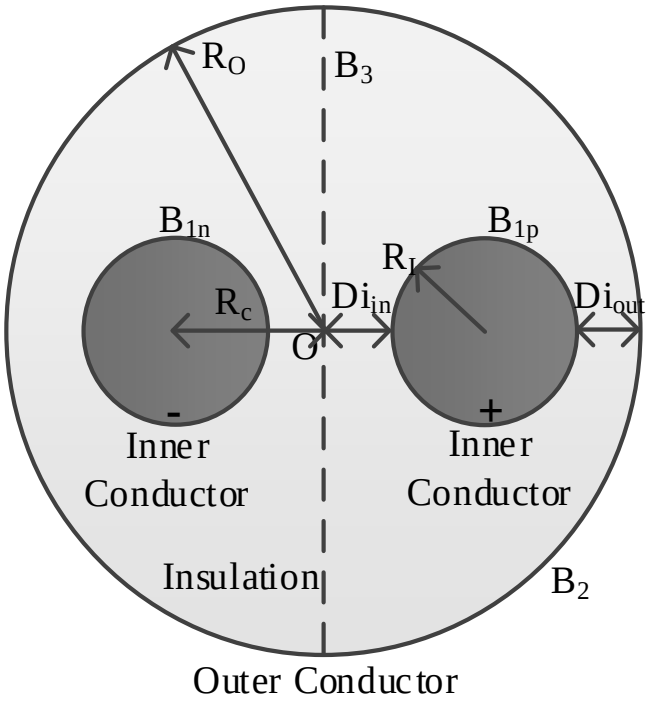

Fig.4.1 Multiconductor cable

4.2 Method of Images

The basis of the model considered are electric and thermal flux tubes that are assembled to model the flux paths within the dielectric [29][34][53]. In the case of a single conductor geometry, establishing the flux tubes is relatively straightforward, since both the thermal and the electric flux follow a radial path that can be modeled using cylindrical tubes.

In contrast, in a multi-conductor cable, the thermal and electric flux paths have both radial and angular direction as shown in Fig.4.2. The electric flux distribution was computed using the commercial FEA tool COMSOL. As a result, deriving the tubes is a challenge. To address, it is first assumed that the changes in conductivity do not alter the direction of the thermal and electric flux lines. This is validated using the FEA results shown in Fig.4.2 wherein the flux paths with uniform conductivity (blue) and a nonuniform conductivity (in red) are shown. It is noted that electric flux lines share the similar paths with some minor deviations. As a result, flux tube geometries are established by solving the Laplacian-based distribution of the fields. Specifically, the respective Laplacian for thermal and electric potential can be expressed as:

$$k\nabla \cdot \nabla T = 0 \tag{4.1}$$

$$\sigma\nabla \cdot \nabla V = 0 \tag{4.2}$$

The solution is accomplished using the Method of Images (MoI). Specifically, the electric and thermal fields generated by a line charge also obey the Laplacian distributions obtained by solving (4.2).

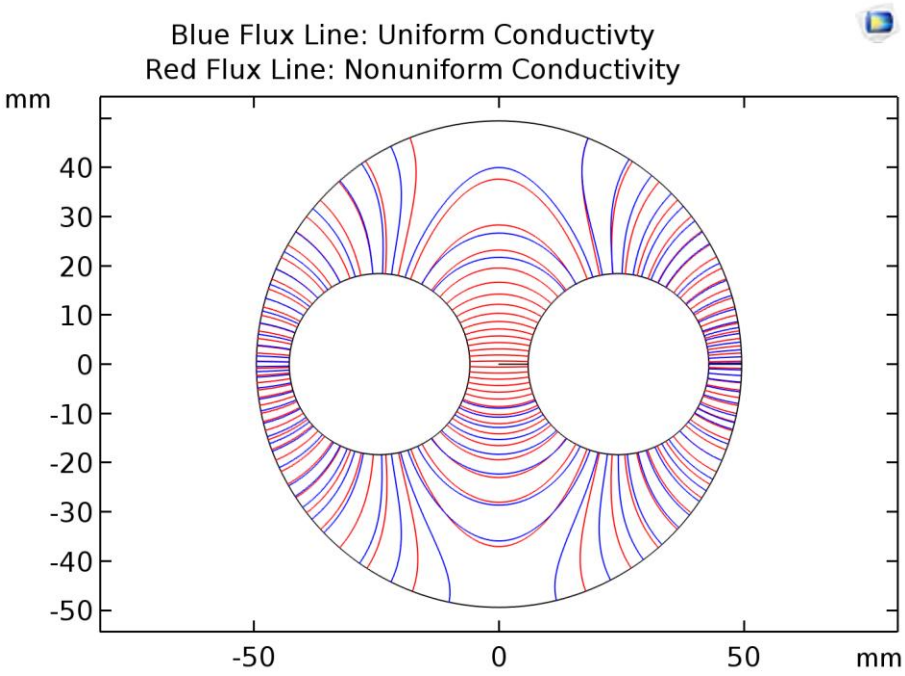

Fig.4.2 Electric flux distribution under uniform/nonlinear conductivity

To solve for the field distribution using line charges, it is assumed that the flux lines are perpendicular to the surface interface between the inner conductors and the dielectric, the dielectric and the outer conducting shield, and in the case of the electric field, at the center line between conductors. These perpendicular interfaces are represented by B_{1p} and B_{1n}, B_2, and B_3, respectively in Fig.4.1.

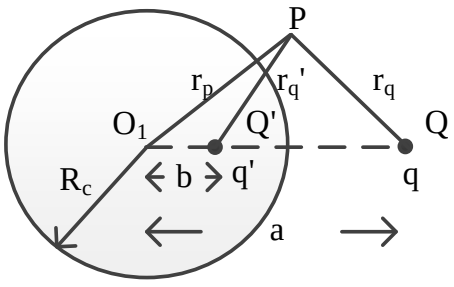

Fig.4.3 Method of images for a cylindrical equal potential surface

In general, the MoI can be used to solve for fields that have cylindrical and linear equipotential surfaces [46][47][48][49][50][51][52]. To provide a background on its application, a representative cylindrical equipotential surface is shown in Fig.4.3. Therein O_1 and R_c are the center and the radius of the cylinder respectively. A line charge q and an arbitrary point P are located at r=a and r=r_p away from the center O_1, respectively. To solve for the fields outside the conducting cylinder, the equipotential surface is removed and replaced with an image line charge q' located at point b. To establish the location of b, the potential distribution due to a line charge *q* is first utilized. Specifically,

$$V(r)-V(r_0)=-\int_{r_0}^{r}\frac{q}{2\pi\varepsilon\gamma}d\gamma=\frac{q}{2\pi\varepsilon}\ln(\frac{r_0}{r}) \tag{4.3}$$

where the *r* is an arbitrary location and the r_0 is a reference point. As a result, the potential distribution outside the equipotential surface at an arbitrary point P due to q and q' can then be expressed by adding the two contributions using (4.3) which yields,

$$V_P=\frac{q}{2\pi\varepsilon}\ln(\frac{r_0}{r_q})+\frac{q'}{2\pi\varepsilon}\ln(\frac{r_0}{r_q'}) \tag{4.4}$$

The r_q and r_q' are the segment PQ and PQ' between the charge q and the point P and the image charge q' and the point P respectively. If one sets

$$q'=-q \tag{4.5}$$

and takes P to be a point on the surface with potential V_s, (4.4) can be expressed:

$$V_s=\frac{q}{2\pi\varepsilon}\ln(\frac{r_q'}{r_q}) \tag{4.6}$$

This shows that the r_q'/r_q is a constant as a result of a constant V_s. In addition, since the surface is cylindrical, the relationship of (4.6) must hold at all points on the cylinder surface. Therefore, to

show how this constraint applies to the ratio, a similar triangle shown in Fig.4.3 can be used (see the points $\Delta O_1PQ' \sim \Delta O_1QP$). Based upon that fact it is a similar triangle, it can be shown that

$$\frac{R_c}{a} = \frac{b}{R_c} = \frac{r_q'}{r_q} \tag{4.7}$$

Hence, the image location within the inner conductor region can be found from (4.7) to be

$$b = \frac{R_c^2}{a} \tag{4.8}$$

Combining (4.4), (4.5) and (4.8), the potential from the line charge and image charge can be calculated through the dielectric.

Similarly, in the case of a linear equipotential surface, the MoI can be applied as shown in Fig.4.4 wherein a line of charge q C/m is located at r= a m away from the linear equal potential surface L. The distribution in the space is described with an implementation of an image charge q' located at b, whose charge value q' and location b are as follows:

$$\begin{cases} q' = -q \\ b = -a \end{cases} \tag{4.9}$$

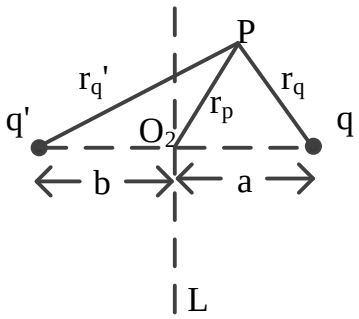

Fig.4.4 Method of images for a linear equal potential surface

In the specific case of the multi-conductor shown in Fig.4.1, multiple image charges are required to approximate the flux lines. To begin, to solve for the boundary condition B_{1p}, all

equipotential surfaces are removed and replaced with a line of charge q_0 that is placed at R_c, the center of the inner positive conductor. This line of charge yields an equipotential at the boundary B_{1p} as shown in Fig.4.5, where red dashed lines represent the electric flux generated by the line of charge q_0. However, the introduction of this line of charge distorts the potential at the boundary B_2.

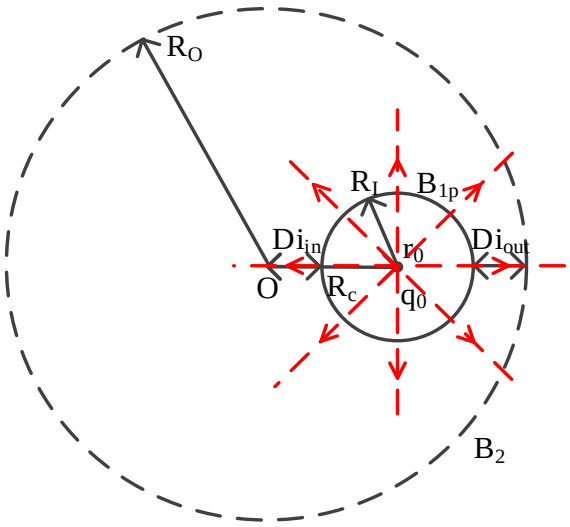

Fig.4.5 Placement of q_0

To satisfy the boundary B_2, an image charge q_1^- is implemented at the location r_1^- by applying the MoI for a cylindrical equipotential surface depicted in Fig.4.3. In the specific case of boundary B_2 as shown in Fig.4.6, the MoI is applied in an inverse order where the charge pair of $\{q_1^-, q_0\}$ is equivalent to $\{q, q'\}$ in Fig.4.3, respectively. As a result, the values of the image line charge q_1^- and r_1^- are expressed

$$\begin{aligned} q_1^- &= -q_0 \\ r_1^- &= \frac{R_O^2}{R_c} \end{aligned} \tag{4.10}$$

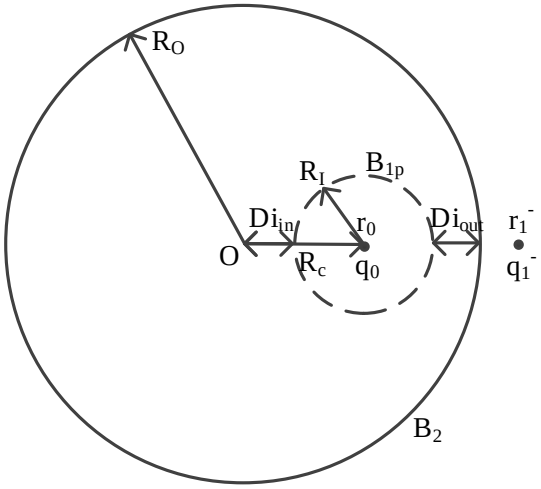

Fig.4.6 Placement of q_1^-

Subsequently, the placement of q_1^- generates a distortion on boundary B_{1p} which is the dashed circle in Fig.4.6. To compensate for this distortion, an additional image line of charge q_1^+ is implemented at the location r_1^+ by applying the MoI depicted in Fig.4.3. Specifically, this pair of line of charges $\left\{q_1^-, q_1^+\right\}$ is equivalent to $\left\{q, q'\right\}$ in Fig.4.3. This pair is constructed about the center of the inner conductor as shown in Fig.4.7. As a result, the values of the image line of charge q_1^+ and r_1^+ are expressed

$$\begin{aligned} q_1^+ &= -q_1^- = q_0 \\ r_1^+ &= \frac{R_I^2}{r_1^- - R_c} + R_c \end{aligned} \tag{4.11}$$

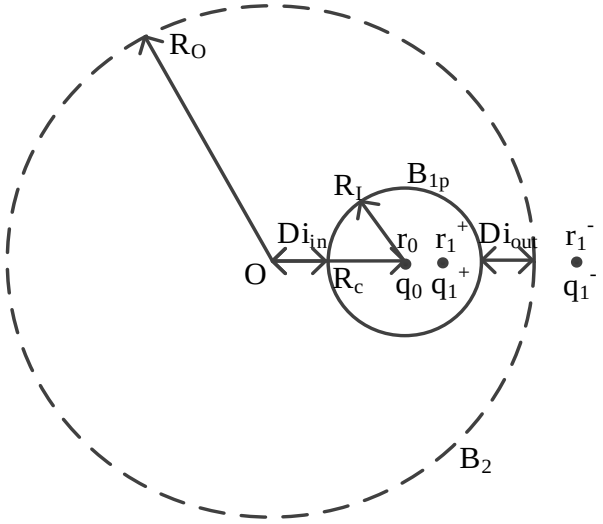

Fig.4.7 Placement of q_1^+

Similarly, the implementation of q_1^- introduces a distortion on boundary B_2 (the dashed circle) as shown in Fig.4.7. Additional image charges are implemented to solve the un-equipotential generated by the previous image charges. An approximate solution to satisfy both boundary condition B_{1p} and B_2 is reached by implementing multiple image charges as shown in Fig.4.8. Specifically, the image charges q_i^- and q_i^+ are added to the geometry repetitively and their respective values and locations are:

$$\begin{aligned} q_i^- &= -q_0 \\ r_1^- &= \frac{R_O^2}{R_c} \\ r_i^- &= \frac{R_O^2}{r_{i-1}^+}, i > 1 \end{aligned} \tag{4.12}$$

and

$$\begin{aligned} q_i^+ &= -q_i^- = q_0 \\ r_i^+ &= \frac{R_I^2}{r_i^- - R_c} + R_c \end{aligned} \tag{4.13}$$

where i is the i[th] pair of image charge. The number of charges is user-defined, where an increase in the number yields flux lines tending toward a Laplacian distribution. In practice it has been found that on the order of 10 yields reasonable results.

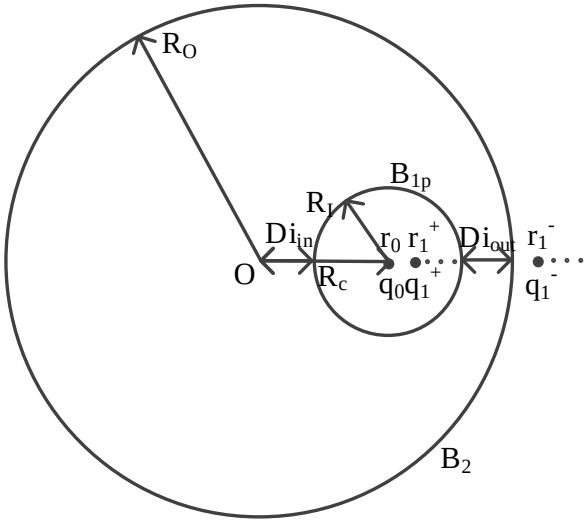

Fig.4.8 Placement of positive charge set

To satisfy the boundary condition B_3, image charges can be implemented using the locations depicted in Fig.4.4. In the specific case shown in Fig.4.8, an image charge set $\left\{q_{n0}, q_{ni}^{-}, q_{ni}^{+}\right\}$ is implemented as a reflection of the charge set $\left\{q_0, q_i^{-}, q_i^{+}\right\}$ about the center boundary B_3. As a result, the values of the charges are:

$$\begin{aligned} q_{n0} &= -q_0 \\ q_{ni}^{-} &= -q_{n0} \\ q_{ni}^{+} &= q_{n0} \end{aligned} \tag{4.14}$$

and their respective locations are at:

$$\begin{aligned} r_{n0} &= -R_c \\ r_{ni}^{-} &= -r_i^{-} \\ r_{ni}^{+} &= -r_i^{+} \end{aligned} \tag{4.15}$$

It is noted that, placement of the charge set $\left\{q_{n0}, q_{ni}^{-}, q_{ni}^{+}\right\}$ to satisfy B_3 also sets up equipotential surfaces at B_{1n} and B_2, respectively provided that the original charges to satisfy B_{1p} and B_2 are not considered. In practice, introduction of (4.14) and (4.15) yields a deviation in the flux lines introduced by (4.12) and (4.13). In other words, setting the charges that satisfy B1n and B2 will distort the lines introduced by the charges set to satisfy B_{1p}. This yields some error, particularly close to the respective inner conductor. To reduce the error, the influence of (4.14) and (4.15) on the field lines calculated around the inner conductor are suppressed by introducing a weighting coefficient. Specifically, at a radius of greater than R_I+Di_{in} around the inner conductors, all test charges are used in evaluating the electric field. As one tends toward the inner positive conductor a weighting function, which is introduced Section 4.3, is applied wherein the influence of (4.14) and (4.15) are decreased linearly so that at the conductor/dielectric interface their influence is zero. Similar weighting is applied to (4.12) and (4.13) when calculating the electric field around the negative conductor.

For the case of the thermal circuit, similar charge distributions are applied with the exception that equal charges are placed on either side of the center line, which are expressed:

$$\begin{aligned} q_i^{-} &= -q_0 \\ q_i^{+} &= q_0 \\ q_{n0} &= q_0 \\ q_{ni}^{-} &= -q_{n0} \\ q_{ni}^{+} &= q_{n0} \end{aligned} \tag{4.16}$$

These are placed at

$$
\begin{aligned}
r_1^- &= \frac{R_O^2}{R_c} \\
r_i^- &= \frac{R_O^2}{r_{i-1}^+}, i > 1 \\
r_i^+ &= \frac{R_I^2}{r_i^- - R_c} + R_c \\
r_{n0} &= -R_c \\
r_{ni}^- &= -r_i^- \\
r_{ni}^+ &= -r_i^+
\end{aligned}
\tag{4.17}
$$

respectively. It is noted that the charge polarity does not change when applying the images to the negative conductor due to the fact that the heat source does not have polarity. In Fig.4.9, it is also noted that all the image charges are placed either inside the inner conductors or outside the outer conductors. There is no image charge inside the region of the dielectric.

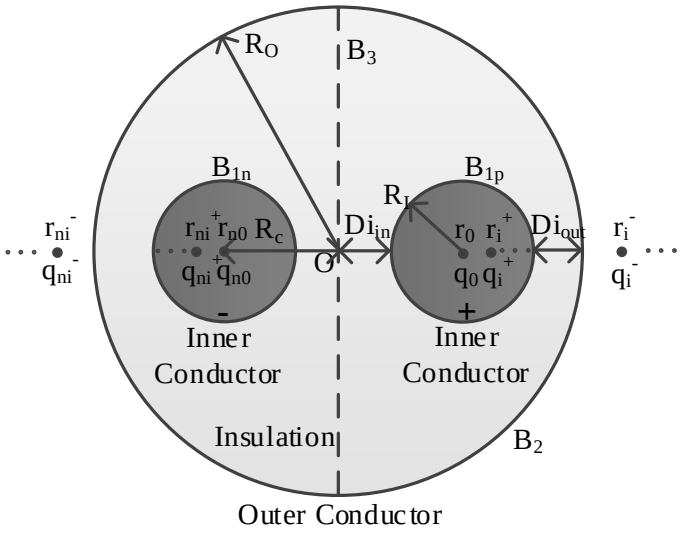

Fig.4.9 Placement of all charges

4.3 Flux Tube Construction

Due to the symmetry of the cable, only the first quarter of the cable is needed to be considered, or the first quadrant of a Cartesian coordinate system as shown in the Fig.4.10. Once

the MoI is used to establish the location of the charges using (4.12)-(4.17), flux tube boundaries are found by first placing a test charge at the surface of the respective inner conductor and establishing its trajectory based upon the net force acting due to all charges at its respective location. This is repeated by placing test charges at several initial locations on the circumference of the inner conductors. By the definition of an equivalent flux tube, there are no flux lines across the side surface of a tube. As a result, these trajectories can be taken as the boundaries of the tubes.

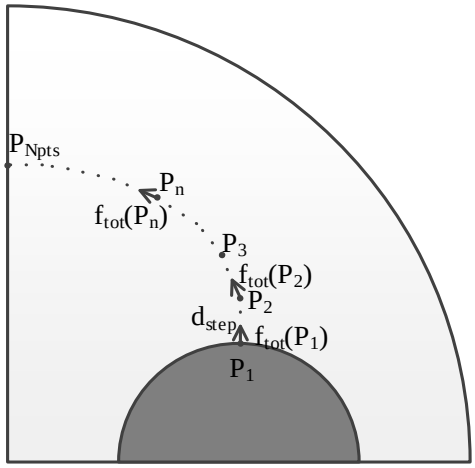

Fig.4.10 Pathfinding algorithm

To find the path of the flux lines, one may suggest to start on the inner conductor boundary, say point P_1 as shown in Fig.4.10. The net force $\vec{f}_{tot}$ of the charge q_0 and all the image charges, q_i^- and q_i^+, q_{n0}, q_{ni}^-, and q_{ni}^+, are calculated at the point P_1. The next possible point P_2 is then approached by adding an incremental step in the direction of the net force. A formula for this pathfinding/traverse approach is:

$$P_n = P_{n-1} + \vec{f}_{tot}(P_{n-1}) \cdot d_{step} \tag{4.18}$$

$$d_{step} = \frac{\min(Di_{in}, Di_{out})}{N_{step}} \tag{4.19}$$

$$\vec{f}_{tot}(P)=\frac{q_0}{\left|\vec{r}_{P,q_0}\right|^2}\cdot\vec{r}_{P,q_0}+\vec{f}_{moi}\left(P,q^-\right)+\vec{f}_{moi}\left(P,q^+\right)$$
$$+\alpha\left(\frac{q_{n0}}{\left|\vec{r}_{P,q_{n0}}\right|^2}\cdot\vec{r}_{P,q_{n0}}+\vec{f}_{moi}\left(P,q_n^-\right)+\vec{f}_{moi}\left(P,q_n^+\right)\right) \tag{4.20}$$

$$\vec{f}_{moi}(P,q)=\sum_{i=1}^{N_{layer}}\frac{q_i}{\left|\vec{r}_{P,q_i}\right|^2}\cdot\vec{r}_{P,q_i} \tag{4.21}$$

$$\alpha(P)=\min\left(\frac{\left|\vec{R}(P)-\vec{R}(R_c)\right|-R_i}{Di_{in}},1\right) \tag{4.22}$$

$$\vec{r}_{P,q}=\vec{R}(P)-\vec{R}(q) \tag{4.23}$$

The incremental step d_{step} is selected as the shorter distance of the dielectric thickness Di_{in} and Di_{out} divided by a discretization level N_{step} which is shown in (4.19). The net force $\vec{f}_{tot}(P)$ and the net force of one image charge set $\vec{f}_{moi}(P,q)$ at the point P are shown in (4.20) and (4.21) where the weighting coefficient $\alpha(P)$ (described previously) in (4.22) is added in the function to balance the force acting to the specific locations that is near the inner conductor B_{1p} due to the other inner conductor. $\vec{R}(R_c)$ in (4.22) stands for the vector distance from center O to the center of the positive inner conductor. The coefficient $\alpha(P)$ is zero near the inner boundary B_{1p} and reaches a maximum of 1 when approaching the center line B_3 or locations at a further distance. The vector distance from charge locations towards the point P is shown in (4.23). Finally, the pathfinding ends once the test charges reaches the outer conductor or the centerline. This pathfinding approach is repeatedly applied to the half circumference of the inner conductor at an angular spacing $\theta_{spacing}$ with a discretization number of N_{span}:

$$\theta_{spacing} = \frac{\pi}{N_{span}} \tag{4.24}$$

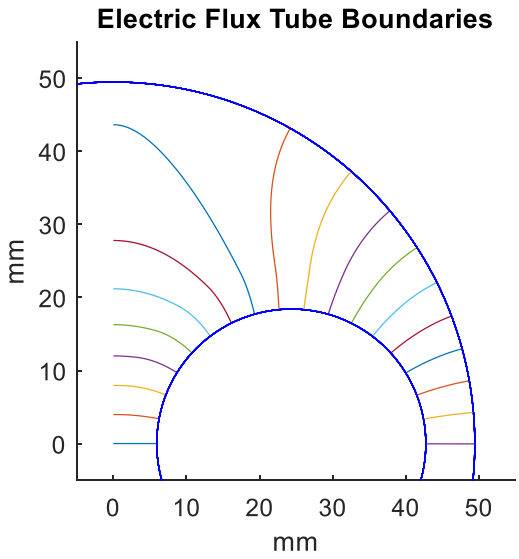

Fig.4.11 Electric tube boundaries obtained using MoI

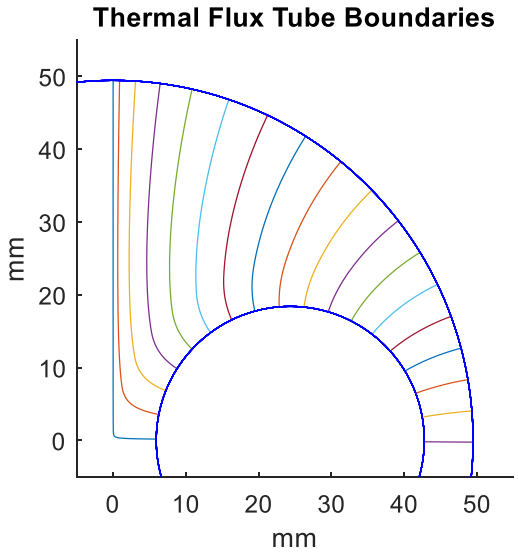

Fig.4.12 Thermal tube boundaries obtained using MoI

Representative tube geometries for the electric flux and the thermal flux are shown in Fig.4.11 and Fig.4.12 for a conductor with parameters shown in Table 4.1. A representative flux tube distribution is constructed with the tube discretization number N_{step}=10 and the angular discretization number N_{span}=18. It can be observed that electric flux tubes in Fig.4.11 start on the inner conductor and end on the center line and the outer conductor perpendicularly where both boundaries have zero potentials during normal operation. In contrast, the thermal flux tubes in Fig.4.12 start on the inner conductor and end only on the outer conductor perpendicularly due to the same heat sources present on both inner conductors.

In practice it is difficult to establish a closed form expression relating the surface potential to tube flux for the tube geometries shown in Fig.4.11 and Fig.4.12. To enable the local electric field and thermal evaluation, the flux tubes are further partitioned by a discretization level N_{pts} as shown in Fig.4.13 and Fig.4.14. To do so a matrix, denoted as *A*, of nodes is constructed using the vertexes of all equivalent tubes. The entries of matrix *A* are the coordinates of the nodes denoted as $a_{m,n}$, where m and n are the mth layer and the nth local flux tube respectively. To enable evaluation, the quadrilateral-shape flux tubes are further partitioned into pseudo-parallelograms, whose inner edge faces towards the respective inner conductor and outer edge faces the outside edge of the cable. A representative parallelogram is shown in Fig.4.17. The $\theta_{1,m,n}$, $\theta_{2,m,n}$, $h_{1,m,n}$, and $h_{2,m,n}$ are the inner angles and the heights of the representative parallelogram. The inner angles can be found by applying the Law of Cosines and vector calculus as:

$$\cos\left(\theta_{1,m,n}\right)=\frac{\left(\vec{R}(a_{m+1,n})-\vec{R}(a_{m,n})\right)\cdot\left(\vec{R}(a_{m,n+1})-\vec{R}(a_{m,n})\right)}{\left|\vec{R}(a_{m+1,n})-\vec{R}(a_{m,n})\right|\left|\vec{R}(a_{m,n+1})-\vec{R}(a_{m,n})\right|} \tag{4.25}$$

$$\cos\left(\theta_{2,m,n}\right)=\frac{\left(\vec{R}(a_{m+1,n})-\vec{R}(a_{m+1,n+1})\right)\cdot\left(\vec{R}(a_{m,n+1})-\vec{R}(a_{m+1,n+1})\right)}{\left|\vec{R}(a_{m+1,n})-\vec{R}(a_{m+1,n+1})\right|\left|\vec{R}(a_{m,n+1})-\vec{R}(a_{m+1,n+1})\right|} \tag{4.26}$$

where $\vec{R}(a_{m,n})$ is the vector location of the vertex $a_{m,n}$. The heights of the parallelogram can be expressed using (4.25) and (4.26),

$$h_{1,m,n} = \left|\vec{R}(a_{m+1,n}) - \vec{R}(a_{m,n})\right| \sin\left(\theta_{1,m,n}\right) = \left|\vec{R}(a_{m+1,n}) - \vec{R}(a_{m,n})\right| \sqrt{1-\cos^2\left(\theta_{1,m,n}\right)} \tag{4.27}$$

$$h_{2,m,n} = \left|\vec{R}(a_{m,n+1}) - \vec{R}(a_{m+1,n+1})\right| \sin\left(\theta_{2,m,n}\right) = \left|\vec{R}(a_{m,n+1}) - \vec{R}(a_{m+1,n+1})\right| \sqrt{1-\cos^2\left(\theta_{2,m,n}\right)} \tag{4.28}$$

The mean cross-sectional area $A_{rct}\left(m,n\right)$ and the mean length $l_{rct}\left(m,n\right)$ of the $\left(m,n\right)^{th}$ parallelogram are expressed in (4.29)-(4.30).

$$A_{rct}\left(m,n\right) = \frac{h_{1,m,n} + h_{2,m,n}}{2} l_d \tag{4.29}$$

$$l_{rct}(m,n) = \frac{\left|\left(\vec{R}(a_{m,n}) - \vec{R}(a_{m,n+1})\right) + \left(\vec{R}(a_{m+1,n}) - \vec{R}(a_{m+1,n+1})\right)\right|}{2} \tag{4.30}$$

where l_d is the unit length into the page.

As a result, the basic dimensions of a flux tube including the mean cross-sectional areas and the mean lengths can be used for the calculations of the flux tubes. Each electric tube is represented using a parallel resistance/capacitance of the form:

$$R_{m,n} = \frac{l_{rct}\left(m,n\right)}{\sigma A_{rct}\left(m,n\right)} \tag{4.31}$$

$$C_{m,n} = \frac{\varepsilon A_{rct}\left(m,n\right)}{l_{rct}\left(m,n\right)} \tag{4.32}$$

Each thermal tube is represented using a T-circuit model with resistances and capacitance defined:

$$R_{\Omega or,m,n} = R_{\Omega ir,m,n} = \frac{l_{rct}\left(m,n\right)}{2kA_{rct}\left(m,n\right)} \tag{4.33}$$

$$C_{\Omega,m,n} = \rho C_p A_{rct}\left(m,n\right) l_{rct}\left(m,n\right) \tag{4.34}$$

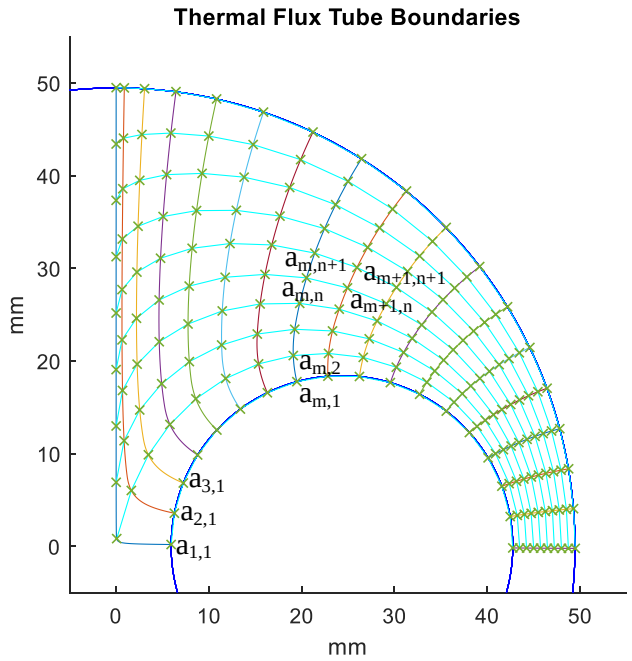

Fig.4.13 Thermal rectangular flux tube discretization

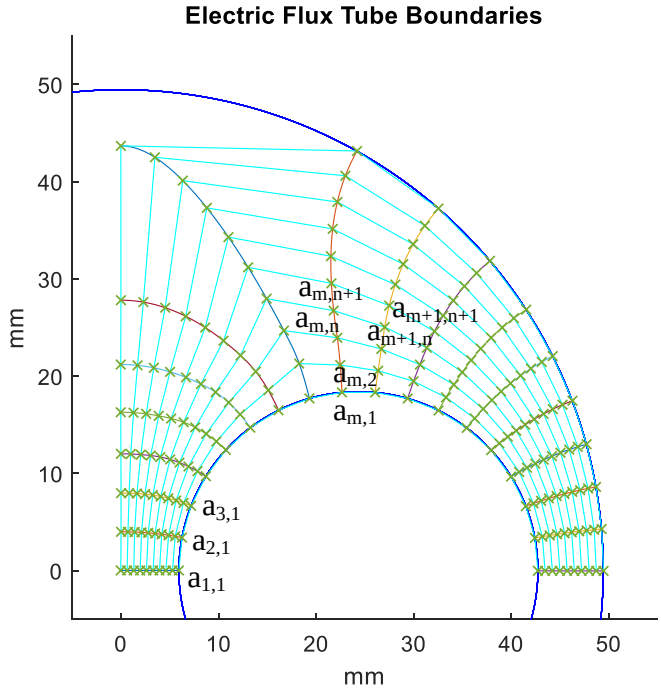

Fig.4.14 Electric rectangular flux tube discretization

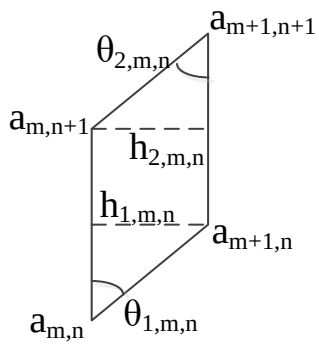

Fig.4.15 Parallelogram flux tube discretization

4.4 Equivalent Circuit Model

Using the flux tube parameters of (4.31)-(4.34), electric and thermal equivalent circuits are established as shown in Fig.4.16 and Fig.4.17. Therein V_{op}, $R_{t,n}$, P_L, $T_{\Omega ir}$, $T_{\Omega or}$, and T_{amb} are the operating voltage from the inner positive conductor to the outer conductor, the small resistance of the associated tube, the resistive heat loss of the inner conductor, the temperature at the inner conductor and the temperature at the outer conductor, and the ambient temperature, respectively. In both the electric and thermal circuits, the circuit elements of the partitioned flux tubes are connected in series starting with the voltage/heat current source at the inner conductors and ending with ground/ambient voltage source at the outer conductor. Each serial-connected section is then connected in parallel with neighboring series sections that are representing the flux paths at the neighboring angular positions. In the electric circuit calculation, the small resistances are placed in series with the associated tubes for input/output compatibility between the source (voltage in/current out) and the RLC circuit (voltage out/current in). A similar circuit construction is detailed in [5] for a coaxial cable. However, unlike the coaxial cable, the thermal and electric circuits in a multi-conductor cable do not share the same partitioned geometry as shown in Fig.4.11,

Fig.4.12, Fig.4.16, and Fig.4.17. It is noted that the locations of the thermal and electric flux tubes are not identical. Therefore, within the electric flux tubes, the temperature needed to establish conductivity is obtained through interpolation. In practice, both the thermal and electric models are expressed in a state model form wherein the capacitor voltages are the states. The solution of the state model can be obtained using any one of a number of integration algorithms. The two circuits are then evaluated accordingly at each time step.

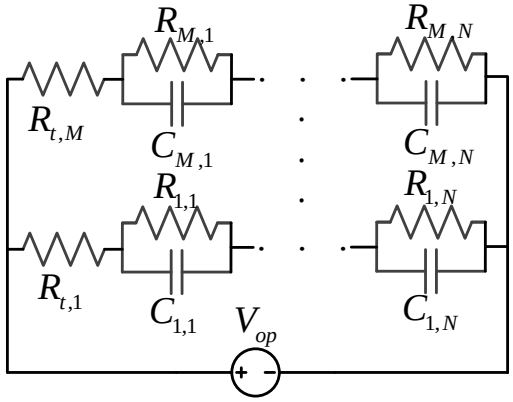

Fig.4.16 Electric equivalent circuit construction

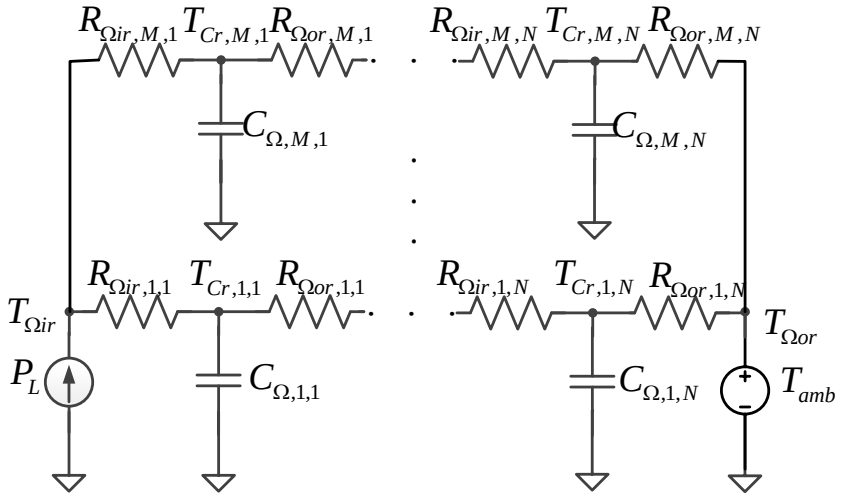

Fig.4.17 Thermal equivalent circuit construction

4.5 Case Study and Validation

To validate the modeling approach, the behavior predicted by the coupled circuits is compared with data acquired from the commercial Finite Element Analysis (FEA) tool COMSOL. The geometric and material parameters for the cable are given in Table 4.1. It is assumed the cable is operating at a voltage of ±10kV (inner conductor with respect to ground) with a conductor current of 1500 A. It is further assumed that the outer conductor/shield maintains an ambient temperature of 25^{o}C. The conductor heat loss is 35.3 W/m. The flux tube is constructed with the tube discretization number N_{step}=10 and the angular discretization number N_{span}=36. The behavior of the electric field is first predicted assuming that the system is at the ambient temperature. Subsequently, the thermal and electric circuits are simulated to a steady state. The resulting temperature and electric field are calculated from the center point O to the outer shield (in a direction toward to the + inner conductor). The results are shown in Fig.4.19-Fig.4.22. From the plots, one can observe that the temperature exhibits a sharp gradient near the outer shield while maintaining a nearly constant temperature between the inner conductors. As a result, the electric field does not present a field-inversion effect between inner conductors. However, one observes a significant inversion between the inner conductors and the shield. Indeed, this inversion is due to the migration and distribution of space charge that results from the temperature gradient [8][9] [46][47][53]. One also notes that the behavior predicted by the equivalent circuit models closely match those obtained from the FEA.

Table 4.1 Multiconductor Parameters

Design Specification	
P_{out}	30MW
V_{OP}	±10kV
Geometric Parameters	
r_I	18.411mm
$Di_{\_in}$	5.9308mm
$Di_{\_out}$	6.7045mm
Conductor Parameters	
Material	Copper
conductivity	59.6×10^{6} S/m
Dielectric Parameters	
Material	XLPE
k_i	0.34 W/mK
A/σ_0	2.2896×10^{-6} $(\Omega m)^{-1}$
a	0.142×10^{-6} $(V/m)^{-1}$
b	7600 K
ε_r	4.2
Operating Condition	
P_L	70.5177M/m
M_C	24.08kg/m
A_C	$76.84cm^2$
ΔT	10.45 ^oC
R	1.578×10^{-5} Ω/m

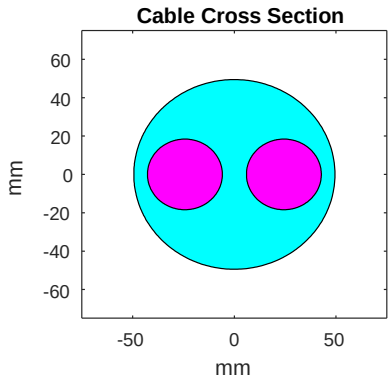

Fig.4.18 Cable cross sections

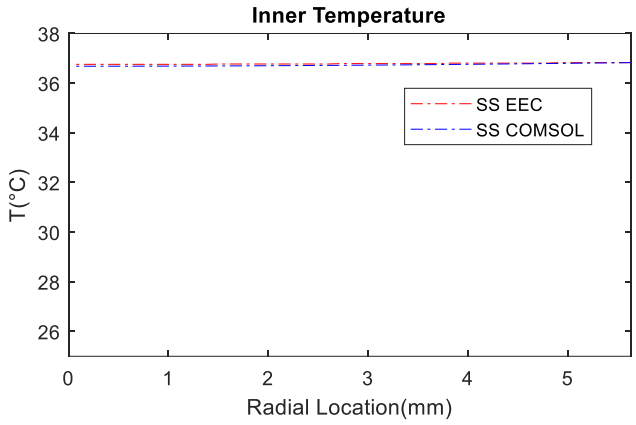

Fig.4.19 Inner radial thermal distribution

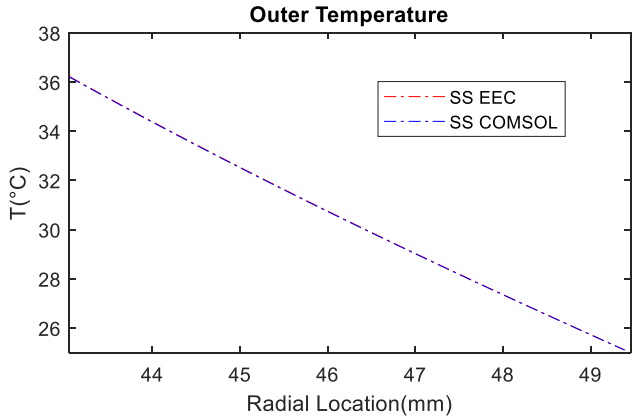

Fig.4.20 Outer radial thermal distribution

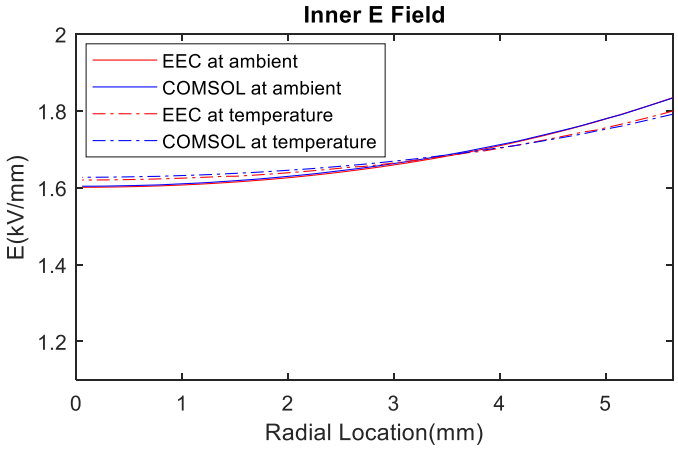

Fig.4.21 Inner radial electric field distribution

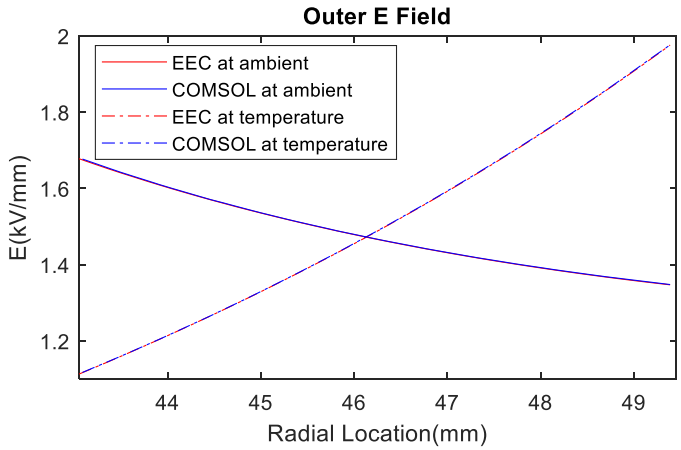

Fig.4.22 Outer radial electric field distribution

5. INCORPORATING CABLE MODELS WITHIN OPTIMIZATION AND SYSTEM SIMULATIONS

5.1 Introduction

In this chapter, the utility of the modeling approach proposed is demonstrated within a multi-objective design optimization of an MVDC cable. The optimization is performed using a Genetic Algorithm [26]. Subsequently, the use of the model within time-domain simulation of a power electronic based system is shown.

5.2 Multi-Objective Design of a Cable

5.2.1 Design objectives

A question arises as to which alternative cable geometry has the best performance under DC operation. To evaluate, it is necessary to consider a trade-off among the mass, efficiency and the volume of a cable. Herein, a cable design optimization is set forth in which a goal is to minimize the conductor power loss, the overall cable mass and volume under multiple design constraints. Hence, the three design objectives consist of the power loss per unit length P_L, the cable mass M_C and the cable cross sectional A_C shown in (5.1) and (5.2). The power loss and mass are computed on a per-meter-length. Expressions for these objectives for a coaxial cable and a multi-conductor cable are given respectively as:

$$\begin{cases} P_L = I_{op} R_I^2 \\ M_C = \rho_{cd} A_{cd} + \rho_{Di} A_{Di} \\ A_C = A_{cd} + A_{Di} \end{cases} \tag{5.1}$$

$$\begin{cases} P_L = 2 I_{OP} R_I^2 \\ M_C = 2\rho_{cd} A_{cd} + \rho_{di} A_{Di} \\ A_c = 2A_{cd} + A_{Di} \end{cases} \tag{5.2}$$

where ρ is the mass density of the material and the subscript *cd* and *Di* represent conductor and dielectric respectively. The cross sectional area of the conductor and dielectric layer of a coaxial cable and a multi-conductor cable can be further expanded as:

$$A_{cd} = \pi R_I^2 \tag{5.3}$$

$$A_{Di} = \pi\left(\left(R_I + Di_{in}\right)^2 - R_I^2\right) \tag{5.4}$$

and

$$A_{cd} = \pi R_I^2 \tag{5.5}$$

$$A_{Di} = \pi\left(\left(2R_{cd} + Di_{in} + Di_{out}\right)^2 - 2R_{cd}^2\right) \tag{5.6}$$

where R_I, Di_{in}, and Di_{out} are the radius of the (inner) conductor and the thickness of the (inner) dielectric layer and the thickness of the outer dielectric layer.

5.2.2 Design space and constraints

Four design variables (genes) are considered in this optimization for the single coaxial cable. These are the radius of the inner conductors R_I, the thickness of the dielectric D_i, the core material C_{cm}, and the operating voltage level V_{OP}:

$$\theta_s = \begin{bmatrix} R_I & D_i & C_{cm} & V_{OP} \end{bmatrix} \tag{5.7}$$

where the core material may be made from copper or aluminum. For the case of the multi-conductor cable, the genes also include the thickness of the inner and the outer dielectric Di_{in} and Di_{out} so that the design space is

$$\theta_s = \begin{bmatrix} R_I & Di_{in} & Di_{out} & C_{cm} & V_{OP} \end{bmatrix} \tag{5.8}$$

To ensure a robust design, the design constraints shown in shown in Table 5.1 and Table 5.2 are imposed when performing optimizations.

Table 5.1 Cable Constraints for Coaxial Cable

Constraint	Description	Values
$c_1 = \text{ltn}(J_C, J_{C\max})$	Max current density	1.5(1)A/mm^2 (Cu/Al)
$c_2 = \text{ltn}(\max(T), T_{\max})$	Max allowed temperature	90 ^{o}C
$c_3 = \text{ltn}(\max(\lvert E \rvert), E_{\max})$	Max long-life electric field	2 kV/mm
$c_4 = \text{ltn}(2(r_c + D_i), D_{\max})$	Max coaxial cable diameter	100 mm

Table 5.2 Cable Constraints for Multiconductor Cable

Constraint	Description	Values
$c_1 = \text{ltn}(\max(T), T_{\max})$	Max allowed temperature	90 ^{o}C
$c_2 = \text{ltn}(\max(\lvert E_{in} \rvert), E_{\max})$	Max long-life electric field	2 kV/mm
$c_3 = \text{ltn}(\max(\lvert E_{out} \rvert), E_{\max})$	Max long-life electric field	2 kV/mm
$c_4 = \text{ltn}(2(r_c + D_i), D_{\max})$ / $c_4 = \text{ltn}(2(2R_I + D_{in} + D_{out}), D_{\max})$	Max coaxial/multi-conductor cable diameter	200 mm / 200 mm

The first in Table 5.1 is the maximum current density within the conductor [10][35][36][37][38][39] where a fixed maximum current rating is used in this optimization as 1.5 A/mm^2 for copper and 1 A/mm^2 for aluminum [36][37][38][39]. The second and third in Table 5.1 and the first, second and third in Table 5.2 are the maximum allowed temperature and the maximum electric field for long life operation during the normal operations in the dielectric [26][35][36][37][38][39][40][41]. The maximum allowed temperature in XLPE is set to 90 ^{o}C [26][35][40][43]. The maximum electric field of 2 kV/mm to prevent dielectric breakdown [26][35][38][39][40][43]. The final is the diameter of the cable that is set to ensure a practical bend diameter.

Within the optimization, the constraints are imposed using a function of the form [26]:

$$\mathrm{ltn}\left(x, x_{\max}\right) = \begin{cases} 1 & x \le x_{\max} \\ \dfrac{1}{1 + x - x_{max}} & x > x_{\max} \end{cases} \tag{5.9}$$

The function evaluation returns 1 if the constraint is satisfied while an inverse evaluation is produced when it is not satisfied. The function approaches zero as x is much more beyond the maximum. To minimize the computational effort, the current density and bend radius constraints are evaluated prior to the initiation of the circuit simulation. Two constraint trackers are introduced to monitor the satisfaction of the constraints.

$$\begin{cases} C_I = C_I + 1 \\ C_S = C_S + c_i \end{cases} \tag{5.10}$$

where C_I, C_S and c_i are the total count of the constraints, the count of the satisfied constraints and constraint evaluation using (5.9) respectively.

5.2.3 Fitness evaluation

Upon the completion of an individual development, the fitness evaluation, F, of the individual is evaluated using:

$$F = \begin{cases} \varepsilon\left(\dfrac{C_s - C}{C}\right)\begin{bmatrix} 1 & 1 & 1 \end{bmatrix}^T & C_s < C_I \\ \begin{bmatrix} \dfrac{1}{P_L} & \dfrac{1}{M_C} & \dfrac{1}{A_C} \end{bmatrix}^T & C_s = C_I \end{cases} \tag{5.11}$$

where ε and C are a small positive number and the total amount of the constraints. The first fitness branch returns a small negative number vector when the constraint(s) are not met. The second fitness branch returns the inverse values of the three design objectives in order to minimize the three objectives.

5.2.4 Single conductor coaxial cable

A case study is set forth using a 30 MW 20 kV cable with the design specifications shown in Table 5.3. In this study, the operating voltage is fixed at 20kV.

Table 5.3 Cable Design Specifications & Space

Design Specification			
Specification	Value	Specification	Value
V_{op}	20kV	I_{op}	1500A
P_{out}	30MW	T_{amb}	25^{o}C
Design Space			
Parameter	Min	Max	Unit
r_c	1	50	mm
D_i	1	50	mm
C_{cm}	0	1	N/A

The optimization process is executed using a population size and the generation size of 800 by 800 for the purpose of both accuracy and efficiency. A 3-D Pareto-optimal front is shown in Fig.5.1 and the individual comparisons are shown in Fig.5.2. Three designs are extracted from the front and the corresponding specifications are displayed in the Table 5.4.The corresponding electric fields are shown in Fig.5.3. Comparing Design 1 and 2, one can observe that under the same power loss condition, copper-based cable designs have a smaller dimension while heavier mass due to the higher conductivity and higher mass density compared to aluminum. Interestingly, one may observe that Design 3 does not exhibit the field inversion due to less power loss and subsequent lower temperature drop.

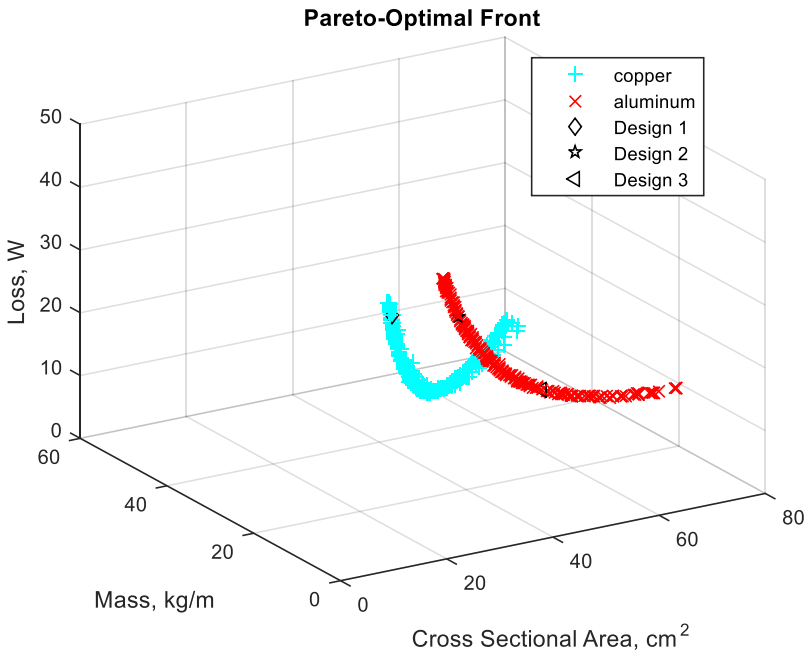

Fig.5.1 3D pareto-optimal front

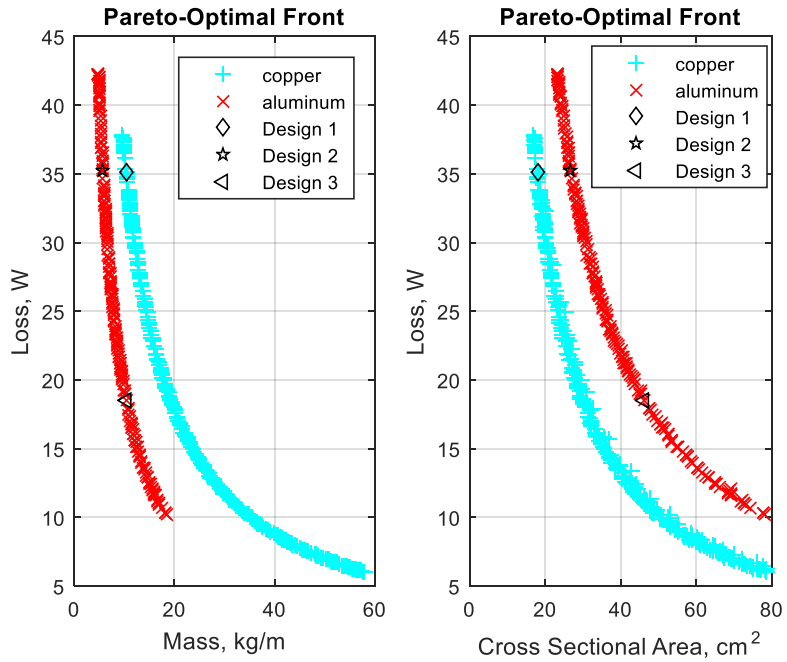

Fig.5.2 2D pareto-optimal front

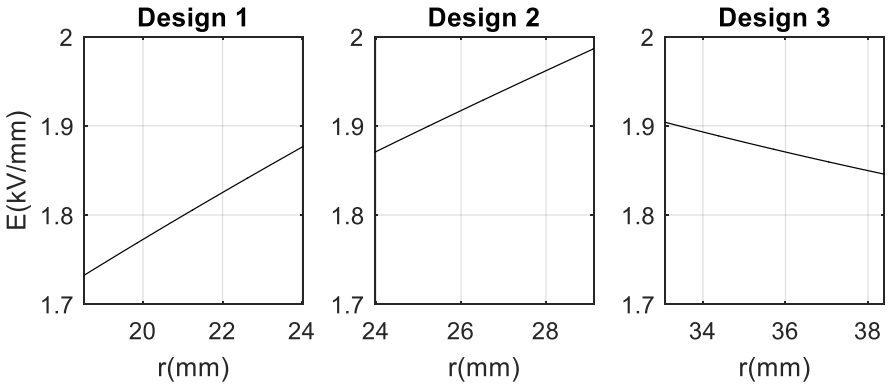

Fig.5.3 Electric field comparison from Design 1, 2 and 3

Table 5.4 Example Designs

Parameter	Design 1	Design 2	Design 3
r_c (mm)	18.504	23.953	33.072
D_i (mm)	5.538	5.184	5.336
P_L (W/m)	35.142	35.202	18.466
M_C (kg/m)	10.3039	5.645	10.356
A_C (cm^2)	18.158	26.671	46.344
C_{cm}	Cu	Al	Al
ΔT (^{o}C)	4.285	3.212	1.287
R (Ω/m)	1.562×10^{-5}	1.565×10^{-5}	8.207×10^{-6}

5.2.5 Multiconductor cable

The case study is compared with the multi-conductor cable which has the same design constraints with the exception that the allowable bend radius is doubled, which was found to enable a better comparison of Pareto fronts, with the recognition that some of the designs on the resulting front may be difficult to implement in the field. In order to compare the design using the multi-conductor cable, a second study is constructed with the coaxial cable using the design space shown in (5.7). In addition, the design constraint of maximum current density shown in Table 5.1 is neglected accordingly.

Table 5.5 Cable Design Specifications & Space

Design Specification			
Description	Value	Description	Value
P_{out}	30MW	T_{amb}	25°C
Design Space			
Parameter	Min	Max	Unit
R_I	1	50	mm
Di_{in}	1	50	mm
Di_{out}	1	50	mm
C_{cm}	0	1	N/A
V_{OP}	500	10000	V
Conductor Parameters			
σ_c(Cu)	36.9×10^6 S/m	σ_c(Al)	59.6×10^6 S/m
Dielectric Parameters			
k	0.34 W/mK	ε_r	4.2
σ_0	2.2896×10^{-6} $(\Omega m)^{-1}$	a	0.142×10^{-6} $(V/m)^{-1}$
b	7600 K		

The allowed range of genes and assumed material properties are shown in Table 5.5. The optimized design space solution is shown in Fig.5.4.The parameter number 1-5 represent the design space shown in (5.8) respectively and the normalized value represent the minimum and maximum value shown in Table 5.5. Viewing Gene 1 (R_I), it is noted that there are two separate conductor sizes corresponding to the two core conductor materials. The thickness of the inner dielectric Di_{in}, Gene 2, is relatively constant due to the fact that the inner electric field has a relatively flat distribution as depicted in Fig.4.21. As a result, the Di_{in} is optimized to a value to meet the maximum electric field of 2kV/mm. In contrast, the thickness of the outer dielectric Di_{out}, Gene 3, varies with the inner conductor radius R_I which is proportional to the power loss P_L. This is due to the fact that the field inversion increases the maximum electric field in the dielectric as depicted in Fig.4.22. To stay within the field constraint, the thickness of the outer dielectric changes with R_I. One also notes that the optimal operating voltage Gene 5 is at the maximum voltage upper limit so that the power loss P_L can be minimized.

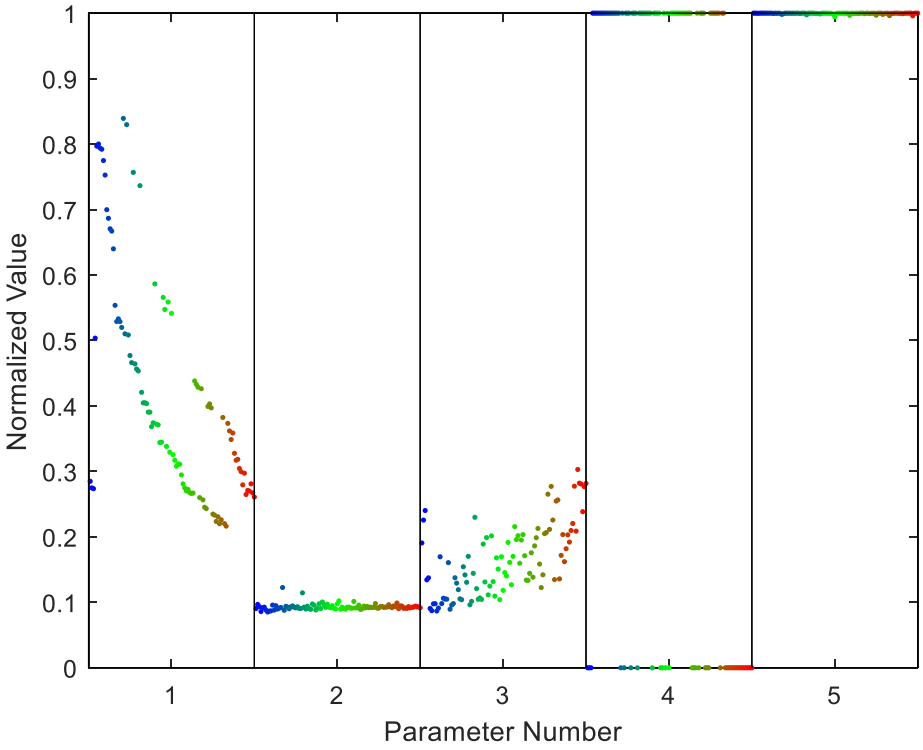

Fig.5.4 Design space

A 2-D Pareto-optimal front showing the mass, loss and cross-sectional area from the optimization study are shown in Fig.5.5 along with the results of the optimization of the single – conductor (coaxial) design operating under the same specifications. In addition, the individual comparisons are also shown in Fig.5.5. Three design specifications from the Pareto-optimal fronts are shown in Table 5.6. The corresponding cable geometries are shown in Fig.5.6. The green dashed line is the presented in Fig.5.5 to indicate the maximum cross-sectional area (~78.5cm^2) of the maximum practical bending diameter of 100mm. Comparing the Design 1 and 3, one can observe that under the same power loss condition, the radii of the core conductors and the dielectric thickness in the both cable geometries have similar values due to the fact that the majority of the heat loss are from the conductor resistive loss. However, the temperature in the multi-conductor

cable is higher due to the two heat sources. Although similar dimensions, the Design 3 has a greater mass and size due the increase in dielectric area between the two conductors.

Comparing Design 2 and 3, which have similar cross-sectional areas, Design 2 has a much larger conductor size which reduces the power loss and the subsequent temperature drop in the cable. On the other hand, Design 2 is heavier than Design 3 due to the larger core conductors.

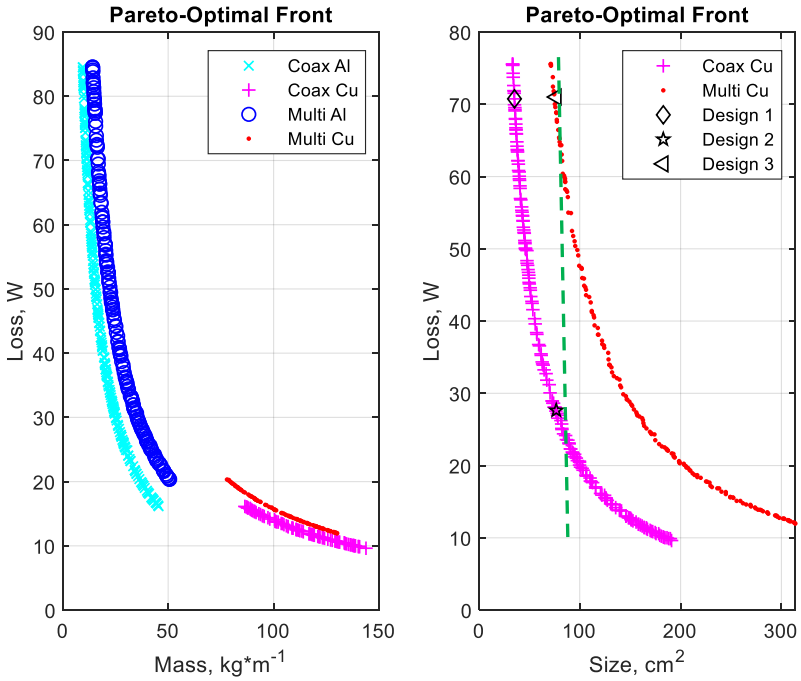

Fig.5.5 Pareto-optimal fronts of the two studies

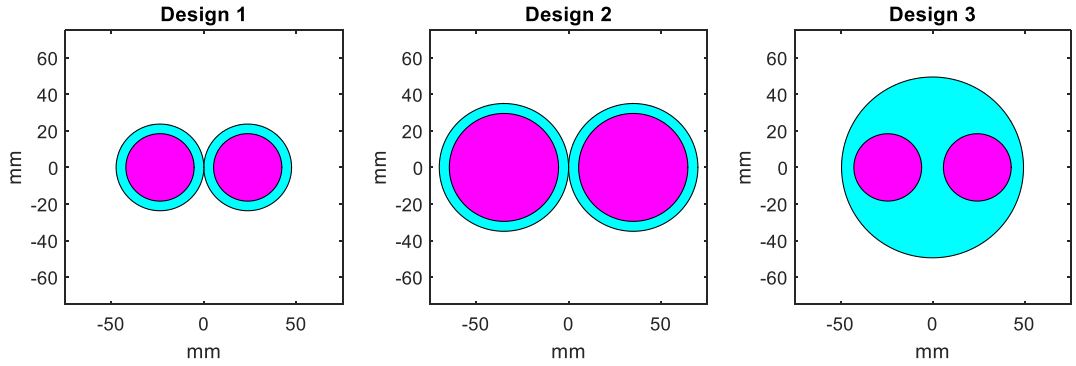

Fig.5.6 Cable cross sections

Table 5.6 Example Designs

Parameter	Design1	Design2	Design3
V_{OP}	10kV	10kV	10kV
R_I (mm)	18.442	29.513	18.411
$Di_{\_in}$(mm)	5.2622	5.4336	5.9308
$Di_{\_out}$ (mm)	-	-	6.7045
P_L (W/m)	70.75	27.63	70.5177
M_C (kg/m)	20.4	51.02	24.08
A_C (cm^2)	35.3	76.73	76.84
C_{cm}	Cu	Cu	Cu
ΔT (°C)	3.74	0.98	10.45
R (Ω/m)	1.572×10^{-5}	6.140×10^{-6}	1.578×10^{-5}

5.3 Cable Model in Simulation

To further illustrate the use of the model, the MVDC cable model is implemented in a system level simulation and introduced within a rectifier system and a resistive load similar to that used for the Auxiliary Power Generation Module (APGM) in [7]. The topology is shown in Fig.5.7. Its controls are shown in Fig.5.8. The parameters of the system are shown in Table 5.7 and Table 5.8. They were obtained by applying a per-unit transformation to the APGM of [7] from 750 V 9 kW to a 20 kV 30 MW base. A 100 m cable system is deployed and simulated between the output filter of the rectifier and the load. The cable parameters are those of Design 1 in Table 5.4.

The system shown in Fig.5.7 is powered by a Permanent-Magnet AC machine. An AC-DC rectifier is connected to the PMAC. An LC DC low pass filter is implemented between the AC-DC rectifier and the load system. A voltage regulator is provided aiming to control the gate signals by monitoring the PMAC rotor angle, θ_r , a and b phase current, i_{as} and i_{bs}, and the DC bus voltage across the capacitor in the low pass filter. The power-deliver cable model is introduced between

the inductor in the low pass filter and the load system. The cable is assumed to be a π shape model of a short transmission line, shown in Fig.5.9, due to the fact of the relatively short transmission distance. The inductance $L_{cab,series}$ of the cable is negligible due to the small value of the inductance compared to the inductor value of the adjacent LC filter and the consideration of the computational effort required to include such a small value. To further simply the computation and comply with the coupled thermal/electric circuit model, the shunt resistance $r_{cab,shunt}$ and the capacitance C_{cab} of the cable are concentrated in the left leg of the π circuit to analyze the electric field and the space charge in the worst case scenario during fault condition. Subsequently, the cable resistance and the capacitance of the dielectric derived in the electric equivalent circuit model is equivalent to the shunt resistance $r_{cab,shunt}$ and the corresponding parallel capacitance C_{cab} in the transmission line model. The cable resistance $r_{cab,series}$ of the conductor is implemented after the electric equivalent circuit branch connecting the low pass filter and the load system. Herein, the new cable model can be shown in Fig.5.10 where the block called cable system consists of cable resistance $r_{cab,shunt}$ and capacitance C_{cab}. To further implement the modified π shape model into Fig.5.7, a detailed positive cable system is specified in Fig.5.11. The negative cable system can be derived similarly.

To construct the simulation model, the voltages of the cable capacitance $v_{cab,+}$ and $v_{cab,-}$ is selected as the state variable. The voltage v_{apgm} after the filter can be expressed as,

$$v_{apgm} = v_{cab,+} - v_{cab,-} \tag{5.12}$$

$$v_{cab,+} = \sum_{n=1}^{N} v_{cab,n+} \tag{5.13}$$

$$v_{cab,-} = \sum_{n=1}^{N} v_{cab,n-} \tag{5.14}$$

, where $v_{cab,n+}$ and $v_{cab,n-}$ are the voltage of the n[th] capacitance tubes. With the same cable geometry and length, the voltage of positive and negative cable have the same value under unfaulted conditions.

The load current is calculated using

$$i_L = \frac{v_{apgm}}{2r_{cab} + r_{load}} \tag{5.15}$$

The total current $i_{cab,+}$ that flows into the positive cable system is then expressed

$$i_{cab,+} = i_{apgm} - i_L \tag{5.16}$$

Subsequently, the capacitor currents in each RC branch in the positive cable system is are,

$$i_{C,n} = i_{cab,+} - \frac{v_{C,n}}{r_{cab,N}} \tag{5.17}$$

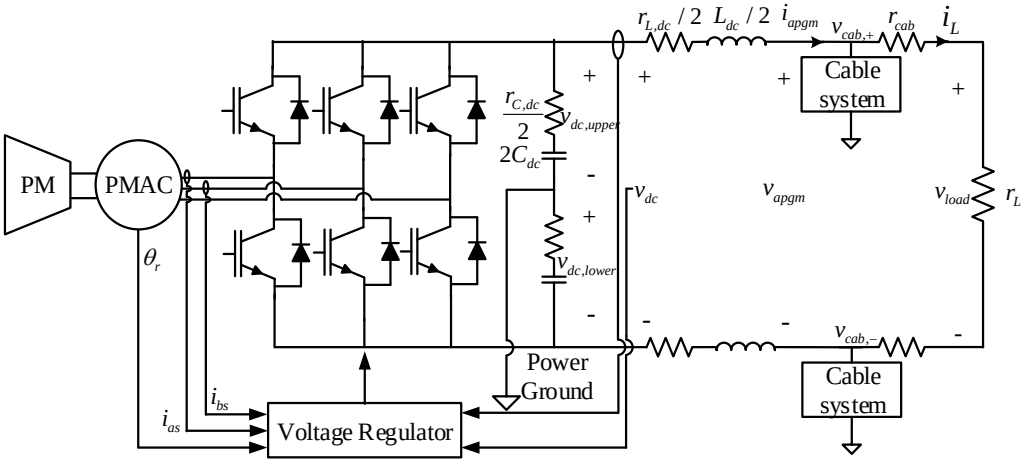

Fig.5.7 Active Bridge PMAC Generation

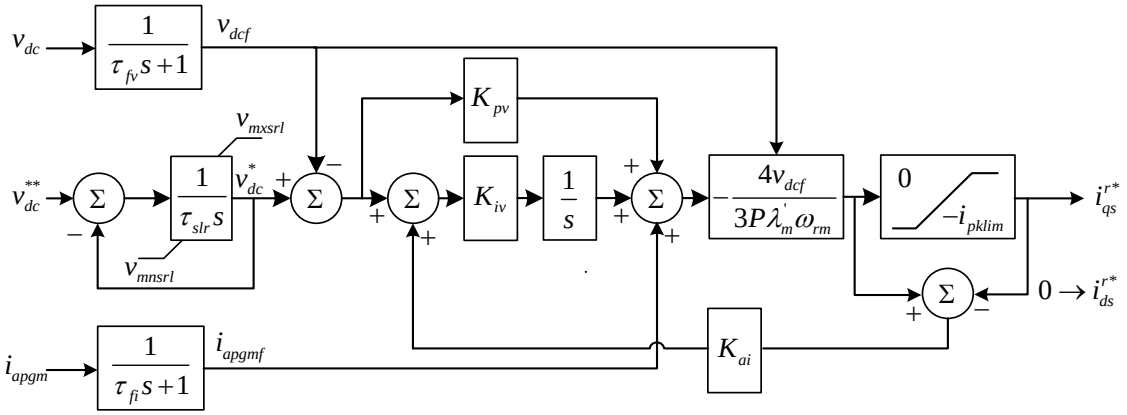

Fig.5.8 Voltage regulator control block

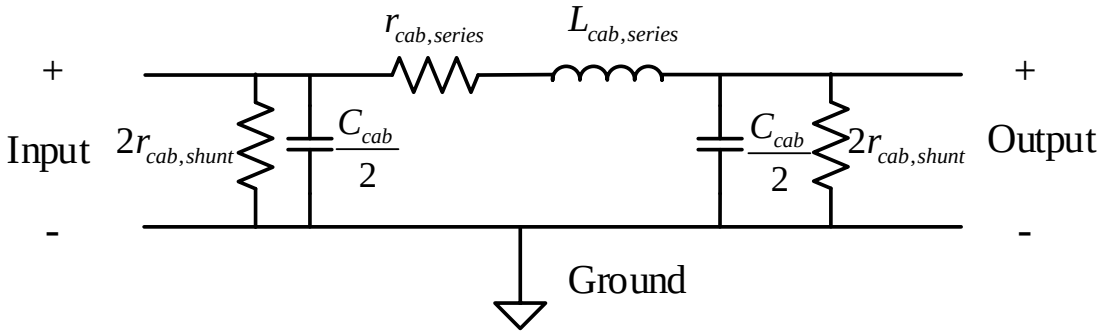

Fig.5.9 The π shape model of a transmission line

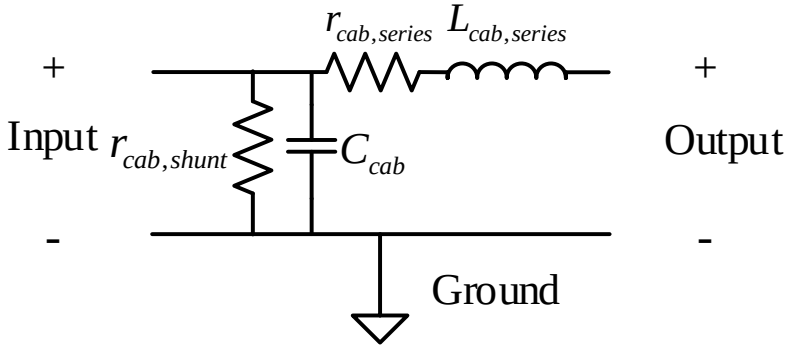

Fig.5.10 The modified π shape model of a transmission line

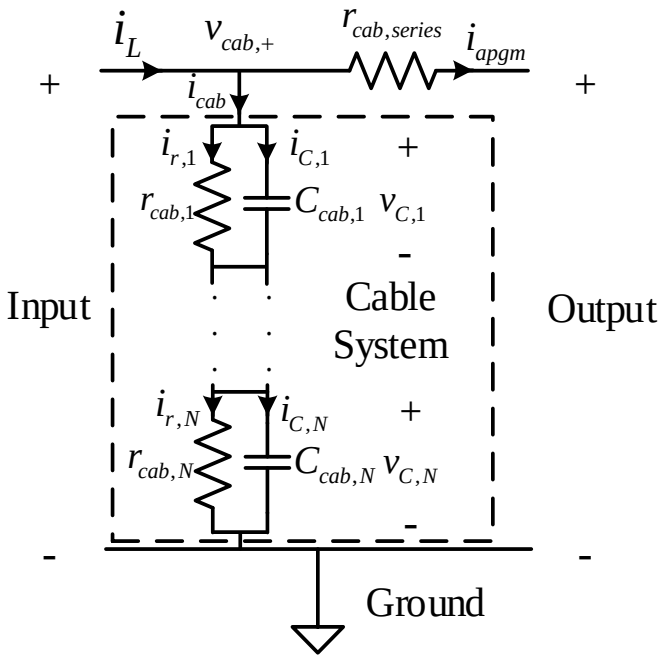

Fig.5.11 The detailed model for cable system

Table 5.7 APGM Components Specifications

Parameter	Value	Description
r_s	0.096Ω	Stator winding phase resistance
L_{ss}	0.55467mH	Stator winding inductance
λ_M	4.5947V·s	Magnetic flux linkage
P	8	Number of poles
C_{dc}	0.85333mF	DC capacitor capacitance
$r_{C,dc}$	4.3mΩ	DC capacitor series resistance
L_{dc}	0.064mH	DC inductor inductance
$r_{L,dc}$	0.064mΩ	DC inductor series resistance
r_L	12.4587Ω	DC load resistance
$r_{L,fault}$	0.2133Ω	Fault DC load resistance
r_{cab}	1.4897mΩ	Cable resistance
f_{smple}	5kHz	Switching frequency
v_{fsw}	26.67V	Switch Drop
f_{sr}	0.0107Ω	Switching Resistance
v_{fd}	26.67V	Forward Switch Drop

Table 5.8 APGM Control Specifications

Parameter	Value	Description
τ_{fv}	79.6μs	Bus voltage filter time constant
τ_{fi}	79.6μs	Inductor current filter time constant
τ_{srl}	100ms	Slew rate limiter time constant
$v_{mx,srl}$	200kV	Maximum output voltage SRL
$v_{mn,srl}$	2000kV	Minimum output voltage SRL
K_{pv}	0.6375A/V	Voltage control proportional gain
K_{iv}	180.75A/(V·s)	Voltage control integral gain
K_{ai}	1109.3A/A	Anti-windup gain
τ_r	1ms	Control relaxation time constant
$i_{pk,lim}$	3.75kA	Peak current limit
H	125A	Hysteresis level of modulator
w^*_{rm}	3600rpm	Dynamometer speed set point

5.4 Case Study

The system level simulation is performed in Simulink wherein the system is running in a steady state with a 30 MW load and subsequently a short-circuit fault is introduced at t = 0.4 s. At t = 0.9 s, the fault is removed and the system recovers. The predicted cable response is shown in Fig.5.12. The left column in Fig.5.12 is the transient performance of the temperature and the electric field in the positive and negative cable branches during the fault condition. The right column is the corresponding performance during the recovery. The respective capture time is from 391 ms to 451 ms and 891 ms to 951 ms. The figure represents the value that is determined every 2 ms. The arrows highlight the direction of the transient performance.

It is noted that the active bridge can no longer track the target voltage while a significant short-circuit current is presented in Fig.5.13. A large voltage and current spike can be observed when the fault is introduced. The voltage falls into the negative region for a very short time due to the large current draw. The power loss per meter in the cable sees a large surge during the fault transient and then stabilizes at a high level. The temperature encounters a spike at the initial fault time due to the large fault. Simultaneously, the electric field in the cable connected to the positive rail experiences a sudden drop to a negative field due to the voltage drop on the cable. During the fault, the temperature within the dielectric does not change significantly due to the large heat capacity and low thermal conductivity of the dielectric. It is noted that the electric field near the inner boundary experiences larger drop than the electric field near the outer boundary. The researchers suggest [1][3][11][15] that the electric field is modified by the combined effect of the applied voltage and the space charge accumulation. In Chapter 3, it also shows that the electric field will experience a sudden drop/shift in the magnitude during the initial voltage reversal under a high thermal gradient. This is due to the fact the voltage induced electric field shifts spontaneously accordingly. The electric field will evolve into the new steady state during the space

charge migration over time. However, in this specific case study, the system does not encounter a large voltage reversal nor a long transient time. Such an evolution may not be seen due to the short time duration and the short voltage reversal. Hence, the electric field in this study may only see a magnitude shift due to the applied voltage while temperature experience a relatively small increase during a line-line fault. One may notice that a large leakage current surge occurs during the fault due to the large voltage drop and the electric field shift. The cable insulation loss encounters a significant spike during the fault. However, it still remains only a small portion of the overall loss in the cable.

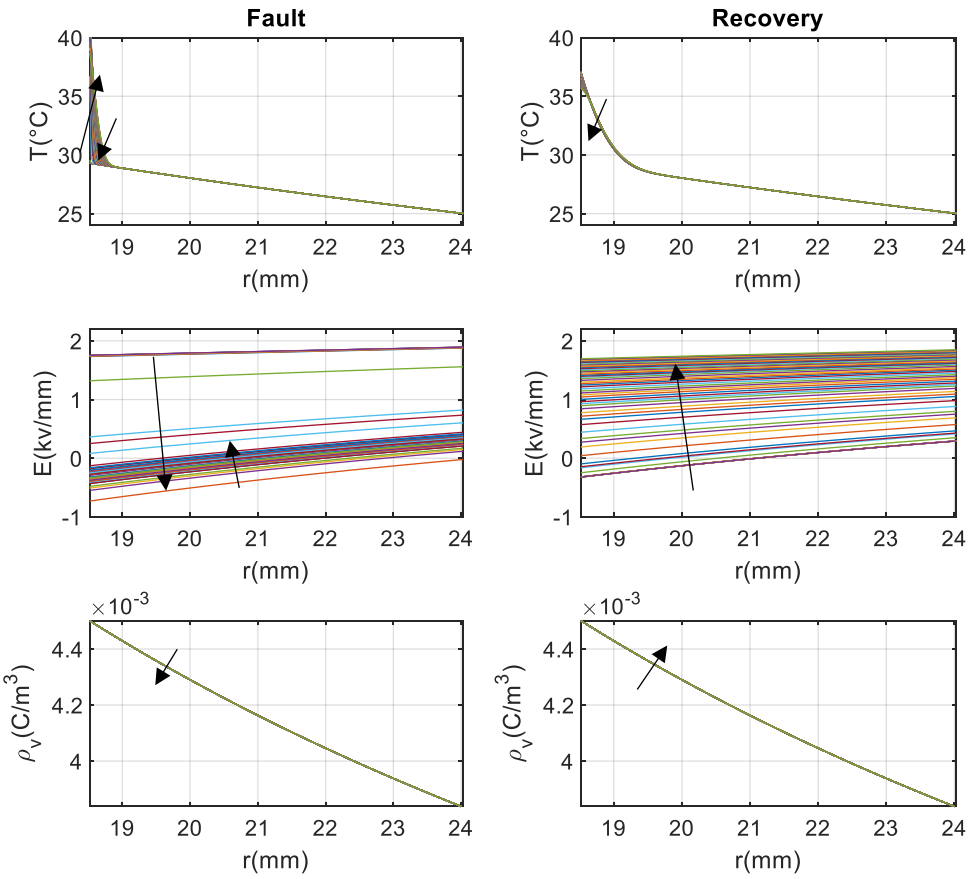

Fig.5.12 Fault and recovery performance of the cable on positive and negative terminals

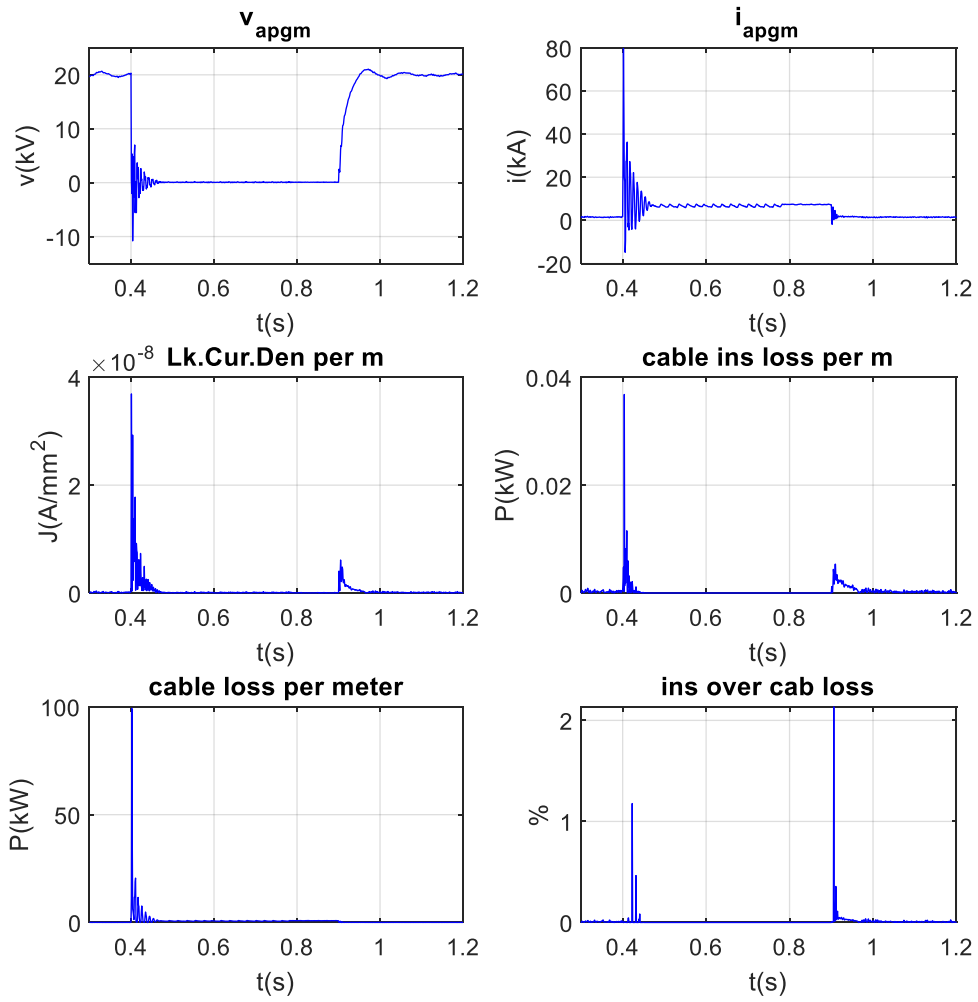

Fig.5.13 Load voltage and current performance

6. EXTENDING CIRCUIT MODELS TO INCLUDE DEFECT CHARGE

6.1 Introduction

Defect charge is a result of impurities in the dielectric material [19][42][44]. The defects may have the potential to create field distortions that lead to premature failure of the dielectric, electric discharge and dielectric breakdown for example. The defect charge may also lead to accelerated degradation of the dielectric due to local field enhancement. Indeed, the analysis on the effect of defect charge is challenging and is still under investigation. The simulation of the influence of the defect charge under an applied operating condition in commercial FEA tool, COMSOL and ANSYS Maxwell, is challenging. Herein, an attempt is made to explore methods to approximate the result of the defect charge within the equivalent electric circuit model.

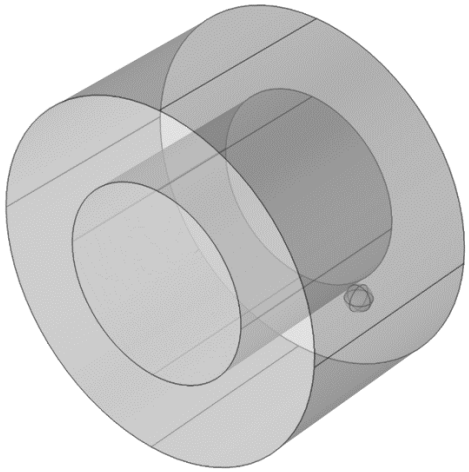

Fig.6.1 A representative defect charge in a coaxial cable in 3D

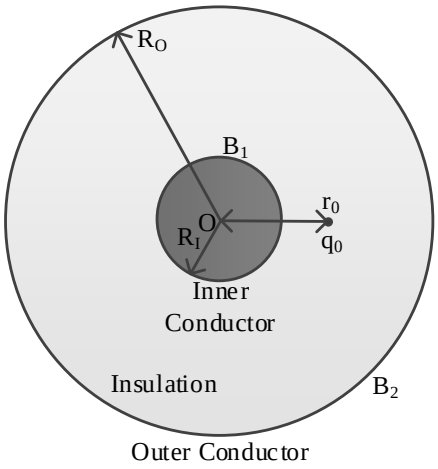

Fig.6.2 Defect charge in a coaxial cable in 2D

6.2 Point Charge Based Defect Charge using Method of Images

In practice, the defect charge is accumulated within a small concentrated region, a cavity for example as shown in Fig.6.1 and Fig.6.2. (The size of the defect charge location represented as a sphere is exaggerated with a diameter of 3 mm in Fig.6.1 for a better visualization.) To calculate the influence of the defect charge the cable whose dimensions are provided in Table 2.2 is used. For the study, it is assumed that the defect charge is a point charge. The electric flux distribution was computed using the commercial FEA tool COMSOL. Considering a 3D model, the electric potential and electric field/flux distribution in the dielectric consists of the radial, angular/circumferential, and z-axial components as shown in Fig.6.3 and Fig.6.4 (where blue contours are equal potential surfaces). A comparison result of the ratio of the radial component vs the z axial component of the electric field along the z axial path passing through the center of the defect charge starting from the edge of the defect charge is shown in Fig.6.5, where the peak at 4.2mm is due to the meshing in the COMSOL. Modeling this 3D behavior is a challenge. To address, it is first assumed that the primary focus of a cable design is establishing the maximum electric field within the dielectric. From Fig.6.4 and Fig.6.5 one can see that this occurs in the cross

section placed through the center of the defect charge. Thus, only this cross section is modeled. It is also assumed that the defect charge induced electric flux lines follow a Laplacian distribution and the flux lines are perpendicular to the surface between the inner conductors and the dielectric at the boundary B_1, the dielectric and the outer conducting shield at the boundary B_2. Unfortunately, there is not an exact solution from MoI that can solve the equipotential surfaces of a conducting cylinder and a point charge. To simplify the model, the MoI for a conducting sphere and a point charge is utilized in order to approximate the electric field generated by the defect point charge. To do so, both the inner conductor and the outer conducting shield are replaced with a conducting sphere as shown in Fig.6.6. The radius of the inner and the outer conducting sphere are the inner and the outer radius of the conducting cylinders respectively. As a result, due to symmetry the field distribution at the cross-sectional area of the defect charge location does not possess any z-axial components. Thus, only radial and circumferential components are needed for the model construction. The point charge induced electric field everywhere on the cross-sectional area still satisfies the boundary condition B_1 and B_2 on the cross-sectional area shown in Fig.6.2.

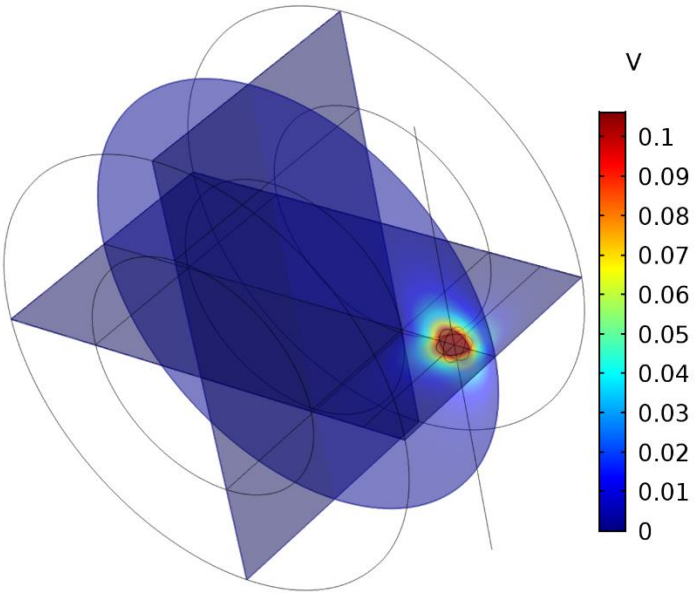

Fig.6.3 Charge induced potential from COMSOL

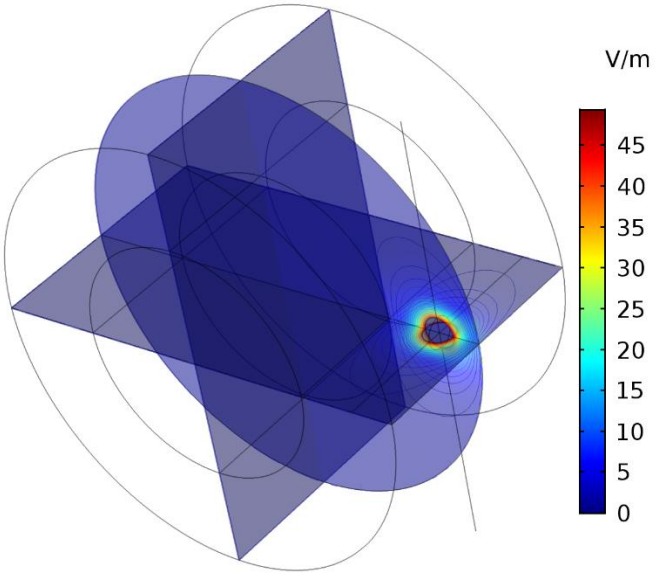

Fig.6.4 Charge induced electric field from COMSOL

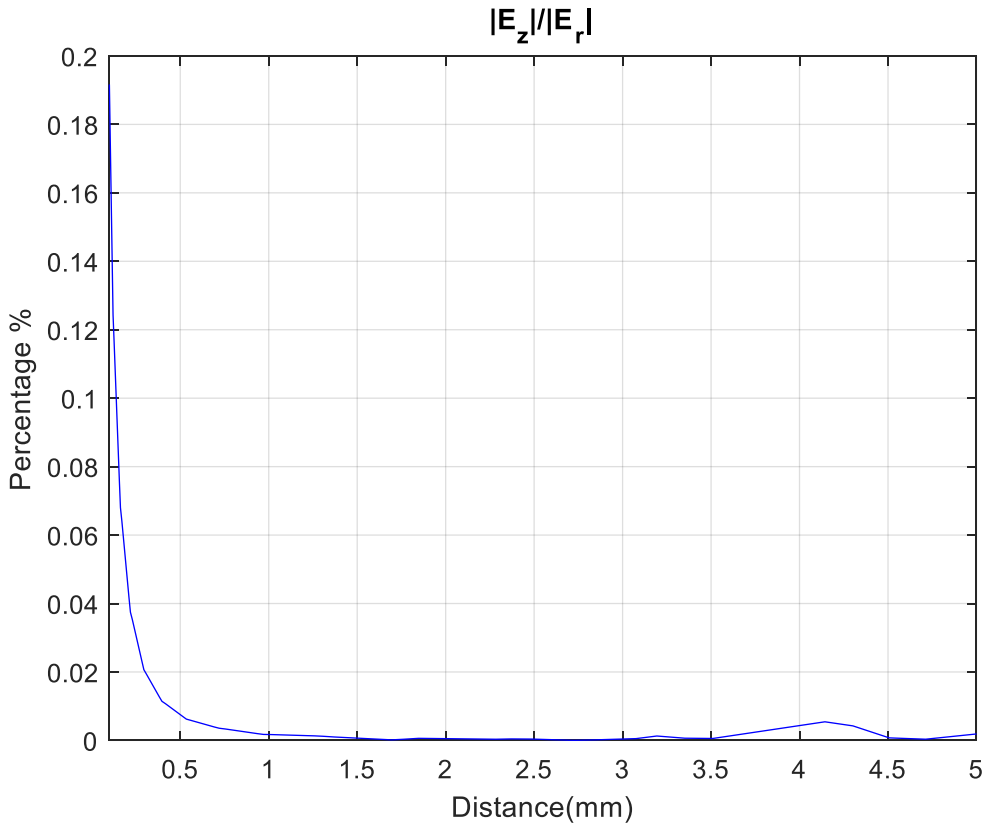

Fig.6.5 Charge induced electric field comparison along z axis through the centered of the defect

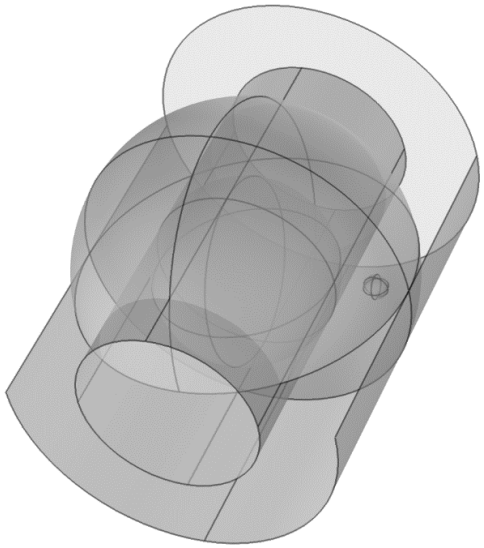

Fig.6.6 MoI assumption for 2 conducting spheres and 1 point charge

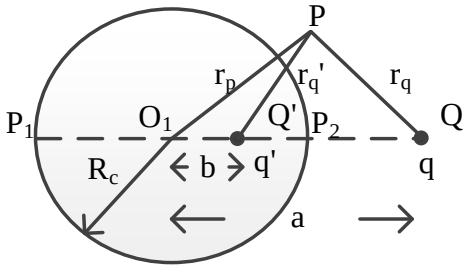

Fig.6.7 Method of images for a spherical equal potential surface

To begin, a similar derivation for MoI of an infinite cylinder has been readily shown in Chapter 4. To provide a background on the construction of a conducting spherical equal potential surface and a point charge, a representative spherical equipotential surface is shown in Fig.6.7[46][47][48][49][50]. Therein O_1 and R_c are the center and the radius of the sphere respectively. A point charge q and an arbitrary point P are located at r=a and r=r_p away from the center O_1 respectively. To solve for the fields outside the conducting sphere, the equipotential

surface is removed and replaced with an image point charge q' located at point b. To establish the location of b, the potential distribution due to a point charge q is first utilized. Specifically,

$$V(r)-V(r_0)=-\int_{r_0}^{r}\frac{q}{4\pi\varepsilon\gamma^2}d\gamma=\frac{q}{4\pi\varepsilon}\left(\frac{1}{r}-\frac{1}{r_0}\right) \tag{6.1}$$

where the r is an arbitrary location and the r_0 is a reference point. As a result, the potential distribution outside the equipotential surface at an arbitrary point P due to q and q' can then be expressed by adding the two contributions using (6.1) which yields,

$$V_P=\frac{q}{4\pi\varepsilon}\left(\frac{1}{r_q}-\frac{1}{r_0}\right)+\frac{q'}{4\pi\varepsilon}\left(\frac{1}{r_q'}-\frac{1}{r_0}\right) \tag{6.2}$$

The r_q and r_q' are the segment PQ and PQ' between the charge q and the point P and the image charge q' and the point P, respectively. If one sets the reference point r_0 to be at infinity, this yields,

$$V_P=\frac{1}{4\pi\varepsilon}\left(\frac{q}{r_q}+\frac{q'}{r_q'}\right) \tag{6.3}$$

If one takes points on the surface, say P_1 and P_2, which lie on the same extended axial lines of the point charge q and q', then due to the grounded conducting surface, the potential (6.3) on the surface is zero, yielding,

$$V_{P_1}=\frac{1}{4\pi\varepsilon}\left(\frac{q}{a+R_c}+\frac{q'}{b+R_c}\right)=0 \tag{6.4}$$

$$V_{P_2}=\frac{1}{4\pi\varepsilon}\left(\frac{q}{a-R_c}+\frac{q'}{R_c-b}\right)=0 \tag{6.5}$$

By rearranging and equating (6.4) and (6.5), one may find the image charge value q' and the location b expressed as,

$$q'=-\frac{R_c}{a}q \tag{6.6}$$

$$b = \frac{R_c^2}{a} \tag{6.7}$$

Combining (6.3), (6.6) and (6.7), the potential from the point charge and image charge can be calculated through the space outside the conducting sphere.

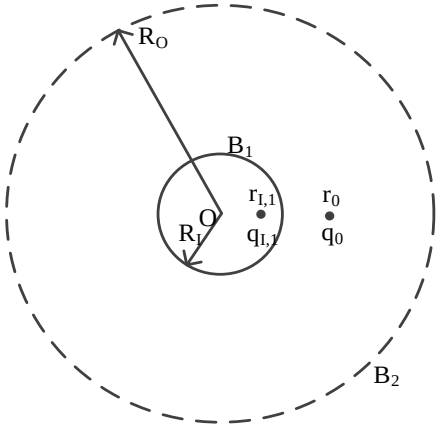

Fig.6.8 Placement of inner image charge $q_{I,1}$

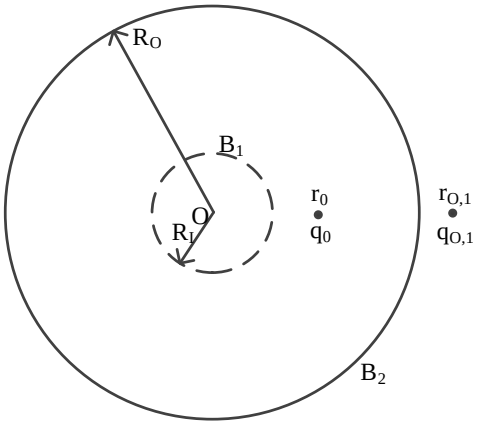

Fig.6.9 Placement of outer image charge $q_{O,1}$

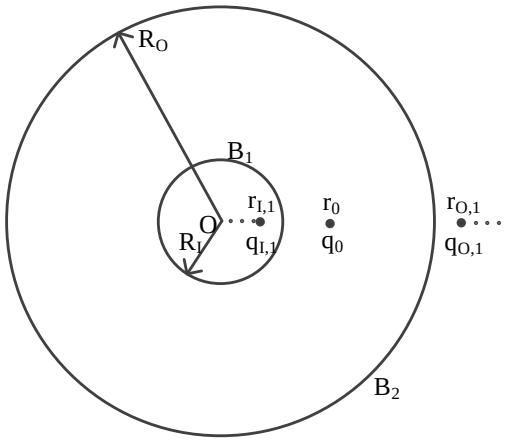

Fig.6.10 Placement of all charges

In the specific case of the defect charge in a coaxial cable as shown in Fig.6.2, multiple image charges are required to approximate the flux lines. To solve for the fields in the dielectric, the equipotential surfaces B_1 and B_2 are removed and replaced with an image charge $q_{I,1}$ and $q_{O,1}$ located at $r_{I,1}$ and $r_{O,1}$ respectively as shown in Fig.6.8 and Fig.6.9. Specifically, the point charge q_0 and the image charge $q_{I,1}$ yield an equipotential at the inner boundary B_1 as shown in Fig.6.8. Similarly, the point charge q_0 and the image charge $q_{O,1}$ yield an equipotential at the outer boundary B_2 as shown in Fig.6.9. The point charge values and their respective locations are:

$$q_{I,1} = -\frac{R_I}{r_q} q_0 \qquad r_{I,1} = \frac{R_I^2}{r_q} \tag{6.8}$$

$$q_{O,1} = -\frac{R_O}{r_q} q_0 \qquad r_{O,1} = \frac{R_O^2}{r_q} \tag{6.9}$$

However, the introduction of these two image charges distort the potential at the respective opposite boundaries. To compensate for this distortion, additional point charges $q_{I,2}$ and $q_{O,2}$ are placed at the location $r_{I,2}$ and $r_{O,2}$ respectively. This second pair of image charges $\{q_{I,2}, q_{O,2}\}$ are implemented based upon the first pair of image charges $\{q_{O,1}, q_{I,1}\}$ respectively. An approximate solution to satisfy both boundary conditions B_1 and B_2 is reached by implementing multiple image charges as shown in Fig.6.10. As a result, the image charges $q_{I,i}$ and $q_{O,i}$ are added to the geometry repetitively and their respective values and locations are:

$$\begin{aligned} q_{I,1} &= -\frac{R_I}{r_q} q_0 \qquad r_{I,1} = \frac{R_I^2}{r_q} \\ q_{I,i} &= -\frac{R_I}{r_{O,i-1}} q_{O,i-1} \quad r_{I,i} = \frac{R_I^2}{r_{O,i-1}}, i > 1 \end{aligned} \tag{6.10}$$

and

$$\begin{aligned} q_{O,1} &= -\frac{R_O}{r_q} q_0 \qquad r_{O,1} = \frac{R_O^2}{r_q} \\ q_{O,i} &= -\frac{R_O}{r_{I,i-1}} q_{I,i-1} \quad r_{O,i} = \frac{R_O^2}{r_{I,i-1}}, i > 1 \end{aligned} \tag{6.11}$$

where i is the ith pair of image charge. The number of charges is user-defined, where an increase in the number yields flux lines tending toward a Laplacian distribution and satisfying the boundary condition B_1 and B_2. In practice it has been found that on the order of 10 yields reasonable results.

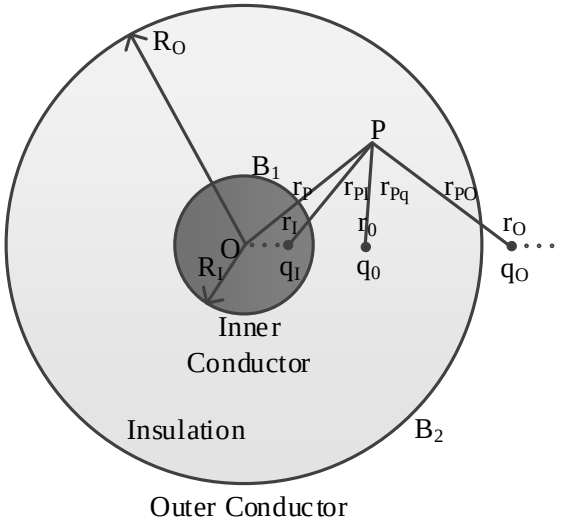

Fig.6.11 Method of image charges in a coaxial cable

The electric potential distribution generated by the defect point charge can be then derived using the similar method derived using (6.1) as shown in Fig.6.11. As a result, the electric potential at an arbitrary point P can be shown as,

$$V_P = \frac{q_0}{4\pi\varepsilon}\left(\frac{1}{r_{Pq}} - \frac{1}{r_0}\right) + \sum_{n=1}^{N}\frac{q_{I,n}}{4\pi\varepsilon}\left(\frac{1}{r_{PI,n}} - \frac{1}{r_0}\right) + \sum_{n=1}^{N}\frac{q_{O,n}}{4\pi\varepsilon}\left(\frac{1}{r_{PO,n}} - \frac{1}{r_0}\right)$$
$$V_P = \frac{1}{4\pi\varepsilon}\left(\frac{q_0}{r_{Pq}} + \sum_{n=1}^{N}\frac{q_{I,n}}{r_{PI,n}} + \sum_{n=1}^{N}\frac{q_{O,n}}{r_{PO,n}}\right) \quad (6.12)$$

where the r_P is an arbitrary location and the r_0 is a reference point which is at the infinity. The r_{Pq}, r_{PI}, and r_{PO} are the segments between the point P and the defect charge and the inner image charge set and the outer image charge set , respectively.

An example of the use of this method for the dielectric with a uniform conductivity was established for a conductor whose parameters are shown in Table 2.2. A defect charge of 1.6×10^{-13} C (10^6 e^-) is located at 34 mm away from the center. Initially, the reference voltage is set to zero at the outer conducting shield at boundary B_2. As a result, the voltage potential obtained using

(6.12) along the two conductor boundaries are shown in Fig.6.12. From the figure one can confirm that equipotential surfaces are obtained using the proposed approach. The comparison results of the potential and the radial electric field along the path of the defect charge location are shown Fig.6.13 and Fig.6.14. In practice, the charge induced electric potential and electric field goes to infinity when it approaches the location of the charge. To show a better comparison, the electric potential and the electric field is shown everywhere along the radius up to 0.1mm within the location of the defect charge. It is noted that the MoI is a relatively accurate method to predict the charge induced electric potential and the electric field distribution.

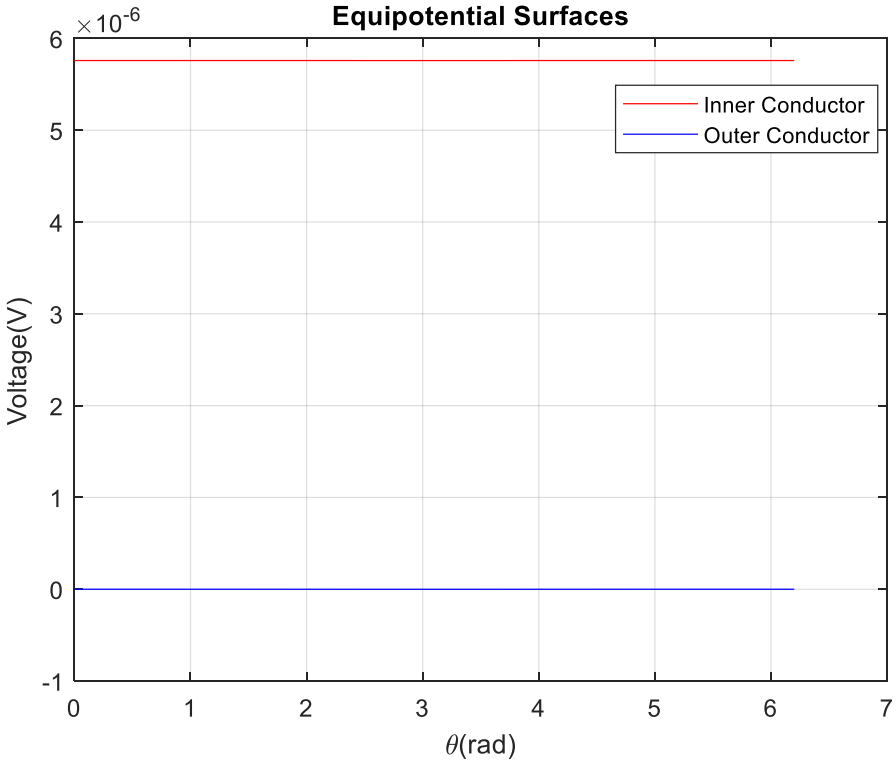

Fig.6.12 Boundary potential from Matlab

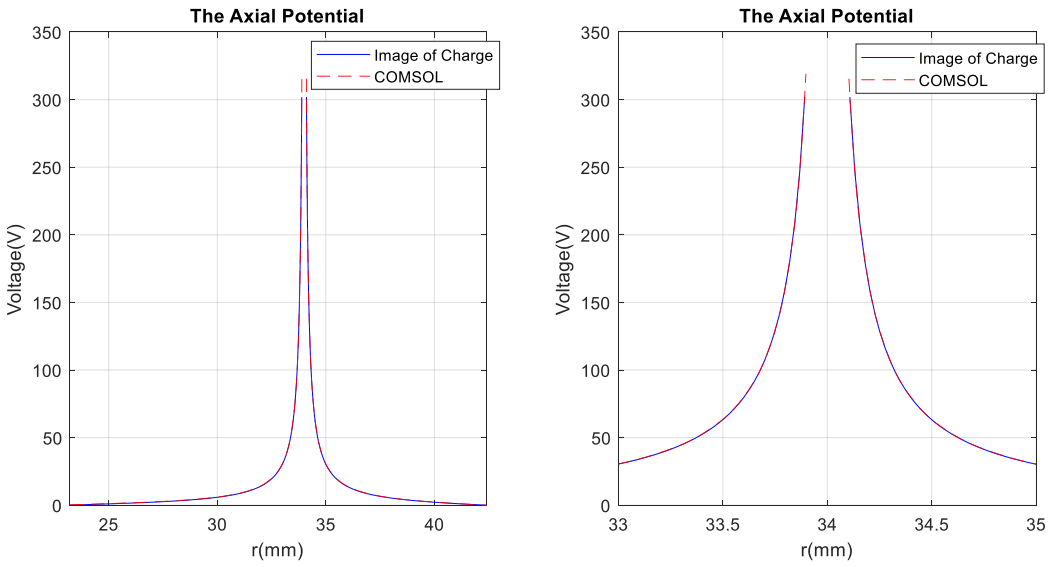

Fig.6.13 Simulation comparison of axial potential

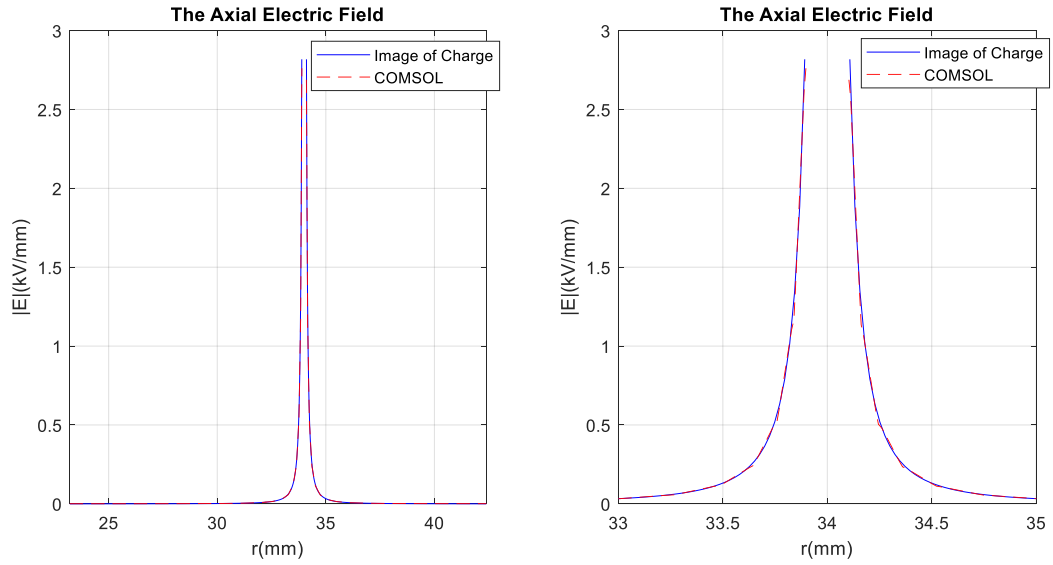

Fig.6.14 Simulation comparison of axial electric field

In the specific case of coaxial cable geometry, field distribution, and the field distribution illustration shown in Fig.6.2 and Fig.6.15, it is noted that the radial path along the defect charge experience the most impact and therefore is selected for field calculation. As a result, the electric equivalent circuit model is constructed along the specified radial path. In the specific case of a

radial flux tube as shown in Fig.6.16, the electric flux generated by the applied operating voltage and the defect charge denoted as E_{app} and E_{dfct}, respectively. The subscript 1 and 2 represent the electric flux at the start and the end surfaces of a flux tube, respectively. The total effective equivalent electric flux density E_{tot} is expressed,

$$E_{tot} = E_{app} + E_{dfct} \tag{6.13}$$

It is noted that E_{tot} is the actual electric field within the equivalent flux tube. It is also noted that the defect charge included field E_{dfct} only influences the electric field strength in the dielectric and does not travel within the dielectric. Within the equivalent electric circuit, the defect charge induced electric field is modeled using a voltage source V_{dfct} as shown in Fig.6.17. The V_{dfct} is the potential drop from the starting point to the end point of each flux tube segments using (6.12). As a result, the electric equivalent circuit model can be constructed as shown in Fig.6.18. The radial electric field can be calculated using the equivalent resistor/capacitor model as depicted in the previous sections.

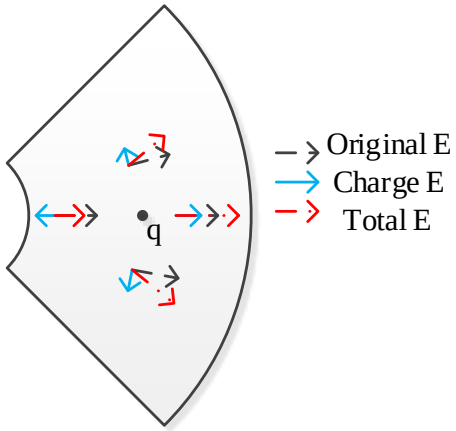

Fig.6.15 Field distribution of a defect charge

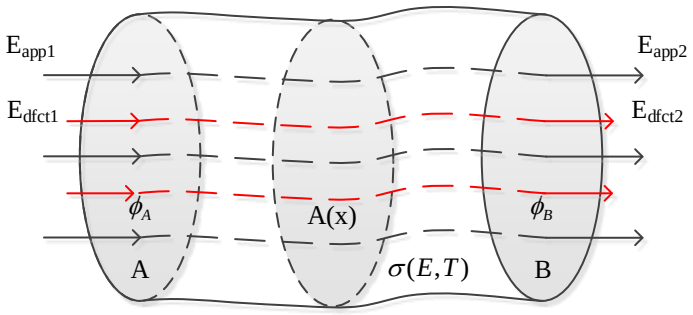

Fig.6.16 Equivalent flux tube with defect charge electric flux

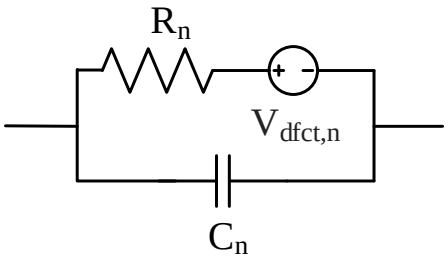

Fig.6.17 Equivalent circuit model with defect charge electric flux

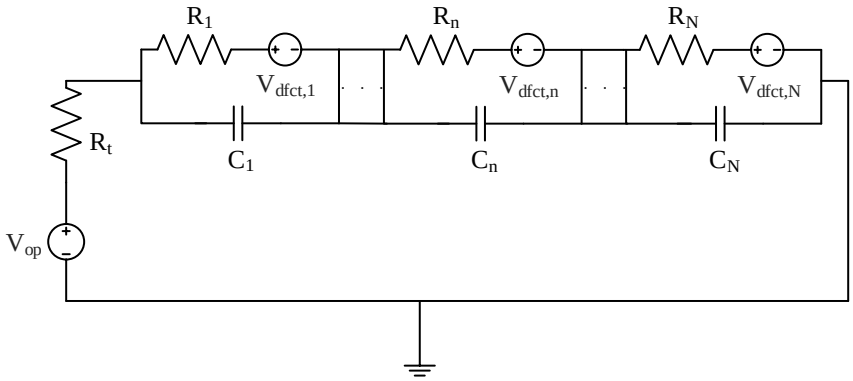

Fig.6.18 Equivalent circuit with defect charge

To explore the effect of the defect charge when energized, the cable is assumed to be operated at the applied voltage of 450kV (as shown in Table 2.2 and in the case study depicted in Chapter 2.3.3). At first, it is assumed there is no thermal gradient. This choice is made due to the fact that performing validation of the model that includes a thermal gradient with existing FEA software proved challenging. Specifically, within COMSOL one could not model a stationary defect charge within a nonlinear conductive material. The predicted electric field obtained with the circuit of Fig.6.18 is compared to that obtained using FEA in Fig.6.19. From the plots one can observe that the electric field predicted using the equivalent circuit matches that predicted from FEA quite well. One also notes that there is a large increase in the electric field in the vicinity of the defect, which is expected.

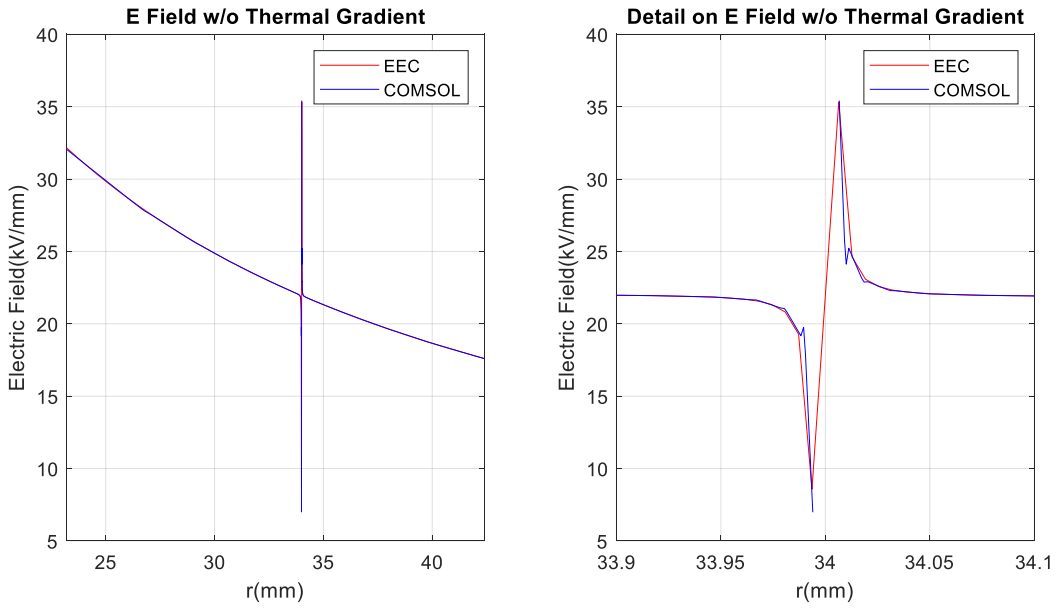

Fig.6.19 Electric field distribution without thermal gradient

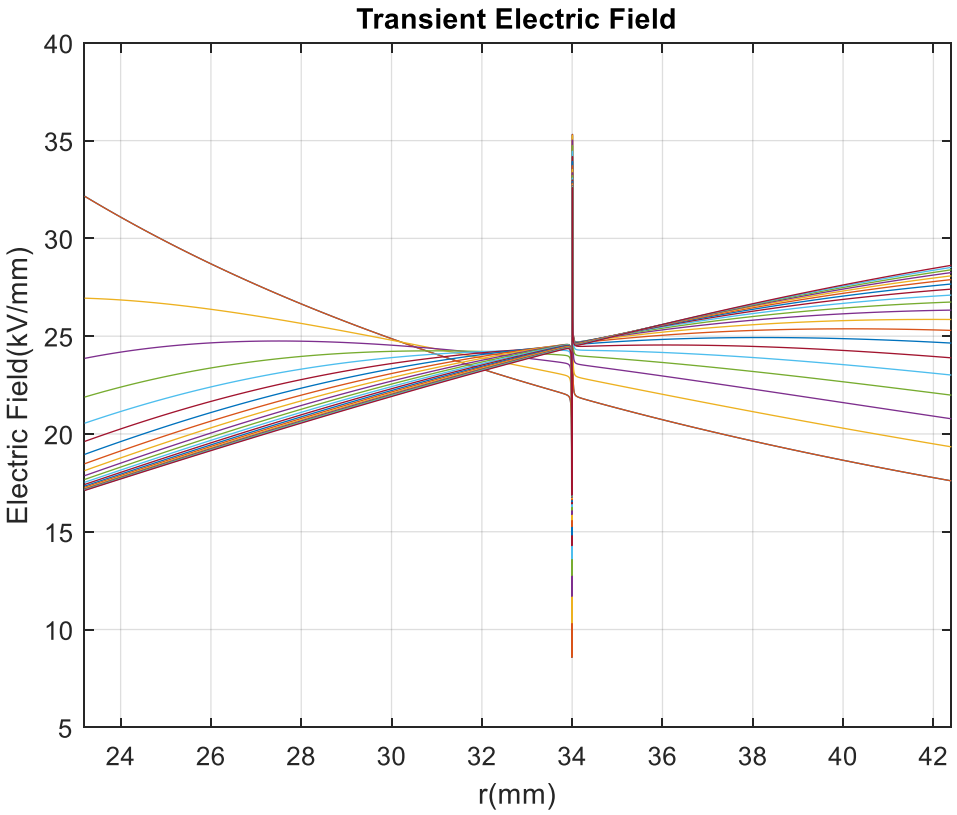

Fig.6.20 Transient capture of electric field

As a second study, a thermal gradient of 15^{o}C is simulated across the dielectric by incorporating the power loss within the thermal the thermal equivalent circuit. Within the simulation, it was assumed the cable operated at an ambient temperature of 35^{o}C. The transient behavior of the electric field is calculated using the equivalent circuit model over 100 minutes where the transient electric field is captured every 5 min. The results are shown in Fig.6.20 and Fig.6.21. From the figures it is noted that the initial electric field (with no temperature gradient) experiences the most impact from the defect charge due to the superposition of the applied electric field and the charge induced electric field. As the time increases, and space charge within the dielectric moves, the increase in the electric field from the defect charge is somewhat reduced

around the defect. This is attributed to the fact that the conductivity in the dielectric is a nonlinear function of the electric field, and thus it reshapes around the defect.

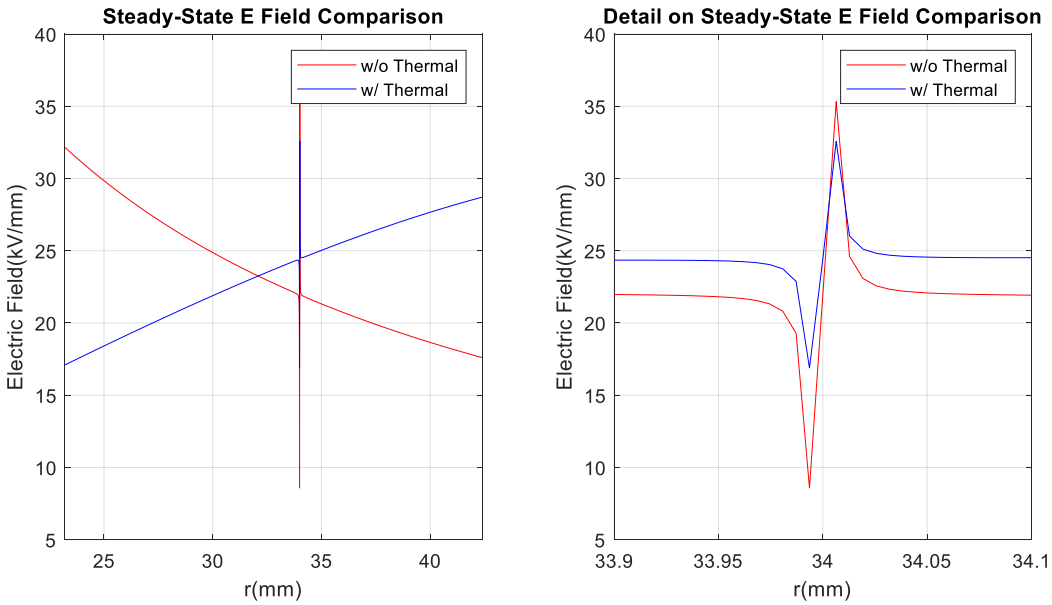

Fig.6.21 Electric field comparison with thermal gradient

7. SUMMARY AND FUTURE WORK

In this thesis, an approach to develop a coupled thermal/electric equivalent circuit model for the design of MVDC cables has been developed. The approach is general and provides the ability to predict the electric fields and space charge accumulation within single and multi-conductor DC cables. For the multi-conductor cables, a judicious use of the Method of Images has been shown be useful in constructing both electrical and thermal models. In contrast to traditional numerical methods, including finite element or finite difference, apriori knowledge of the electric field behavior is used to discretize the dielectric into a relatively (user defined) small number of electric flux tubes. The relatively coarse discretization enables the solution to be computed rapidly. The modeling approach has been validated using several examples presented in the literature. In addition, its usefulness has been highlighted in the optimization of a 20 kV 30 MW cable wherein objectives included minimization of mass, size and loss. Several designs from Pareto-Optimal Front has been compared wherein the impact of core material selection, dimension, and cable geometric alternatives has been highlighted. In addition, the equivalent circuit model is readily coupled within models of power converters to explore cable response during both steady state and transient operation. Finally, a method has been developed to model the impact of defect charge within the dielectric. This enables one to explore the potential impact of defects and potentially allow researchers to means to minimize their impact on cable life.

To date, single and two conductor cylindrical cables have been considered using the proposed approach. Additional geometric alternatives, including sandwich type cables, quad-core cables could be modeled and their performance compared with the cylindrical alternatives. The equivalent circuit model can also be extended to modeling capacitors and insulators, both of which are subject to the same nonlinearities under DC excitation. Finally, an approach to model the voids

within the dielectric and potentially predict partial discharge could likely developed based upon the modeling techniques proposed. This would enhance the cable design optimization by enabling exploration of candidate cable lifetimes.

REFERENCES

[1] M. Jeroense. (1997). Charges and Discharges in HVDC Cables in particular in mass mass-impregnated HVDC cables (Doctoral dissertation, TU Delft, Delft University of Technology.

[2] P. Morshuis and M. Jeroense, "Space charge in HVDC cable insulation," *IEEE 1997 Annual Report Conference on Electrical Insulation and Dielectric Phenomena*, Minneapolis, MN, 1997, pp. 28-31 vol.1.

[3] F.H. Kreuger, “Industrial High DC Voltage”, Delft University Press, Jan 1995, ISBN: 978-90-407-1110-7.

[4] R. Bartnikas, K.D. Srivastava, “Power and Communication Cables: Theory and Applications”, Wiley, Jan 2003, ISBN: 978-0-780-31196-1.(original book, with RC model)

[5] S. M. Alagab, S. Tennakoon and C. Gould, "Review of wind farm power collection schemes," *2015 50th International Universities Power Engineering Conference (UPEC)*, Stoke on Trent, 2015, pp. 1-5. doi: 10.1109/UPEC.2015.7339922

[6] D. J. Becker and B. J. Sonnenberg, "DC microgrids in buildings and data centers," *2011 IEEE 33rd International Telecommunications Energy Conference (INTELEC)*, Amsterdam, 2011, pp. 1-7. doi: 10.1109/INTLEC.2011.6099725

[7] S. D. Sudhoff *et al*., "A reduced scale naval DC microgrid to support electric ship research and development," *2015 IEEE Electric Ship Technologies Symposium (ESTS)*, Alexandria, VA, 2015, pp. 464-471.

[8] C. C. Reddy and T. S. Ramu, "On the computation of electric field and temperature distribution in HVDC cable insulation," in *IEEE Transactions on Dielectrics and Electrical Insulation*, vol. 13, no. 6, pp.1236-1244, December 2006.

[9] Bodega, R. (2006). Space charge accumulation in polymeric high voltage DC cable systems (Doctoral dissertation, TU Delft, Delft University of Technology), Chicago.

[10] Liu, R., Takada, T., & Takasu, N. (1993). Pulsed electro-acoustic method for measurement of space charge distribution in power cables under both DC and AC electric fields, *Journal of Physics D: Applied Physics*, *26*(6), 986.

[11] Jeroense, M.J.P.; Morshuis, P.H.F., "Electric fields in HVDC paper-insulated cables," *Dielectrics and Electrical Insulation, IEEE Transactions on* , vol.5, no.2, pp.225,236, Apr 1998.

[12] Zaccone E. “Advanced Technologies for Future Transmission Grids”, Springer London, 2013, ISBN: 978-1-4471-4548-6.

[13] D. Fabiani *et al*., "HVDC Cable Design and Space Charge Accumulation. Part 3: Effect of Temperature Gradient [Feature article]," in *IEEE Electrical Insulation Magazine*, vol. 24, no. 2, pp. 5-14, March-April 2008.

[14] Reddy, C.C.; Ramu, T.S., "On the DC Conductivity of HV DC Cable Insulation - Cautions in using the Empirical Models," *Electrical Insulation, 2008. ISEI 2008. Conference Record of the 2008 IEEE International Symposium on* , vol., no., pp.39,42, 9-12 June 2008.

[15] X. Chen, X. Wang, K. Wu, Z. R. Peng, Y. H. Cheng and D. M. Tu, "Effect of voltage reversal on space charge and transient field in LDPE films under temperature gradient," in *IEEE Transactions on Dielectrics and Electrical Insulation*, vol. 19, no. 1, pp. 140-149, February 2012.

[16] M. Fu, L. A. Dissado, G. Chen and J. C. Fothergill, "Space charge formation and its modified electric field under applied voltage reversal and temperature gradient in XLPE cable," in *IEEE Transactions on Dielectrics and Electrical Insulation*, vol. 15, no. 3, pp. 851-860, June 2008.

[17] L. Haydock, R. P. Allcock and R. N. Hampton, "Application of a finite element technique to model an electrical power cable," in *IEEE Transactions on Magnetics*, vol. 30, no. 5, pp. 3741-3744, Sept. 1994.

[18] El-Saadawi, Magdi & EL-Adawy, Mohamed & S. Abdel-Aziz, Mohamed. (2015). Numerical Simulation of Electric Field and Potential Distribution of Medium Voltage Cables using OctaveFEMM. .

[19] M. Alsharif et al., "FEM Modeling of Electric Field and Potential Distribution of MV XLPE Cables Containing Void Defect", in *2012 COMSOL Conference, Milan*, October 2012. Available: https://www.comsol.com/paper/fem-modeling-of-electric-field-and-potential-distributions-of-mv-xlpe-cables-con-13431.

[20] D. Fabiani *et al*., "Polymeric HVDC Cable Design and Space Charge Accumulation. Part 1: Insulation/Semicon Interface," in *IEEE Electrical Insulation Magazine*, vol. 23, no. 6, pp. 11-19, Nov.-Dec. 2007.

[21] S. Delpino *et al*., "Feature article - Polymeric HVDC cable design and space charge accumulation. Part 2: insulation interfaces," in *IEEE Electrical Insulation Magazine*, vol. 24, no. 1, pp. 14-24, Jan.-Feb. 2008.

[22] D. Fabiani *et al*., "HVDC Cable Design and Space Charge Accumulation. Part 3: Effect of Temperature Gradient," in *IEEE Electrical Insulation Magazine*, vol. 24, no. 2, pp. 5-14, March-April 2008.

[23] T. L. Hanley, R. P. Burford, R. J. Fleming and K. W. Barber, "A general review of polymeric insulation for use in HVDC cables," in *IEEE Electrical Insulation Magazine*, vol. 19, no. 1, pp. 13-24, Jan.-Feb. 2003.

[24] W. Choo, G. Chen and S. G. Swingler, "Space charge accumulation under effects of temperature gradient and applied voltage reversal on solid dielectric DC cable," *2009 IEEE 9th International Conference on the Properties and Applications of Dielectric Materials*, Harbin, 2009, pp. 946-949.

[25] K R Bambery, R J Fleming and J T Holbøll, "Space charge profiels in low density polyethylene samples containig a permittivity/ conductivity gradient", in *Jounal of Physics. D: Applied Physics*, vol. 34, no. 20, October 2001.

[26] Genetic Optimization System Engineering Tool (GOSET) For Use with MATLAB, Manual Version 2.6, School of Electrical and Computer Engineering, Purdue University, West Lafayette, IN, with United States Naval Academy, Annapolis, MD, 2014. Available: https://engineering.purdue.edu/ECE/Research/Areas/PEDS/go_system_engineering_toolbox.

[27] Boggs, S.A., "Semi-empirical high-field conduction model for polyethylene and implications thereof," *Dielectrics and Electrical Insulation, IEEE Transactions on* , vol.2, no.1, pp.97,106, Feb 1995.

[28] P. H. F. Morshuis, R. Bodega, D. Fabiani, G. C. Montanari, L. A. Dissado and J. J. Smit, "Calculation and Measurement of Space Charge in MV-size Extruded Cables Systems under Load Conditions," *2007 IEEE International Conference on Solid Dielectrics*, Winchester, UK, 2007, pp. 502-505.

[29] V. Ostovic, "Dynamics of saturated electric machines", University of Osijek, Jan 1989, ISBN 0-387-97079-7.

[30] Z. Y. Huang, J. A. Pilgrim, P. L. Lewin and S. G. Swingler, "Real-time electric field estimation for HVDC cable dielectrics," *2015 IEEE Electrical Insulation Conference (EIC)*, Seattle, WA, 2015, pp. 1-4.

[31] S.-M. Jung, Hyers-Ulam stability of linear differential equations of first order, In *Applied Mathematics Letters*, Volume 17, Issue 10, 2004, Pages 1135-1140, ISSN 0893-9659, Available: http://www.sciencedirect.com/science/article/pii/S0893965904816926

[32] C. Fuhrer, "Numerical Methods in Mechanics FMN081-2006: 8.12: Stability behavior of Euler's method" in *Lund Univerisity*, Feb 2006. Available: http://www.maths.lth.se/na/courses/FMN081/FMN081-06/lecture22.pdf.

[33] S. Bond, "ODE Stability", in CS 450, UIUC, Fall 2008. Available: https://courses.engr.illinois.edu/cs450/fa2009/odestability.pdf.

[34] S. D. Sudhoff(2014), *Power Magnetic Devices: A Multiobjective Design Approach*. IEEE Press/Wiley.

[35] N. Hampton, R. Hartlein, H. Lennartsson, H. Orton, R. Ramachandran "Long-life XLPE insulated power cables" JiCable, France, 2007 pp 593.

[36] K. Allwein, E., Marazhn, "Feasibility of HTS DC cables on board a ship",Sep.2011.Available:http://mydocs.epri.com/docs/publicmeetingmaterials/1110/7TNRSL46577/08%20-%20Economic%20Feasibility%20of%20HTS%20DC%20Cables%20on%20Board%20a%20Ship%20(Allweins%20for%20Klein).pdf.

[37] Liban Cables, 'Medium Voltage Cables Up to and Including 36kV'. Available:https://www.libancables.com/eservice/Lebanonen/fileLibrary/Download_540234110/Lebanon/files/Medium-Voltage-Cables.pdf.

[38] Brugg Cables, "High Voltage XLPE Cable Systems". Available:http://nepa-ru.com/brugg_files/02_hv_cable_xlpe/03_web_xlpe_guide_en.pdf

[39] Nelson Ljumba, "High Voltage Cable Insulation Systems", in *energize*, University of KZN, pp.30 May 20008

[40] A. Haddad.; D.D. Warne., "Advances in High Voltage Engineering", IET Power And Energy Series 40, 2004. Available: http://digital-library.theiet.org/content/books/po/pbpo040e.

[41] CME Wire and Cable, "Ampacity – Copper and Aluminum Type MV-90 and MV-105 Cables", Available:http://www.cmewire.com/catalog/sec15-mvs/mvs-01-amp.pdf

[42] L. A. Dissado, C. Laurent, G. C. Montanari and P. H. F. Morshuis, "Demonstrating a threshold for trapped space charge accumulation in solid dielectrics under DC field," in *IEEE Transactions on Dielectrics and Electrical Insulation*, vol. 12, no. 3, pp. 612-620, June 2005.

[43] J.C. Fothergill and R.N. Hampton, "Chapter 10 Polymer insulated power cable" in *Advances in High Voltage Engineering*, pp.478-510, 2004.

[44] Davies, D.K. , "Trapped Charges on Dielectrics," in *Nature* 203, 290-291, July 1964. Doi: 10.1038/203290a0

[45] S. Ramo, J. R. Whinnery, T. V. Duzer, "Fields and Waves in Communication Electronics", Wiley, 1994, ISBN: 978-0-471-58551-0.

[46] J.D. Jackson (1998), *Classical Electrodynamics (3rd ed)*, John Wiley & Sons.

[47] D.J. Griffiths(2012), *Introduction to Electrodynamics (4th ed)*, Pearson.

[48] K.A. Rousan(2019), *Approaching Method of Images and It's Relation with Real Images*, Sripatsingh College, India

[49] K.L. Wu, Th. Blu, *Basic Electromagnetics Chapter 3.5 Method of Images*. The Chinese University of Hong Kong http://ivp.ee.cuhk.edu.hk/~ele3310/data/Lesson11-13.pdf

[50] Today in Physics 217: the method of images. https://www.researchgate.net/publication/224759690_Specific_Heat_and_Thermal_Conductivity_Measurement_of_XLPE_Insulator_and_Semiconducting_Materials

[51] Today in Physics 217: the method of images. https://www.usplastic.com/knowledgebase/article.aspx?contentkey=508

[52] Today in Physics 217: the method of images. https://omnexus.specialchem.com/polymer-properties/properties/density

[53] X. Zhang and S. Pekarek, "A coupled thermal/electric circuit model for design of MVDC ship cables", *2017 IEEE Electric Ship Technologies Symposium* (ESTS), Arlington, VA, 2017, pp. 71-78.

VITA

Xiang Zhang received his B.S with highest distinction and PhD degrees in electrical and computer engineering from Purdue University in 2014 and 2019, respectively. His main interest includes MVDC cable modelling, electric machine design, and power electronics.